**Thesis for Doctor of Philosophy**

# Variant selection of Allotriomorphic Ferrite in Steels

Kim, Dae Woo (金 昊 優)

Computational Metallurgy

Graduate Institute of Ferrous Technology

Pohang University of Science and Technology

2011

**Variant selection of Allotriomorphic Ferrite in Steels** **2011 Kim, Dae Woo**

# 철계 다상 페라이트의 결정방위 선택

# Variant selection of Allotriomorphic Ferrite in Steels

# Variant selection of Allotriomorphic Ferrite in Steels

by

Kim, Dae Woo
Department of Ferrous Technology
(Computational Metallurgy)
Graduate Institute of Ferrous Technology
Pohang University of Science and Technology

A thesis submitted to the faculty of Pohang University of Science and Technology in partial fulfillments of the requirements for the degree of Doctor of Philosophy in the Graduate Institute of Ferrous Technology (Computational Metallurgy)

Pohang, Korea
December 3th, 2010

Approved by

Prof. Bhadeshia, H.K.D.H. — Major Advisor

Prof. Suh, Dong-Woo — Co-advisor

# Variant selection of Allotriomorphic Ferrite in Steels

Kim, Dae Woo

This dissertation is submitted for the degree of Doctor of Philosophy at the Graduate Institute of Ferrous Technology of Pohang University of Science and Technology. The research reported herein was approved by the committee of Thesis Appraisal

December 3th, 2010

Thesis Review Committee

Chairman: Prof. Bhadeshia, H.K.D.H
(Signature)
Member: Prof. Suh, Dong-Woo
(Signature)
Member: Prof. Lee, Hu-Chul
(Signature)
Member: Prof. Lee, Jae-Sang
(Signature)
Member: Dr. Um, Kyung-Keun
(Signature)

# Preface

This dissertation is submitted for the degree of Doctor of Philosophy at Pohang University of Science and Technology. The research described herein was carried out under the supervision of Professor H. K. D. H. Bhadeshia, Professor of Computational Metallurgy in the Graduate Institute of Ferrous Technology, Pohang University of Science and Technology and Professor of Physical Metallurgy, University of Cambridge, between March 2007 and February 2011.

This work is to the best of my knowledge original, except where suitable references are made to previous work. Neither this, nor any substantially similar dissertation has been or is being submitted for any degree, diploma or other qualification at any other university or institution. This dissertation does not exceed 60,000 words in length.

The research has been published as follows:

Kim, D.W., R.S. Qin, and H.K.D.H. Bhadeshia, *Transformation texture of allotriomorphic ferrite.* Jamshedpur India, 2008 Microstructure and Texture in Steels, 2008

Kim, D.W., R.S. Qin, and H.K.D.H. Bhadeshia, *Transformation texture of allotriomorphic ferrite in steel.* Materials Science and Technology, 2009. **25**(7): p. 892-895.

Kim, D.W., Suh, D.W and H.K.D.H. Bhadeshia, *Dual orientation and variant selection during diffusional transformation of austenite to allotriomorphic ferrite.* Journal of Materials Science, 2010. **45**(15): p. 4126-4132.

Kim, D.W., Suh, D.W and H.K.D.H. Bhadeshia*, Plastic strain and variant selection during diffusional transformation*. Houston USA, 2010 Materials Science and Technology Conference, 2010

Kim, D.W., Suh, D.W and H.K.D.H. Bhadeshia*, Plastic strain and variant selection during diffusional transformation in steels*. to be submitted.

Kim, D.W., Ryu, J.H, Suh, D.W and H.K.D.H. Bhadeshia*, Texture prediction by artificial neural netwrok approach*. to be submitted.

MFT Kim, Dae Woo
20081010 Variant selection of Allotriomorphic Ferrite in Steels,
Department of Ferrous Technology
(Computational Metallurgy) 2010
Advisor: Bhadeshia, H. K. D. H.; Prof. Suh, Dong-Woo
Text in English

## Abstract

The orientation of crystals of allotriomorphic ferrite in austenite has been investigated in order to understand the mechanism by which particular relationships are favoured over others via a process known as “variant selection”. This kind of selection in the context of diffusional transformations contrasts with displacive products where the interaction of transformation plasticity with an external field is the dominant selection criterion. With diffusional reactions the local environment of the growing crystal controls its crystallography. Variables such as the location of the nucleation site, the number and orientation of parent grains with which the site is in contact, interfacial velocity and impingement effects have been identified here to play a systematic role in variant selection.

It is conceivable that an allotriomorph may seek to adopt an orientation which matches well with all the adjacent austenite grains. Such simultaneous lattice matching has been investigated theoretically in order to predict the probability of such events as a function of polycrystalline aggregates of austenite grains which themselves may be textured. It is found that both using the theory, and through experimental determinations, that the probability of simultaneous matching depends not only on the intensity of texture in the austenite, but also the presence of

appropriate low-angle grain boundaries.

In addition, a new type of simultaneous matching has been discovered a special coincidence site lattice (CSL) boundaries. Quantitative analysis has been carried out to confirm that such matching is more probable when the ferrite forms at particular CSL boundaries.

To explain many macroscopic texture observations, it is necessary not only to consider the role of the nucleation site, but also the fact that subsequent growth can, through hard impingement with other growing grains, stifle some grains and hence diminish their contributions to the intensity of texture. A theory has been developed for such growth selection. A heterogeneous distribution of stored energy in austenite grains plays a significant role on the growth selection process. The model is validated on measured data.

With the help of an artificial neural network model, the development of transformation texture due to allotriomorphic ferrite has been predicted in "interstitial-free" steels. The method includes the influence of several parameters including chemical composition, cold rolling reduction and annealing temperature and has been compared with expectations from published data.

# Contents


PREFACE I

ABSTRACT III

CONTENTS V

NOMENCLATURE IX

CHAPTER 1: INTRODUCTION AND AIM 1

CHAPTER 2: REVIEW OF ALLOTRIOMORPHIC FERRITE 5

2.1 Introduction 5

2.2 Thermodynamics 6

2.3 Nucleation kinetics 10

2.4 Crystallography of allotriomorphs 16

2.5 Summary 18

CHAPTER 3: TRANSFORMATION TEXTURE IN STEELS 23

3.1 Introduction 23

3.2 Geometry of crystallography 26
3.2.1 Crystal structure and definition of a basis 26
3.2.2 Representation of rotation axis 28
3.2.3 Representation of macroscopic textures 32

3.3 Texture inheritance during transformation 34

3.4 Variant selection by different transformation mechanism 36
3.4.1 Definition of variant selection 36
3.4.2 Variant selection in displacive transformation 37
3.4.3 Variant selection during reconstructive mechanism 41

3.5 Comment on variant selection in diffusional transformation 44

**3.6 Summary** 45

**CHAPTER 4: DUAL ORIENTATION AND VARIANT SELECTION DURING DIFFUSIONAL TRANSFORMATION** 47

**4.1 Introduction** 47

**4.2 Calculation method for dual orientation possibility** 49
4.2.1 Methodology for drawing texture 49
4.2.2 Austenite grain structure 52
4.2.3 Introduction of ferrite texture 56

**4.3 Calculated ferrite textures** 58

**4.4 Grain edge and corner nucleation** 62

**4.5 Summary** 63

**CHAPTER 5: NEW TYPE OF DUAL ORIENTATION AT SPECIAL CSL BOUNDARIES** 64

**5.1 Introduction** 64

**5.2 Experimental procedures** 65
5.2.1 Heat treatment 65
5.2.2 EBSD measurement and accuracy of observations 66

**5.3 Numerical method** 67

**5.4 Classical type of dual orientation** 72

**5.5 Dual orientation at CSL boundaries** 78

**5.6 Calculation of dual orientation at some CSL boundaries** 78

**5.7 Conclusions** 80

**CHAPTER 6 SELECTIVE GRAIN GROWTH PHENOMENON AND VARIANT SELECTION** 86

**6.1 Introduction** 86

**6.2 Experimental procedures** 87
6.2.1 Heat treatment 87
6.2.2 EBSD measurement 88

6.2.3 Evaluation of stored energy in deformed austenite grains 88

**6.3 Orientation of allotriomorphic ferrite to adjacent austenite grains 92**
6.3.1 Undeformed sample 92
6.3.2 Deformed sample: nucleation at high energy boundaries 96
6.3.3 Deformed sample: nucleation at twin boundaries 105

**6.4 A Model for growth control 107**
6.4.1 Representation of interface velocity 107
6.4.2 A condition for growth controlling 117

**6.5 Analysis from the calculation results 118**

**6.6 Conclusions 120**

**CHAPTER 7 TEXTURE PREDICTION BY ARTIFICIAL NEURAL NETWORK APPROACH 128**

**7.1 Introduction 128**

**7.2 Details of modeling 129**

**7.3 Results and discussions 129**

**7.4 Summary 134**

**APPENDIX A TEXTURE DEVELOPMENT DURING REVERSE TRANSFORMATION 143**

**A.1 Introduction 143**

**A.2 Experimental procedures 144**

**A.3 Results and discussions 144**

**A.4 Conclusions 149**

**APPENDIX B FORTRAN PROGRAM 152**

**REFERENCES 156**

**ACKNOWLEDGEMENTS 174**

**CURRICULUM VITAE** **178**

# Nomenclature

| | |
|---|---|
| $\overline{x}$ | mole fraction of carbon in bulk austenite |
| $x^{\alpha\gamma}$ | mole fraction of carbon in ferrite in equilibrium with austenite |
| $x^{\gamma\alpha}$ | mole fraction of carbon in austenite in equilibrium with ferrite |
| $Ae_1$ | equilibrium $\gamma + \alpha$ / $\alpha + Fe_3C$ phase boundary |
| $Ae_3$ | equilibrium $\gamma$ / $\gamma + \alpha$ phase boundary |
| $\Omega_\alpha$ | equilibrium ferrite fraction by level rule |
| $\Omega_\gamma$ | equilibrium austenite fraction by level rule |
| $\mu_{Fe}^{\alpha}$ | chemical potentials of iron in ferrite |
| $\mu_{Fe}^{\gamma}$ | chemical potentials of iron in austenite |
| $\mu_{C}^{\alpha}$ | chemical potentials of carbon in ferrite |
| $\mu_{C}^{\gamma}$ | chemical potentials of carbon in austenite |
| $\Delta G^{\gamma\rightarrow\gamma'+\alpha}$ | free energy change for transformation from austenite to ferrite |
| $G^{\gamma}$ | free energy of austenite |
| $G^{\alpha}$ | free energy of ferrite |
| $G^{\gamma'}$ | free energy of enriched austenite |
| $a_{\mathrm{C}}^{\gamma}\{x\}$ | activity of carbon in austenite evaluated at the composition x |
| $a_{\mathrm{C}}^{\alpha}\{x\}$ | activity of carbon in ferrite evaluated at the composition x |
| $a_{\mathrm{Fe}}^{\gamma}\{x\}$ | activity of iron in austenite evaluated at the composition x |
| $a_{\mathrm{Fe}}^{\alpha}\{x\}$ | activity of iron in ferrite evaluated at the composition x |
| $\Delta G_m$ | maximum driving force for nucleation |
| $\Delta G_{total}$ | total free energy change between parent and product phases |
| $r^*$ | critical nucleus radius for stability during nucleation |
| $G^*$ | critical activation free energy barrier for nucleation |
| $r$ | radius of new nucleus during nucleation |
| $n_c$ | the number of critical size nuclei |
| $N$ | total number of atoms in the initial phase |
| $k_B$ | Boltzmann constant ($1.380\times10^{-23}$ J $K^{-1}$) |
| $T$ | Absolute temperature |
| $I_v$ | nucleation rate per unit volume |
| $\upsilon$ | collision frequency |
| $n_v$ | number of atoms per unit volume |
| $Z$ | Zeldovich non-equilibrium factor for nucleation |
| $Q$ | Activation energy for atoms crossing matrix/nucleus interface |
| $K_1^f, K_1^e, K_1^c$ | Site factor expressing fraction of active nucleation sites on grain boundary faces, edges and corners |
| $K_2^f, K_2^e, K_2^c$ | shape factor expressing fraction of active nucleation sites on grain boundary faces, edges and corners |
| $\varphi_1, \Phi, \varphi_2$ | three Euler angles |
| [A; **u**] | arbitrary **u** vector with respect to the basis A |

| | |
|---|---|
| (A J B) | rotation matrix transforming the components of vectors referred to the A basis to those referred to the B basis |
| (A J' B) | inverse matrix of (A J B) |
| ($\alpha$ J $\gamma$) | rotation matrix transforming the components of vectors in austenite to those in ferrite |
| $g$ | crystal orientation |
| $dV(g)$ | total volume of grain between g and $g+\Delta g$ |
| $V_0$ | total volume fraction of specimen |
| $\sigma$ | interfacial energy per unit area |
| $\sigma_{\gamma\alpha}$ | austenite matrix/ ferrite nucleus interfacial energy per unit area |
| $\alpha$ | allotriomorphic ferrite |
| $\gamma$ | austenite |
| $\Delta_{max}$ | maximum permitted deviation from exact rational low energy orientation relationship |
| $\sum$ | number of coincidence site lattice boundary |
| $\rho$ | average dislocation density in austenite grains |
| $\rho_0$ | dislocation density for fully recrystallized grains |
| $\sigma_{m\ ax}$ | maximum flow stress |
| $\overline{M}$ | mean Taylor factor |
| $M_j(g_j)$ | Taylor factor having grain orientation, $g_j$ |
| $\mu_T$ | temperature dependent shear modulus |
| $b$ | magnitude of Burgers vector |
| $\Delta G_{def}{}^{i}$ | intrinsic stored energy in an austenite grain, i |
| $\Delta G_{chem}$ | chemical driving force for phase transformation |
| $\overline{\Delta G_{def}}$ | average stored energy of austenite grains |
| $M$ | interface mobility |
| $M_0$ | pre-exponent in interface mobility |
| $Q_M$ | activation energy for migration of iron atom across the interface |
| $v_m^I$ | interface moving velocity of incoherent boundaries toward $\gamma_m$ |
| $v_m^S$ | interface moving velocity of semi-coherent boundaries toward $\gamma_m$ |
| $d_0$ | initial distance between two adjacent nuclei |
| $h$ | Plank constant ($6.626\times10^{-34}$ J s) |
| $\delta$ | atomic spacing |

# Chapter 1: Introduction and Aim

The crystallographic theory of martensite [1-3] is probably one of the most complete formulations in the field of materials science because of the clear and distinguishing characteristics of the shape deformation which on a macroscopic scale has the characteristics of invariant-plane strains. Since there is a pronounced interaction between these strains during transformation and externally imposed stresses or strains [4-8], the criteria for crystallographic variant selection have been well-established and the classic Patel and Cohen analysis [9], which gives the mechanical driving force due to this interaction, has been successful in explaining the selection of crystallographic variants in the context of martensitic or bainitic transformation in steels [4, 10, 11].

However, there is no equivalent model or established theory for reconstructive transformations such as allotriomorphic ferrite formation because at relatively high temperatures, long-range atomic diffusion can permit strain energy to be relaxed. So, macroscopic variant selection during diffusional transformation does not seem to be influenced by external stresses or strains [12]. However, some possibilities for local variant selection in diffusional transformation come from features associated with nucleation and grain growth phenomena.

It is favorable for ferrite to have a lattice correspondence with austenite with which it is in contact in order to reduce the activation energy for nucleation. Precipitations, therefore, have a low energy orientation relationship with at least one

of the adjacent austenite grains. These low energy orientation relationships are often assumed to be close to Kurdjumov-Sachs [13] or Nishiyama-Wassermann [14], whence densely packed planes and corresponding close-packed directions from the two lattices are approximately parallel. Since the specific variants of the orientation relationship may be selected randomly among all possibilities, there will be no favoured variants. However, circumstances may arise in which a few precipitations satisfy a low energy orientation relationship with both the austenite lattices which it is in contact. This is one type of local variant selection during diffusional transformation, dual orientation phenomenon.

The activation energy for the nucleation of ferrite could also be decreased by reducing the interfacial energy. According to the report by Lee and Aaronson [15, 16], interfacial energy decreases as the inclination angle between a facetted interface and the grain boundary plane of austenite decreases. Since a facetted interface of ferrite is corelated with a close-packed plane and direction of each phase, only variants satisfying the closest inclination angle would be favoured for nucleation. So, the grain boundary plane orientation is an important factor determining variant selection during diffusional transformation.

Variant selection by dual orientation and interfacial energy minimization are limited to the nucleation stage. However, hard impingement between particles during grain growth can also lead to variant selection. The impingement may occur due to relative differences in interface moving velocity due to the heterogeneous distribution of stored energy in each austenite grains and growth of certain ferrite

grain could be severely restricted by other ferrite grains. So, texture intensity of ferrite varies with grain size and major texture intensity would be determined by growth selection.

Variant selection during diffusional transformation could be determined by any of three criteria: dual orientation, grain boundary plane orientation and growth selection. For example, variant selection would be more influenced by grain boundary plane orientation than impingement if the stored energy difference between two adjacent austenite grains is quite small. Moreover, variant s hard to be observed when ferrite nucleates at low angle boundary because the dual orientation possibility itself is quite low [17, 18].

The emphasis therefore in this present research is on clarifying all possible situations which can affect variant selection during diffusional transformation to ferrite:

- Based on fundamental crystallographic theories, the dual orientation possibility has been calculated numerically for a variety of conditions
- A new type of simultaneous lattice matching has been discovered at specific coincidence site lattice (CSL) boundaries and has been compared with the classical dual orientation phenomenon
- A theory has been developed according to various stored energy conditions in austenite to explain growth selection.
- A series of Electron Back Scattered Diffraction (EBSD) experiments have been conducted to prove the calculation results or suggestions.

In addition, a neural network model was used to study the effect of metallurgical parameters such as chemical composition, rolling-reduction rate, annealing temperature etc. on texture development in “interstitial free” steels. The transformation texture development during reverse transformation in aluminum added TRIP steels is described briefly in the appendix.

# Chapter 2: Review of Allotriomorphic Ferrite

## 2.1 Introduction

Allotriomorphic ferrite is one of the most important phases in low-alloy steels. It is the first phase to form from austenite at temperatures below $Ae_3$ and thus it determines the composition and amount of austenite remaining for subsequent transformations. The term 'allotriomorph' implies that the shape of the particle does not respect its internal crystalline symmetry [19]; the ferrite nucleates at an austenite grain boundary and its morphology is determined by the contours of the boundary, which represents an easy diffusion path.

However, the morphology can sometimes be facetted with the interfaces corresponding to low energy phase between the parent and product phases. In such cases the shape is more likely to reflect the symmetry of the $\gamma$-$\alpha$ bicrystal [20]. It has been known that the ability of growing ferrite to form facets depends not just on the orientation dependence of interfacial energy but also on the driving force for transformation [21]. For example, particular variants which reduce the interfacial energy should be favoured among all possible low energy orientation relationships. Moreover, ferrite formed at high temperatures (low super-saturations) could appear facetted while that formed at lower temperature where the driving force is large may not (Figure 2.1).

Consequently, it is necessary to investigate the fundamental transformation theories of ferrite nucleation for a clear understanding of crystallographic

orientations and variant selection mechanisms in the context of allotriomorphic ferrite. This Chapter therefore addresses the basic thermodynamics and nucleation mechanisms for transformation.

## 2.2 Thermodynamics

The driving force for the transformation from austenite to ferrite is the reduction in the free energy of the total system obtained when lattice of austenite transforms a more stable mixture of austenite and ferrite. A schematic diagram illustrating this free energy change is shown in Figure 2.2, where austenite having bulk composition $\overline{x}$ can reduce the total free energy of system when ferrite forms with composition of $x^{\alpha\gamma}$ leaving the austenite composition of $x^{\gamma\alpha}$. The austenite is enriched by the carbon partitioning as ferrite grains grow. In equilibrium conditions, the composition of austenite follows the $Ae_3$ line until the eutectoid temperature is reached. $x^{\alpha\gamma}$ is the carbon mole fraction in the ferrite which is in equilibrium with austenite of composition $x^{\gamma\alpha}$.

These mole fractions of ferrite ($\Omega_\alpha$) and austenite ($\Omega_\gamma$) at certain temperature between $Ae_3$ and $Ae_1$ can be determined from the application of the lever rule in the phase diagram as follows:

$$\Omega_\alpha = \frac{x^{\gamma\alpha} - \overline{x}}{x^{\gamma\alpha} - x^{\alpha\gamma}} \tag{2.1}$$

$$\Omega_\gamma = \frac{\overline{x} - x^{\alpha\gamma}}{x^{\gamma\alpha} - x^{\alpha\gamma}} \tag{2.2}$$

Since equilibrium between two phases means that the chemical potentials ($\mu$) of the components in each phase are identical, the chemical potentials of Fe and C should be same in austenite and ferrite.

$$\mu_{Fe}^{\alpha} = \mu_{Fe}^{\gamma} \tag{2.3}$$

$$\mu_{C}^{\alpha} = \mu_{C}^{\gamma} \tag{2.4}$$

Meanwhile, the driving force, $\Delta G^{\gamma \rightarrow \gamma' + \alpha}$ can be determined by the difference between original free energy of austenite phase, $G^{\gamma}$ and free energy of product phases ferrite, $G^{\alpha}$ as well as carbon enriched austenite, $G^{\gamma'}$ Considering the mole fraction of each phase, this relationship could be represented by:

$$\Delta G^{\gamma \rightarrow \gamma' + \alpha} = \left(\Omega_{\gamma} G^{\gamma'} + \Omega_{\alpha} G^{\alpha}\right) - G^{\gamma} \tag{2.5}$$

The energy of each phase as:

$$G^{\gamma} = \overline{x}\mu_{C}^{\gamma}\{\overline{x}\} + (1 - \overline{x})\mu_{Fe}^{\gamma}\{\overline{x}\} \tag{2.6}$$

$$G^{\gamma'} = x^{\gamma\alpha}\mu_{C}^{\gamma}\{x^{\gamma\alpha}\} + (1 - x^{\gamma\alpha})\mu_{Fe}^{\gamma}\{x^{\gamma\alpha}\} \tag{2.7}$$

$$G^{\alpha} = x^{\alpha\gamma}\mu_{C}^{\alpha}\{x^{\alpha\gamma}\} + (1 - x^{\alpha\gamma})\mu_{Fe}^{\alpha}\{x^{\alpha\gamma}\} \tag{2.8}$$

where $\mu_{C}^{\gamma}\{\overline{x}\}$ represents the chemical potential of carbon in austenite when carbon concentration is equal to $\overline{x}$ and similarly for other chemical potentials. From Equations 2.6 to 2.8, Equation 2.5 can be expressed as:

$$\Delta G^{\gamma \rightarrow \gamma' + \alpha} = \overline{x}\left(\mu_{C}^{\gamma}\{x^{\gamma\alpha}\} - \mu_{C}^{\gamma}\{\overline{x}\}\right) - (1 - \overline{x})\left(\mu_{Fe}^{\gamma}\{x^{\gamma\alpha}\} - \mu_{Fe}^{\gamma}\{\overline{x}\}\right) \tag{2.9}$$

Writing the chemical potential term as μ = G + RTlna produces the results:

$$\Delta G^{\gamma \rightarrow \gamma' + \alpha} = \overline{x}RT\ln\frac{a_{\mathrm{C}}^{\gamma}\{x^{\gamma\alpha}\}}{a_{\mathrm{C}}^{\gamma}\{\overline{x}\}} - (1 - \overline{x})RT\ln\frac{a_{\mathrm{Fe}}^{\gamma}\{x^{\gamma\alpha}\}}{a_{\mathrm{Fe}}^{\gamma}\{\overline{x}\}} \tag{2.10}$$

(a)

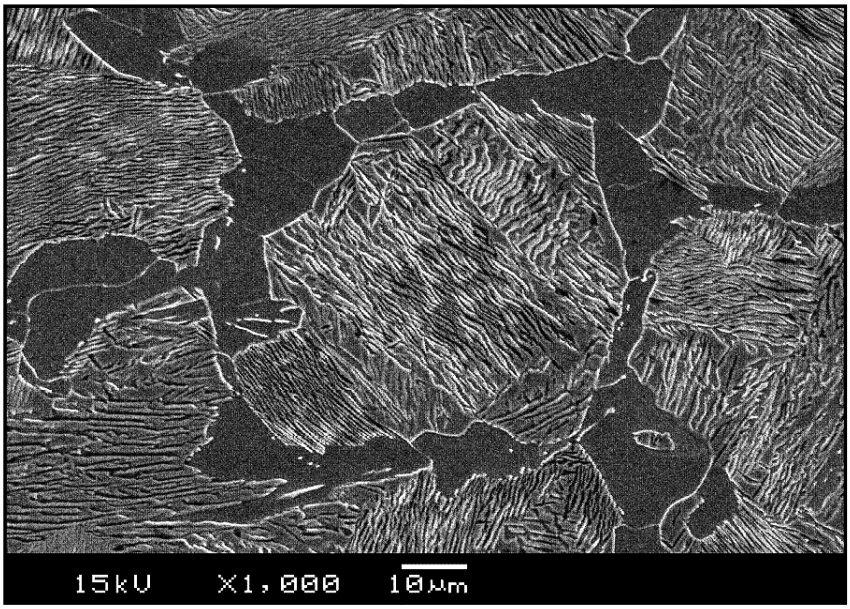


(b)

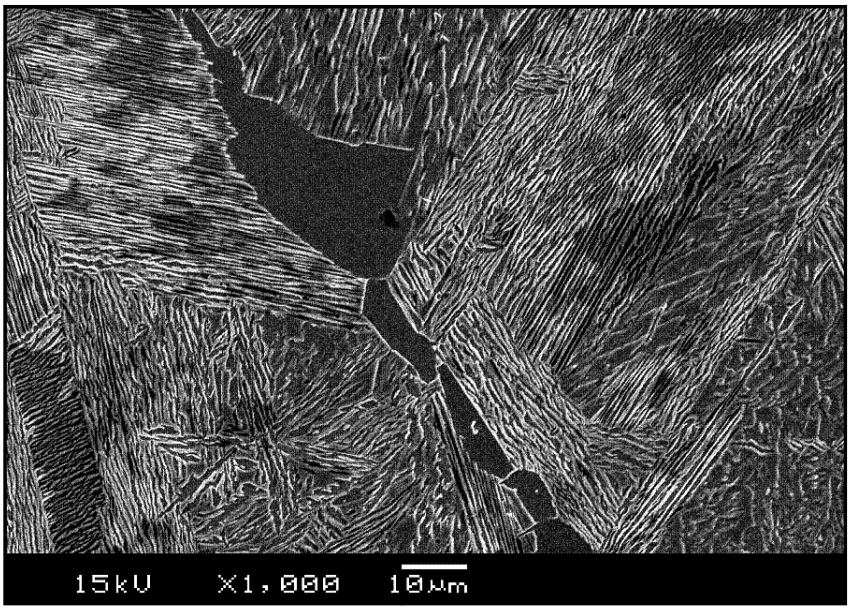


Fig. 2.1 SEM images of a low alloy steel, showing allotriomorphic ferrite (black) nucleated at prior austenite grain boundaries according to the different transformation temperature: (a) 700℃ and (b) 740℃. There is a greater tendency of faceting in the latter case.

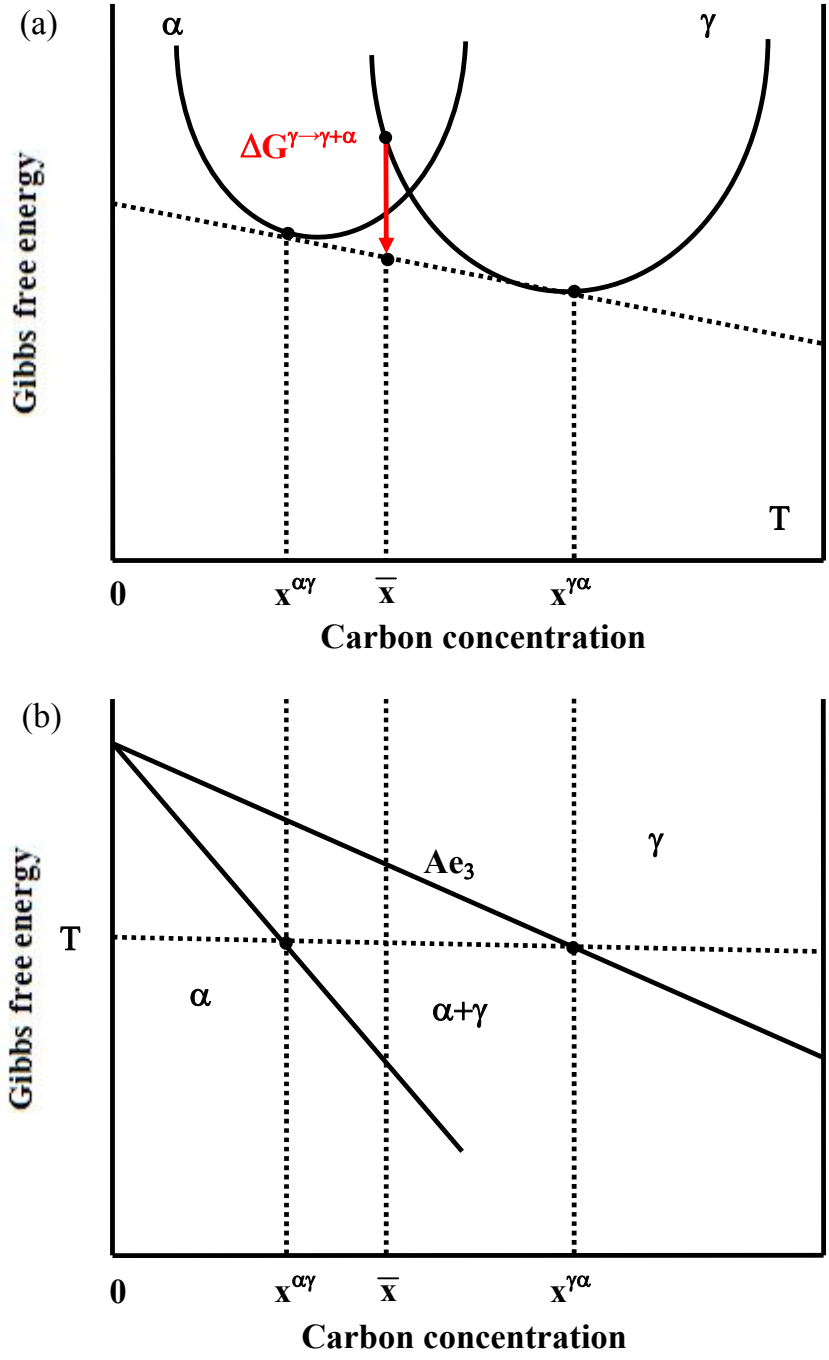


Fig. 2.2 Schematic free energy-composition diagram at temperature, T (a) and the corresponding section of the Fe-C phase diagram (b).

where $a_C^{\gamma}\{\overline{x}\}$ is the carbon activity in austenite evaluated at concentration $x^{\gamma\alpha}$ and similar definition apply to the other activity terms. To evaluate the free energy change for the austenite to ferrite transformation, the equilibrium phase boundary compositions and activities should be determined.

As it mentioned in Chapter 1, the crystallographic orientation of ferrite is determined mostly in early nucleation stage. The initial distance between neighboring nuclei is one of the important concepts in macroscopic growth selection governed by hard impingement effects. So, it is necessary to consider the driving force for ferrite nucleation which is different from the $\Delta G^{\gamma\rightarrow\gamma'+\alpha}$ described previously.

In a binary solution, the energy can be obtained using the double tangent construction illustrated in Figure 2.3 [22]. It is assumed that ferrite formation produces a very small change in the bulk composition of austenite when the nucleus volume is very small. As this small value tends to 0, the austenite composition tends towards the bulk composition, $\overline{x}$. $x_m$ is the nucleus composition and it is obtained when free energy change is maximized. So, $\Delta G_m$ is evaluated when the two tangents are parallel:

$$\Delta G_m = RT\hbar \frac{a_C^{\alpha}\{x_m\}}{a_C^{\gamma}\{\overline{x}\}} \tag{2.11}$$

## 2.3 Nucleation kinetics

According to the classical nucleation theories, for a pure system, the overall

driving force for the nucleation is expressed by the difference in the free energies between initial and final stages of the assembly. If the nucleus is constrained by the phase in which it nucleates then there will be an additional strain energy component in the overall free energy. The energy increase due to the formation of new interface also has to be considered in the total free energy change. During the homogeneous nucleation of a new ferrite phase in a solid austenite matrix, assuming a spherical nucleus of radius *r*, the total net free energy change is:

$$\Delta G_{total} = -\frac{4\pi}{3} r^3 (\Delta G_v - \Delta G_s) + 4\pi r^2 \sigma_{\gamma\alpha} \qquad (2.12)$$

where $\sigma_{\gamma\alpha}$ is the interfacial energy per unit area between ferrite and austenite, $\Delta G_v$ is $G_\gamma - G_\alpha$ and $\Delta G_s$ is the strain energy per unit volume. The critical free energy barrier for nucleation by thermal fluctuation is represented by $G^*$ and it is the value when free energy change $\Delta G_{total}$ is a maximum. This relationship can be expressed by:

$$\frac{d(\Delta G)}{dr} = -4\pi r^2 (\Delta G_v - \Delta G_s) + 8\pi r \sigma_{\gamma\alpha} = 0 \qquad (2.13)$$

The radius of nuclei satisfying Equation 2.12 is called critical radius $r^*$ and is:

$$r^* = \frac{2\sigma_{\gamma\alpha}}{(\Delta G_v - \Delta G_s)} \qquad (2.14)$$

Substituting it into Equation 2.13 again, we can obtain critical free energy barrier as:

$$G^* = \frac{16\pi {\sigma_{\gamma\alpha}}^3}{3(\Delta G_v - \Delta G_s)^2} \qquad (2.15)$$

Figure 2.4 shows this total free energy changes according to the radius of nucleus.

When the radius is smaller than the critical value, the total free energy can be

decreased by the dissolution of the nucleus but it can be reduction occurs beyond $r^*$. If we assume existence of stationary distribution of nuclei of size $r < r^*$, the number of critical size nuclei present, $n_c$ can be represented as a probability of such a nucleus being formed multiplied by the total number of atoms in the initial phase (vapor), $N$:

$$n_c = N\exp\left\{-\frac{G^*}{k_B T}\right\} \tag{2.16}$$

$n_c$ is a statistical distribution function for nuclei of critical size. Then, the nucleation rate is represented by combination of $n_c$ and the probability of a vapor atom condensing to a critical nucleus in unit time (a collision frequency). Thus, the nucleation rate per unit volume, $I_v$ is:

$$I_v = \upsilon n_v \exp\left\{-\frac{G^*}{k_B T}\right\} \tag{2.17}$$

where $\upsilon$ is defined as collision frequency and $n_v$ is number of atoms per unit volume. Considering the gradual decrease of distribution function in $r > r^*$, it has been modified by multiplication of the pre-exponential factor in Equation 2.15 with a parameter $Z$, known as the Zeldovich factor where:

$$Z = \frac{1}{r^*}\left\{\frac{G^*}{3\pi k_B T}\right\}^{0.5} \tag{2.18}$$

Since assumption of all these results based on the kinetics of gaseous collisions which is not applicable in real case, concepts of atomic vibration frequency ($k_B t/ h$) and activation energy for the transfer of atoms across the $\alpha/\gamma$ interface, $Q$ was considered. Consequently, nucleation rate per unit volume, $I_v$ is represented as:

$$I_v = \frac{k_B T}{h} n_v Z \exp\left\{-\frac{(Q + G^*)}{k_B T}\right\} \tag{2.19}$$

In heterogeneous nucleation, Equation 2.17 can be modified by [23, 24]:

$$I_v = \frac{k_B T}{h} n_v \rho_j \exp\left\{-\frac{\left(K_2^j G^* + Q\right)}{k_B T}\right\} \tag{2.20}$$

where $\rho_j$ is a density of sites factor, representing the number of sites of a particular type available for nucleation and is equal to $\{\delta/d_r\}^{3-j}$. $\delta$ is a effective grain boundary thickness and $d_r$ is the grain size of austenite. $K_2^j$ is a shape factor for the sites of different dimensionality j. j=3 for for homogeneous nucleation, 2 for faces, 1 for edges and 0 for corners. Equation 2.17 was modified again by Reed and Bhadeshia [25] by considering the shape and sites factor:

$$I_b^j = \frac{k_B T}{h} \frac{K_1^j}{\delta^2} \exp\left\{-\frac{\left(K_2^j G^* + Q\right)}{k_B T}\right\} \tag{2.21}$$

where $K_2^j$ is the shape factor and $1/\delta^2$ is total possible number of sites per unit area. Values of site factor, $K_1^j$ and shape factor, $K_2^j$ are listed in Table 2.1

Table 2.1 Values of site factor and shape factor according to the nucleation site [25]

| Site | Site factor | Shape factor |
|---|---|---|
| Face | $6.9\times10^{8}$ | $6.9\times10^{8}$ |
| Edge | $1.3\times10^{8}$ | $1.3\times10^{8}$ |
| Corner | $1.2\times10^{8}$ | $1.2\times10^{8}$ |

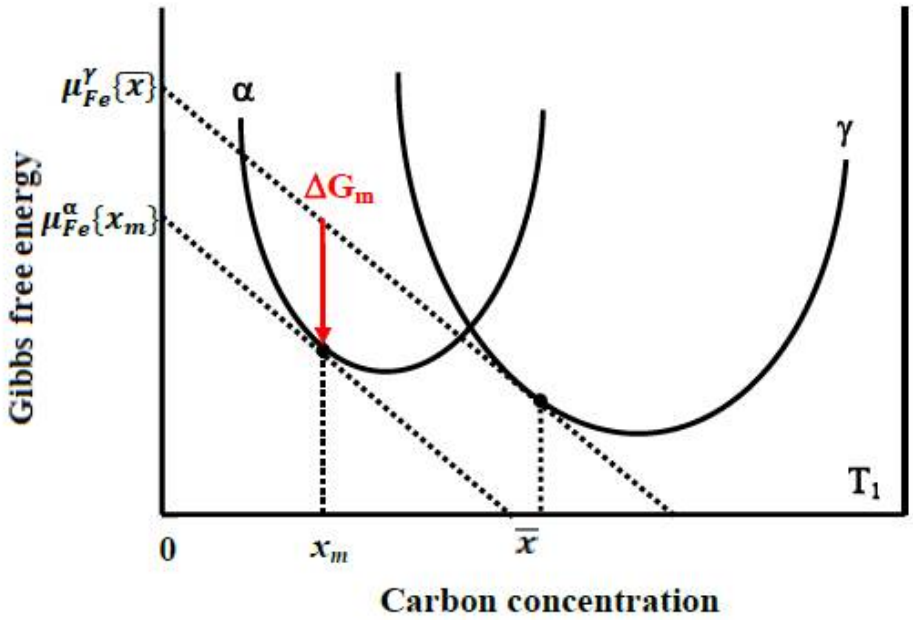


Fig. 2.3 Evaluation of driving force for nucleation, $\Delta G_m$ in free energy-composition diagram.

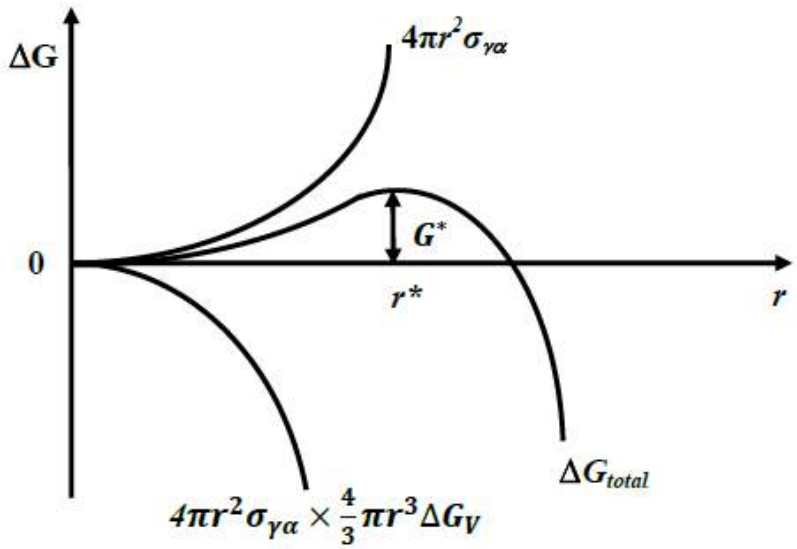


Fig. 2.4 The free energy change associated with the homogeneous nucleation of a spherical nucleus of radius *r*.

## 2.4 Crystallography of allotriomorphs

The properties of interfaces between austenite and ferrite depend on the relative dispositions of the crystals and the ferrite morphology is also severely influenced by the crystallography via the orientation dependence of the interfacial energy. Therefore, an understanding of the crystallography of each phase and orientation correlations between ferrite and austenite is an important feature of materials research.

Although many investigations including experiments and calculations have been carried out to study the crystallography of allotriomorphs during transformation [17, 18, 26-30], perhaps, the most important experimental observation is that orientation relationship between precipitations and matrix found during phase transformations is usually not random [26-29]. This frequency of occurrence of a particular orientation relationship usually exceeds the probability obtained by simply taking two separate crystals and joining them up in an arbitrary way. This indicates there are relationships between two phases [19].

In general, it has been known that this non-random orientation relationship exists to minimize the strain energy when nuclei form by the homogeneous deformation so that there is a coordinated movement of atoms. On the other hand, it can occur in order to reduce the interfacial energy and hence the activation energy for nucleation. Thermally activated embryos that comply with low-energy orientation would find it relatively easy to grow into successful nuclei, thus resulting in a non-random orientation distribution. The former case corresponds to the bainitic or martensitic

transformation by a displacive mechanism and the latter one corresponds to allotriomorphs by reconstructive transformation which is concerned in this thesis. Although the concept of displacements leading to crystal structure change is not appropriate for allotriomorphic ferrite, diffusional transformations also show similar low energy orientation relationship. Ryder and Pitsch [26, 27] proposed that $\alpha/\gamma$ orientation relationship lie nearby Bain orientation [31] and we can see that their experimental results in Figure 2.5 are in good accordance with their suggestion. King and Bell [28] conducted a detailed study of the crystallography of allotriomorphic ferrite in a Fe-0.47C wt % alloy isothermally transformed above the eutectoid temperature. In most cases they analyzed, ferrite was found to have Kurdjumov-Sachs (KS) [13] or Nishiyama-Wasserman (NW) [14] orientation relationship whose range was more restricted than the $11^{\circ}$ of the Bain orientation. The orientations tended to cluster at and around the KS and to a lesser extent the NW relations. It was always possible to find a close-packed plane of austenite which was within $2^{\circ}$ of a closet-packed plane of ferrite; within these planes, a close-packed direction of austenite could always be found within $8^{\circ}$ of a similar direction in the ferrite as shown in Figure 2.6.

Similar investigations also have been carried out by Babu and Bhadeshia with high silicon steels [30]. They produced complex microstructures consisting of bainitic ferrite, allotriomorphic ferrite and retained austenite, which permitted the direct observation of orientation relationship between ferrite and austenite in room temperature. Table 2.2 represents the experimental results and classical type of KS

or NW orientation relationships were observed. They also found a comparatively large number of random orientation relationship with both adjacent austenite grains (number 3, 6~14 in the table). In order to avoid a large activation barrier, the ferrite must nucleate with a good match with at least one of the austenite grains. Their results were therefore, quite different from traditional tendency of orientation relationship. However, it could be well explained by assumption of allotriomorphic ferrite growth into region far from their original nucleation sites and Purdy [32] also showed similar results in his TEM studies when ferrite growth occurred along grain boundary with high mobility.

## 2.5 Summary

Many crystallographic observations have shown that allotriomorphic ferrite has a particular non-random orientation relationship with at least one of adjacent austenite grains even though it is transformed from austenite by long range diffusion of atoms. Unlike the displacive mechanism, this tendency arise from endeavor of the embryo to reduce the interfacial energy per unit volume; are hence the finally activation energy during formation into nuclei.

This non-random crystallographic orientation is normally regarded as Bain, Kurdjumov-Sachs or Nishiyama-Wasserman orientation relationship and it is determined in the early stages of nucleation. It is therefore, important to understand the fundamental theories of thermodynamics as well as nucleation kinetics.

Although many investigations have been carried out and show that the

development of low energy orientation relationship during allotriomorphic ferrite transformation is almost similar to that in displacive transformation, reconstructive transformation seems to be further complicated in predicting orientation relationship precisely including variants selection since the ferrite grows by the uncoordinated movements of atoms and its growth is consequently not limited to the grain in which it originally nucleated.

(a)

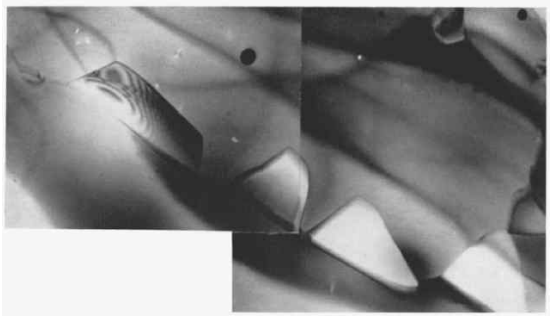

(b)

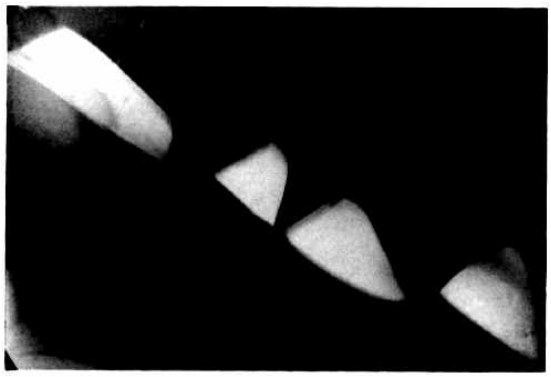

(b)

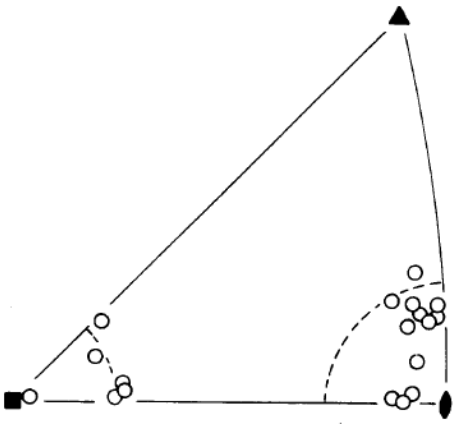

Fig. 2.5 (a) and (b) is bright field and dark field images respectively in TEM observation of grain boundary precipitation in Co+20 vol. % Fe. (c) is (100) poles of ferrite represented in circle with respect to the austenite grain. Dotted lines indicate the Bain orientation regions [26].

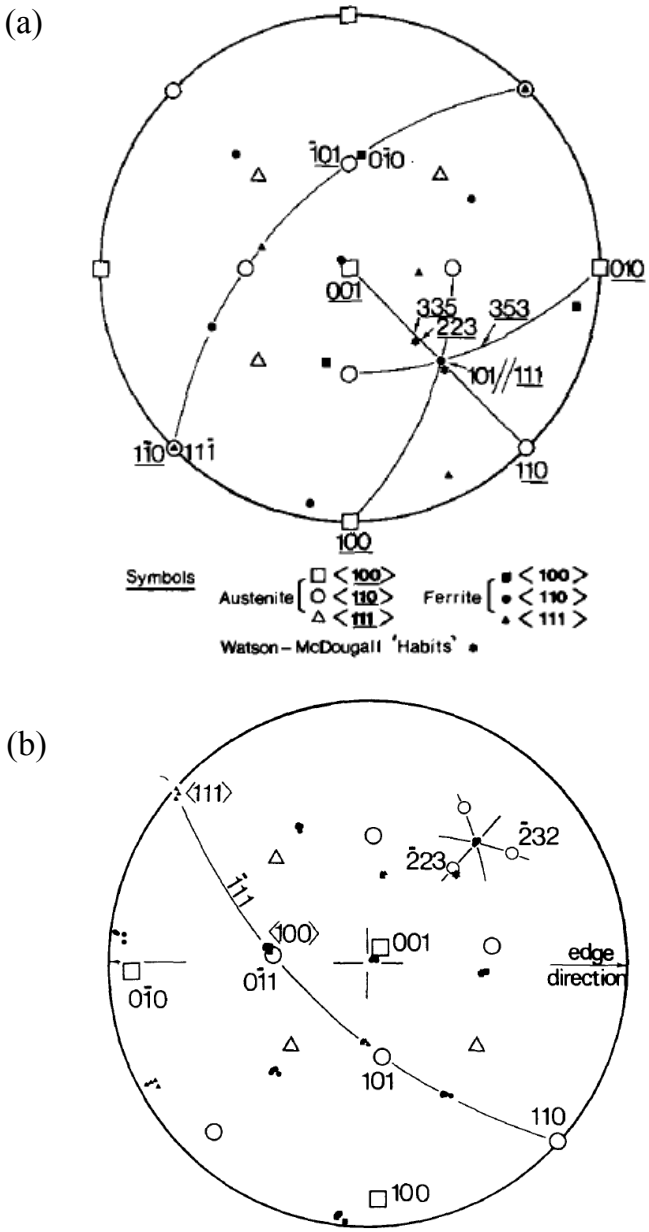


Fig. 2.6 (a) is a $(100)_{\gamma}$ standard projection illustrating a variant of the Kurdjumov-Sachs orientation relationship and (b) is orientation relationship observed from experiments [28].

Table 2.2 Ferrite-austenite orientation relationship: θ is the angle between {111} plane of austenite and {110} of ferrite. φ is the angle between <110> direction of austenite and <111> direction of ferrite [30]

| Number | θ | φ | Approximate orientation relationship |
|---|---|---|---|
| 1a | 4.04 | 3.2 | KS/ NW |
| 1b | 27.6 | 22.0 | - |
| 2a | 0.0 | 5.0 | NW |
| 2b | 18.1 | 32.1 | - |
| 3a | 15.1 | 4.9 | - |
| 3b | 13.7 | 13.6 | - |
| 4a | 0.0 | 5.3 | NW |
| 4b | 19.9 | 15.8 | - |
| 5a | 35.3 | 33.5 | - |
| 5b | 2.0 | 5.5 | KS/ NW |
| 6a | 20.5 | 16.4 | - |
| 6b | 15.0 | 1638 | - |
| 7a | 18.9 | 22.5 | - |
| 7b | 8.7 | 10.7 | - |
| 8a | 24.5 | 10.1 | - |
| 8b | 5.7 | 23.5 | - |
| 9a | 28.9 | 28.5 | - |
| 9b | 0.0 | 19.8 | - |
| 10a | 24.3 | 10.6 | - |
| 10b | 18.7 | 11.3 | - |
| 11a | 26.4 | 26.4 | - |
| 11b | 14.4 | 17.0 | - |
| 12a | 25.5 | 23.8 | - |
| 12b | 28.5 | 21.4 | - |
| 13a | 21.4 | 30.8 | - |
| 13b | 30.3 | 24.4 | - |
| 14a | 24.4 | 26.8 | - |
| 14b | 0.0 | 8.9 | - |
| 15a | 2.7 | 28.7 | - |
| 15b | 3.0 | 5.8 | KS/ NW |
| | 6.9 | 5.3 | KS/ NW |

# Chapter 3: Transformation texture in Steels

## 3.1 Introduction

The processes which generate textures and texture changes in steels consist mainly of deformation, recrystallization and transformation. Transformation texture plays a minor role in providing the initial orientation information for cold rolled and recrystallized steels when most processing is carried out in the ferrite phase after phase transformation. For example, interstitial free (IF) steels shows strengthening of intensity in the α-fiber texture component after severe deformation and γ-fiber texture become dominant over all texture components (Figure 3.1) [33]. Since the excellent formability of IF steels results especially from the formation of this strong γ-fiber texture, the effect of texture changes due to the phase transformation on the mechanical properties is insignificant.

However, steels can also be employed in the normalized or hot-rolled conditions, in which cases the texture changes accompanying transformation play a bigger role in influencing mechanical properties due to the particular texture developments. Some of these steels pass through a controlled rolling procedure, in which reductions are applied in the unrecrystallised austenite region or intercritical region before cooling to room temperature [34]. Figure 3.2 shows a schematic diagram of this controlled rolling process. Microstructure changes according to deformation in each stage were illustrated and it can be expected that the texture in the final product is largely influenced by texture changes due to the phase transformation in these processing

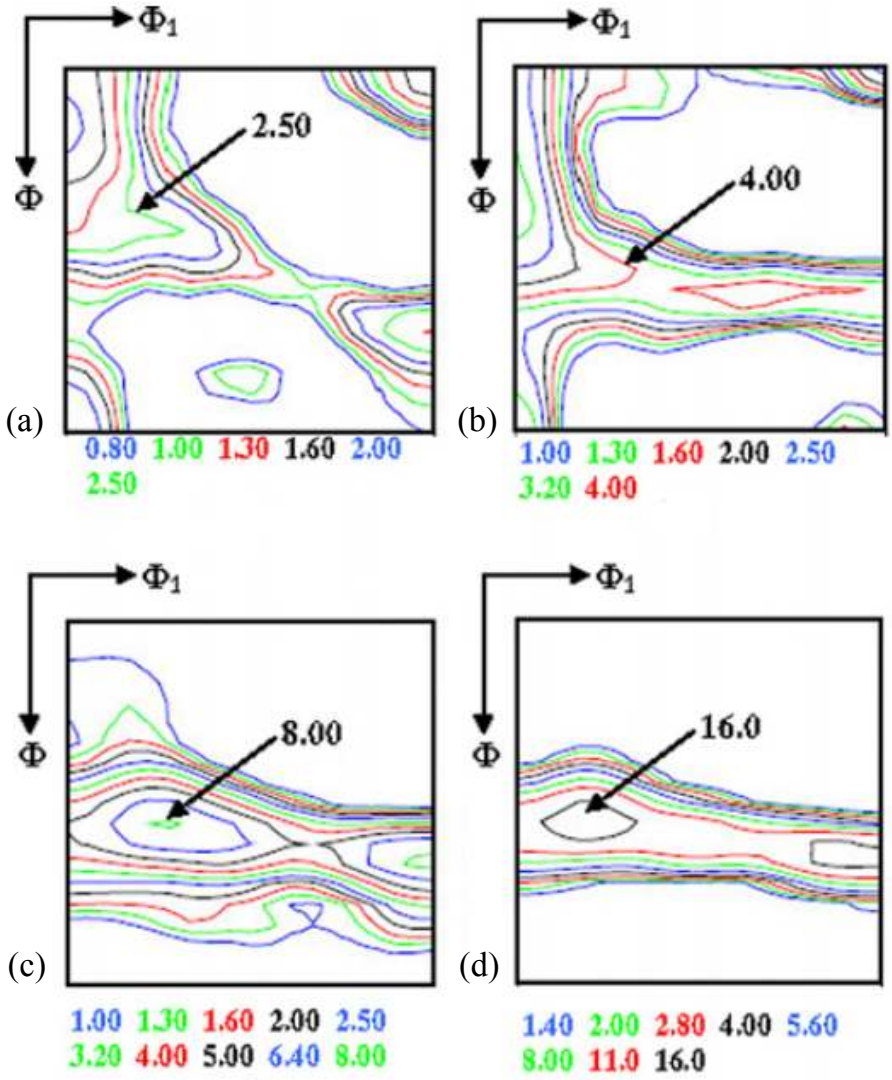


Fig. 3.1 $\Phi_2$=45° sections of ODF of the studied steels in [33]: (a) hot rolled, (b) 80% cold rolled, (c) 80% cold rolled and annealed at 700℃ and (d) 80% cold rolled and annealed at 800℃.

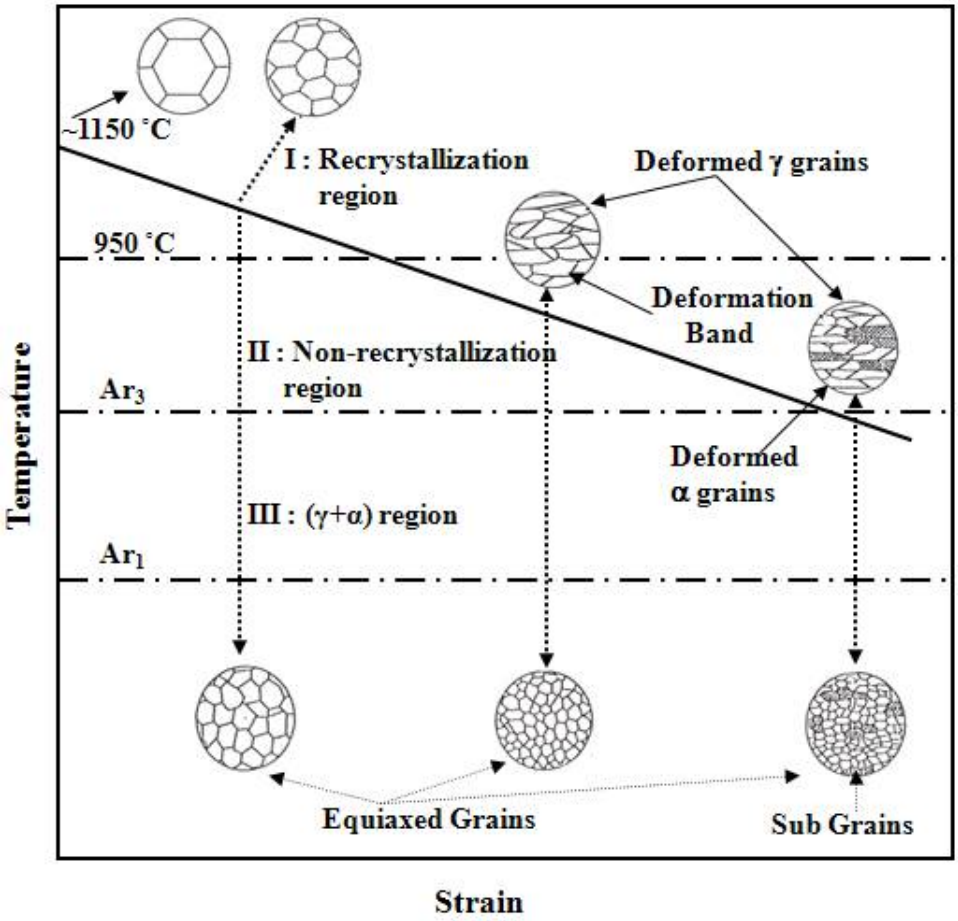


Fig. 3.2 Schematic diagram illustrating the three stages of the controlled rolling process and changes in microstructures with deformation in each stage [34].

conditions.

Since there are particular orientation relationships between precipitates and the matrix, development of transformation texture in ferrite is always correlated with the orientation of austenite. Thus it is important to understand the variables which affect the inheritance of texture from austenite to ferrite for clarifying the overall mechanism of texture development. In this section, various orientation relationships have been surveyed based on the fundamental concepts in the geometry of crystallography according to the variety of transformation conditions. The variant selection mechanism has been considered in depth for both the displacive and reconstructive mechanisms.

## 3.2 Geometry of crystallography

### 3.2.1 Crystal structure and definition of a basis

Throughout this thesis the vector and matrix notation due to MacKenzie and Bowles [2, 35] is used because is particularly good at avoiding confusion between frames of reference. Figure 3.1 shows a unit cell of austenite which has a face-centered cubic crystal structure. To specify the direction and magnitude of a vector for example **u** in the figure, it is necessary to have a reference set of coordinates. The frame of this crystal coordinate system can be represented by three orthogonal vectors $\mathbf{a}_1$, $\mathbf{a}_2$, $\mathbf{a}_3$ which lie along the three sides of the unit cell. These three vectors which are parallel to the unit cell edges and of magnitude equal to the austenite

lattice parameter form the crystallographic basis.

The set of vectors $\mathbf{a_i}$ (i =1, 2, 3) are called the basis vectors and the basis itself can be identified by a basis symbol A. Now, any vector **u** in the structure can then be written as:

$$\mathbf{u} = u_1\mathbf{a_1} + u_2\mathbf{a_2} + u_3\mathbf{a_3} \qquad (3.1)$$

where $u_1$, $u_2$ , $u_3$ are its components in the basis A.

In the special case when all these vectors are mutually perpendicular and of unit length the basis is called orthonormal. Any column vector **u** = [$u_1$ $u_2$ $u_3$] can be represented as [A; **u**]. For instance in Figure 3.3 u vector can be expressed with respect to the basis A by:

$$[\mathrm{A};\ \mathbf{u}] = [1\ 1\ 1] \qquad (3.2)$$

A single row matrix ($u_1$ $u_2$ $u_3$) with round brackets can also be used to represent the vector **u**, which is (**u**; A) = ($u_1$ $u_2$ $u_3$). Notice that the column matrix [A; **u**] is the transpose of row matrix (**u**; A). An arbitrary vector in one basis also can be represented in another by using a 3×3 transformation matrix, which is written as (B J A). It transforms the components of vectors referred to the A basis to those referred to the B basis. The matrices (A J B) and (A J´ B) represent the inverse and transpose of the (B J A) respectively. Since the directions of these basis vectors are different in every grain, it is necessary to show this information according to the unified criterion and the specimen coordinate system is usually used because it is determined by the external shape of the specimen. For rolled sheet steel, it is normal to choose a coordinate system S whose axes $\mathbf{s_1}$, $\mathbf{s_2}$ and $\mathbf{s_3}$ lie along the rolling

direction (RD), transverse direction (TD) and normal direction (ND) of the sheet, respectively, as shown in Figure 3.4. The preference of crystallographic orientation of each grain within the sample is the essence of texture. There are several ways to represent texture and they will be discussed later in this chapter.

### 3.2.2 Representation of rotation axis

For an orthonormal basis, a new unit vector which is parallel to an arbitrary vector, $\mathbf{u} = [u_1, u_2, u_3]$ can be obtained as:

$$\left[\frac{u_1}{\sqrt{u_1^2+u_2^2+u_3^2}}, \frac{u_2}{\sqrt{u_1^2+u_2^2+u_3^2}}, \frac{u_3}{\sqrt{u_1^2+u_2^2+u_3^2}}\right] = [\cos\alpha, \cos\beta, \cos\gamma] \quad (3.3)$$

where $\alpha, \beta, \gamma$ are angles between $\mathbf{u}$ and $\mathbf{a_1}$, $\mathbf{a_2}$, $\mathbf{a_3}$. Here the second basis B can be represented by specifying the direction cosigns of its three axes $\mathbf{b_1}$, $\mathbf{b_2}$, $\mathbf{b_3}$ in basis A, that is:

$$\begin{aligned}\mathbf{b_1} &= \cos\alpha_1 \times \mathbf{a_1} + \cos\beta_1 \times \mathbf{a_2} + \cos\gamma_1 \times \mathbf{a_3}\\ \mathbf{b_1} &= \cos\alpha_2 \times \mathbf{a_1} + \cos\beta_2 \times \mathbf{a_2} + \cos\gamma_2 \times \mathbf{a_3}\\ \mathbf{b_1} &= \cos\alpha_3 \times \mathbf{a_1} + \cos\beta_3 \times \mathbf{a_2} + \cos\gamma_3 \times \mathbf{a_3}\end{aligned} \quad (3.4)$$

where $\alpha_i$, $\beta_i$, $\gamma_i$ ($i$=1~3) are defined as angles between $\mathbf{a_i}$ and $\mathbf{b_1}$, $\mathbf{a_i}$ and $\mathbf{b_2}$, $\mathbf{a_i}$ and $\mathbf{b_3}$ respectively.

This relationship indicates the transformation from basis A to basis B which can be expressed by 3×3 matrix (A J B) as mentioned in 3.2.1:

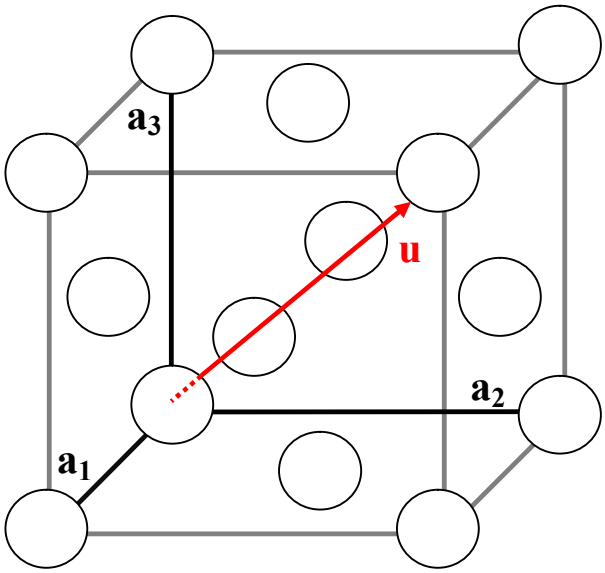


Fig. 3.3 An unit cell of face-centered cubic (FCC) and crystal coordinate system

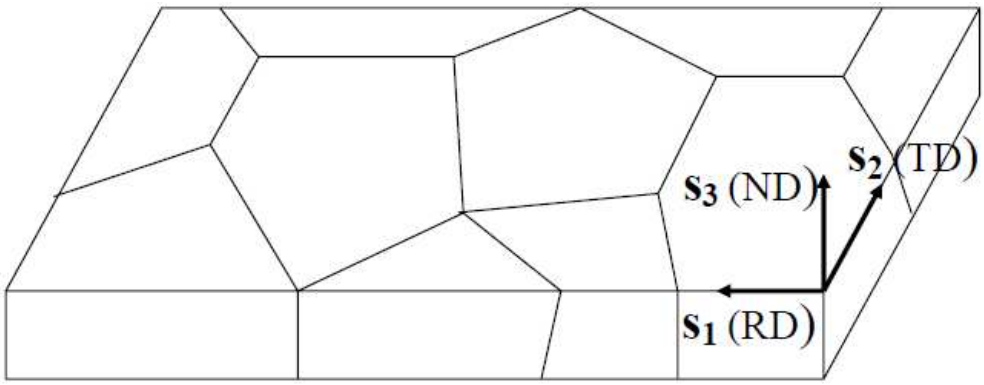


Fig. 3.4 Schematic diagram for sample reference frame. RD: rolling direction, TD: transverse direction, ND: normal direction.

$$(\mathrm{A\ J\ B}) = \begin{pmatrix} \cos\alpha_1 & \cos\alpha_2 & \cos\alpha_3 \\ \cos\beta_1 & \cos\beta_2 & \cos\beta_3 \\ \cos\gamma_1 & \cos\gamma_2 & \cos\gamma_3 \end{pmatrix} \tag{3.5}$$

Thus an arbitrary vector **u** in base B can be expressed according to the base A:

$$[\mathrm{A};\mathbf{u}] = (\mathrm{A\ J\ B})[\mathrm{B};\mathbf{u}] \tag{3.6}$$

$$[\mathrm{B};\mathbf{u}] = (\mathrm{B\ J\ A})[\mathrm{A};\mathbf{u}] \tag{3.7}$$

where (B J A) is a transverse matrix of (A J B). This rotation matrix can be expressed by an axis-angle pairs which has been well derived by Bunge [36] as:

$$\begin{pmatrix} \mathrm{u_1u_1(1-m)+m} & \mathrm{u_1u_2(1-m)+u_3m} & \mathrm{u_1u_3(1-m)+u_2n} \\ \mathrm{u_1u_2(1-m)+u_3n} & \mathrm{u_2u_3(1-m)+m} & \mathrm{u_2u_3(1-m)+u_1n} \\ \mathrm{u_1u_3(1-m)+u_2n} & \mathrm{u_2u_3(1-m)+u_1n} & \mathrm{u_3u_3(1-m)+m} \end{pmatrix} \tag{3.8}$$

where m=cos$\theta$, n=sin$\theta$ and $\theta$ is the corresponding right-handed rotation angle and it can be obtained from the fact that:

$$\mathrm{J_{11} + J_{22} + J_{33}} = 1 + 2\cos\theta \tag{3.9}$$

and the components of the vector u along the axis of rotation are given by:

$$\mathrm{u_1} = (\mathrm{J_{23} - J_{32}})/\ 2\sin\theta$$

$$\mathrm{u_2} = (\mathrm{J_{31} - J_{13}})/\ 2\sin\theta$$

$$\mathrm{u_3} = (\mathrm{J_{12} - J_{21}})/\ 2\sin\theta \tag{3.10}$$

The rotation matrix also can be represented by using Euler angles as shown in Figure 3.5 First, $\varphi_1$about the normal direction ND ($x_3$ in the figure), transforming the transverse direction TD ($x_2$ in the figure) into TD' and the rolling direction RD ($x_1$ in the figure) into RD' as shown in (a). $\phi$ rotation in (b) is about RD' and finally make $\varphi_2$ rotation about ND'', where these $\varphi_1$, $\phi$, $\varphi_2$ are Euler angles.

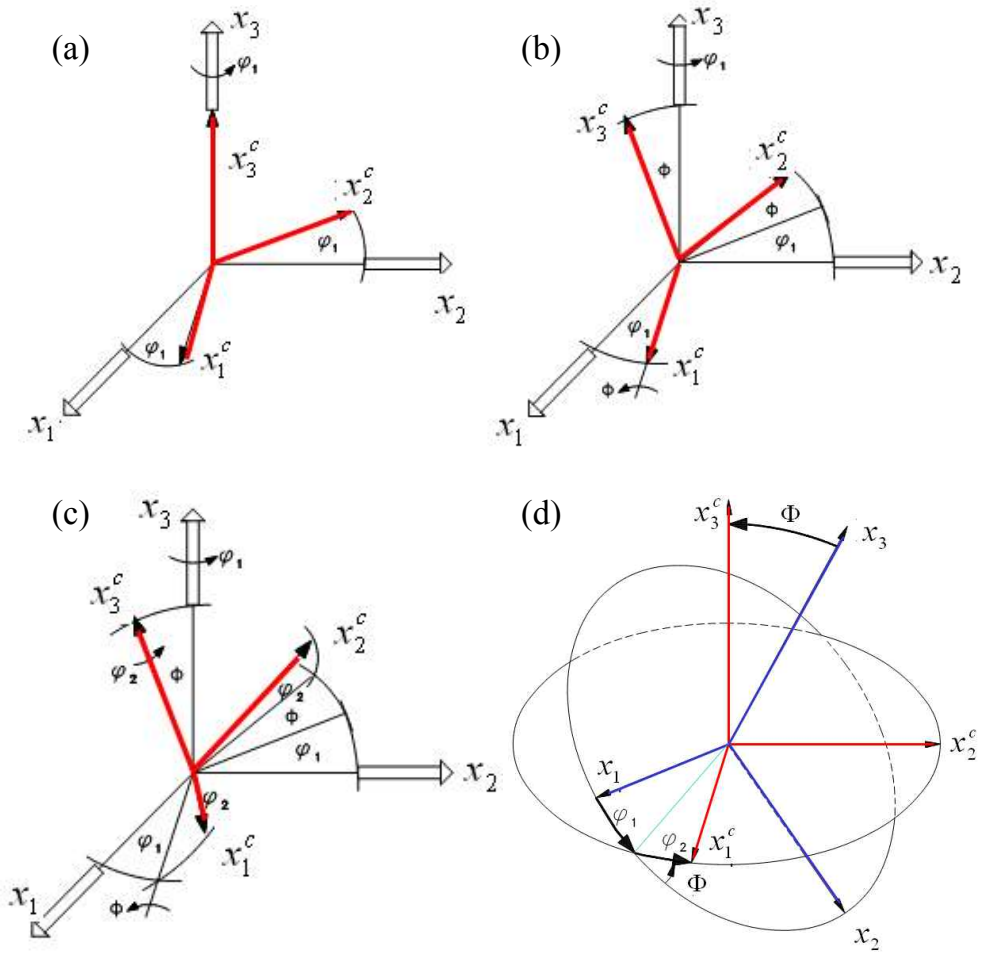


Fig. 3.5 Diagram showing how rotation through the Euler angles describes the rotation between the specimen and crystal axes

(a) $\varphi_1$ about the normal direction ND

(b) $\phi$ about the axis RD'(in its new orientation)

(c) $\varphi_2$ about ND'' in its new orientation)

(d) Sample coordinates ($x_1$, $x_2$, $x_3$) rotation to crystal coordinate ($x^c_1$, $x^c_2$, $x^c_3$)

### 3.2.3 Representation of macroscopic textures

X-ray or neutron diffraction has been introduced as common techniques to determine macroscopic textures and pole figures, inverse pole figures and orientation distribution functions (ODF). There are perhaps the most popular methods to express orientation information from polycrystalline structures. The pole figures plots poles of a certain crystal direction with respect to the specimen coordinate on a stereographic projection. The orientation can be also described by poles of the specimen coordinate system with respect to those of the crystal coordinate system in stereographic projection, which yields the inverse pole figure. For instance, orientation of (124)[$2\bar{1}0$] cubic crystal was expressed using pole figure and inverse pole figure in Figure 3.6 (a) and (b) respectively.

Both of them has been widely used for convenience and simplicity of the stereographic projection, but the projection of the three-dimensional orientation distribution onto a two dimensional pole figure causes a loss in information. Therefore, to permit quantitative evaluation of the texture, it is necessary to describe the orientation density of grains in a polycrystalline in an appropriate three dimensional representation, i.e. in terms of its orientation distribution function, *f(g)* which is normally represented as [37, 38]:

$$\frac{dV(g)}{V_0} = f(g)dg \qquad (3.11)$$

where g is a crystal orientation and $dV(g)$ is total volume of grain between g and $g+\Delta g$. $V_0$ is the total volume of specimen.

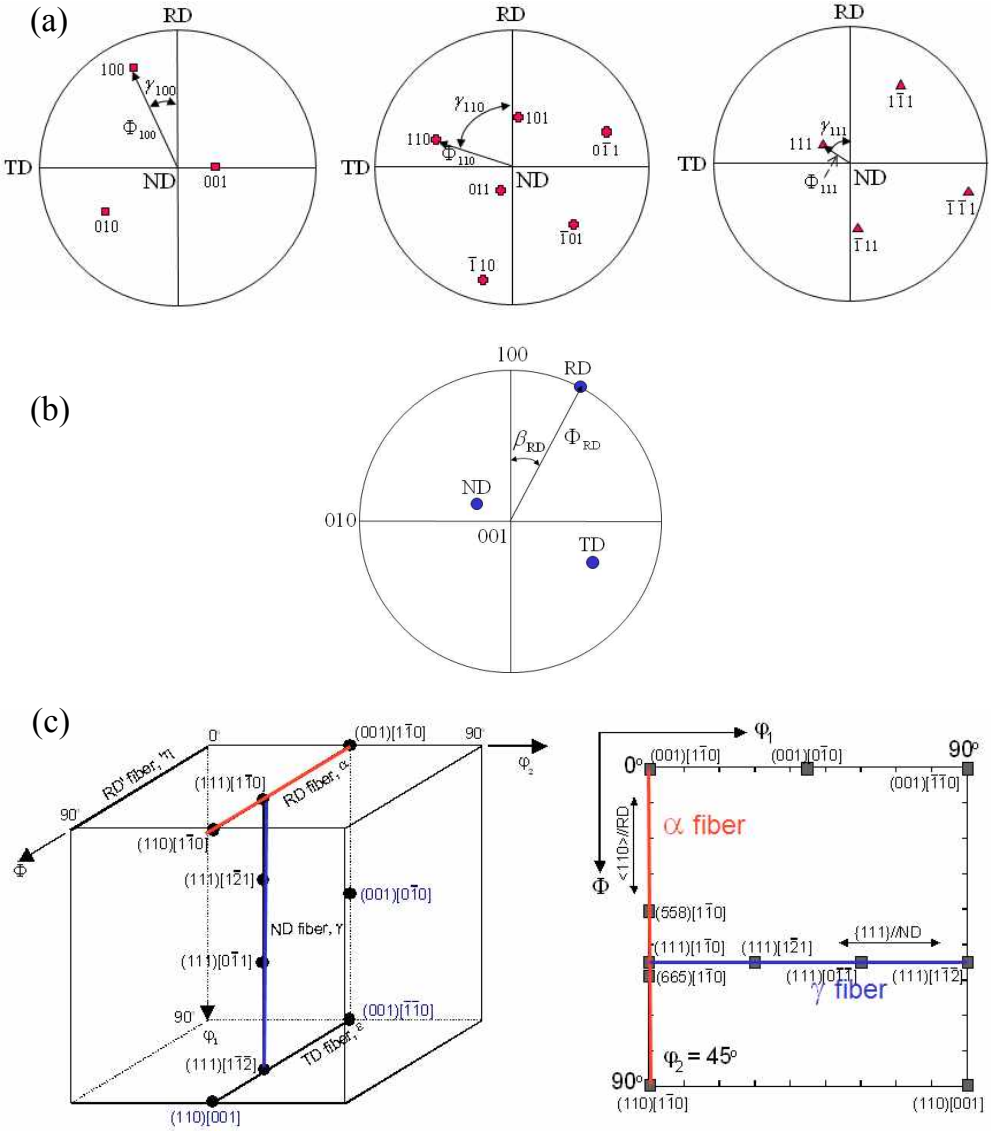


Fig. 3.6 (a) shows (100), (110) and (111) pole figures of (124)[2$\bar{1}$0] cubic crystal and (b) illustrates inverse pole figure of (124)[2$\bar{1}$0]. (c) is a three dimensional view of Euler space with locations of some important ideal orientations and fibers

By using Bunge's spherical harmonics [36], information of orientation density is obtained quantitatively and it is expressed as a multiple of volume fraction in random distribution in Euler space. So, if the value of density is 2, then the volume of certain orientation will be double than the volume of random distribution. Even though the orientation density distribution can be represented by using contour plane, particular section when $\varphi_2$=45° is usually taken to the representative of characteristic texture components. Some important texture components including $\alpha$ and $\gamma$ fiber textures were illustrated in Figure 3.6 (c).

## 3.3 Texture inheritance during transformation

It is often assumed that the orientation relationship between austenite and martensite is close to some rational orientation relationship. Table 3.1 shows some of these rational orientation relationships and they can be also described using the Euler angles shown in Table 3.2. By consideration of the symmetry of the parent crystal a certain number of possibilities present themselves in order to arrange symmetry equivalent planes and directions of both phases parallel to each other. These possibilities are 24 variants for the Kurdjumov-Sachs relationship, 12 for the Nishiyama-Wasserman relationship as well as Pitsch, 3 for the Bain orientation relationship. Table 3.2 is a calculation results from these Euler angles and shows misorientation angles between the rational orientation relationships. However, it has been known that the true orientation relationship must be irrational [1, 4, 39, 40]. It has been assumed that the orientation difference between the rational and irrational

Table 3.1 List of some selected rational orientation relationship commonly used to describe the α/ γ interface

| Orientation relationship | Variants |
|---|---|
| Kurdjumov-Sachs | $\{1\bar{1}0\}_\alpha // \{1\bar{1}1\}_\gamma, <\bar{1}\bar{1}1>_\alpha // <\bar{1}\bar{1}0>_\gamma$ |
| Nishiyama-Wasserman | $\{1\bar{1}0\}_\alpha // \{1\bar{1}1\}_\gamma, <001>_\alpha // <011>_\gamma$ |
| Pitsch | $\{0\bar{1}1\}_\alpha // \{001\}_\gamma, <111>_\alpha // <110>_\gamma$ |
| Bain | $\{0\bar{1}1\}_\alpha // \{001\}_\gamma, <100>_\alpha // <100>_\gamma$ |

Table 3.2 Euler angles by Bunge notation given for the transformation from austenite to ferrite and ferrite to austenite

| Orientation relationship | γ → α | | | α → γ | | |
|---|---|---|---|---|---|---|
| | $\varphi_1$ | $\phi$ | $\varphi_2$ | $\varphi_1$ | $\phi$ | $\varphi_2$ |
| Kurdjumov-Sachs | 5.77° | 48.19° | 5.77° | 5.77° | 48.19° | 5.77° |
| Nishiyama-Wasserman | 9.74° | 45° | 0° | 0° | 45° | 9.74° |
| Pitsch | 0° | 45° | 9.74° | 9.74° | 45° | 0° |
| Bain | 0° | 45° | 0° | 0° | 45° | 0° |

Table 3.3 Misorientation angle between rational orientation relationships

| | KS | NW | Pitsch | Bain |
|---|---|---|---|---|
| KS | - | 5.26° | 5.26° | 11.07° |
| NW | 5.26° | - | 7.44° | 9.74° |
| Pitsch | 5.26° | 7.44° | - | 9.74v |
| Bain | 11.07° | 9.74° | 9.74° | - |

may seem less than a few degrees but is essential because rational orientation cannot lead to the existence of an invariant line which is a condition for martensitic transformation. In this point of view, it is noticeable that orientation relationship between matrix and precipitations during reconstructive transformation has been also observed to be irrational [30, 41-43]. It has been known that this is due to minimize the growth strains and maximize the condition for crystallographic relief of those strains [43].

## 3.4 Variant selection by different transformation mechanism

### 3.4.1 Definition of variant selection

As mentioned in section 3.3, there are particular orientation relationships between precipitates and the matrix. The development of transformation texture in ferrite is therefore always correlated with the original orientation of austenite grains. These relationships can be expressed in terms of the parallelism of certain planes and directions between ferrite and austenite as $\{h_1k_1l_1\}\langle h_2k_2l_2\rangle$, $\{u_1v_1w_1\}\langle u_2v_2w_2\rangle$, where the scripts 1 and 2 refer to the parent and product structures. This variant from the same family of planes and directions and symmetry dictates the total number of variants possible. Sometimes, however, particular variants among them are favoured by some factors such as external stresses or strains etc., which is called '*variant selection'*.

### 3.4.2 Variant selection in displacive transformation

Martensite formation is generally accompanied by a change in volume and a significant transformation shear while reconstructive contains a mixing up of atoms as well as absence of the shape deformation shown in Figure 3.7. It can therefore, be anticipated that the course of the transformation is likely to be affected by the elastic and plastic deformations which result from these phenomenon. Experimental results conducted by Gey et al. [44] show good examples of variant selection during martensitic transformation. Figure 3.8 represents the experimentally determined Cube textured austenite pole figure and ferrite pole figure from the austenite. The experimentally obtained ferrite texture is different from that calculated corresponding to (c) and this clearly shows specific variants should be favoured during transformation.

Based on extreme experimental work, variant selection models have been proposed over the past few decades and some important models and remarks are summarized in Table 3.4. Although detail conditions for variant selection vary, they have a common assumption that martensite variants are favoured when there are externally imposed strains or stresses. This is because the transformation reflect a physical deformation

Table 3.4 Variant selection models in displacive transformation

| Model | Remarks or conditions for variant selection |
|---|---|
| Shape deformation (SD) model [9] | Work by interaction between applied stress and displacive shear should be maximized |
| Bokros-Parker (BP) model [45, 46] | Habit plane should be nearly perpendicular to the active slip plane |
| Active slip system (AS) model [47] | Particular slip systems subjected to the largest shear stresses during rolling before transformation |
| Twining shear (TS) model [5, 8, 48, 49] | Double shear mechanism of martensite crystallography |
| Bain strain (BS) model [50] | Interaction between applied stress of rolling and the Bain strain |

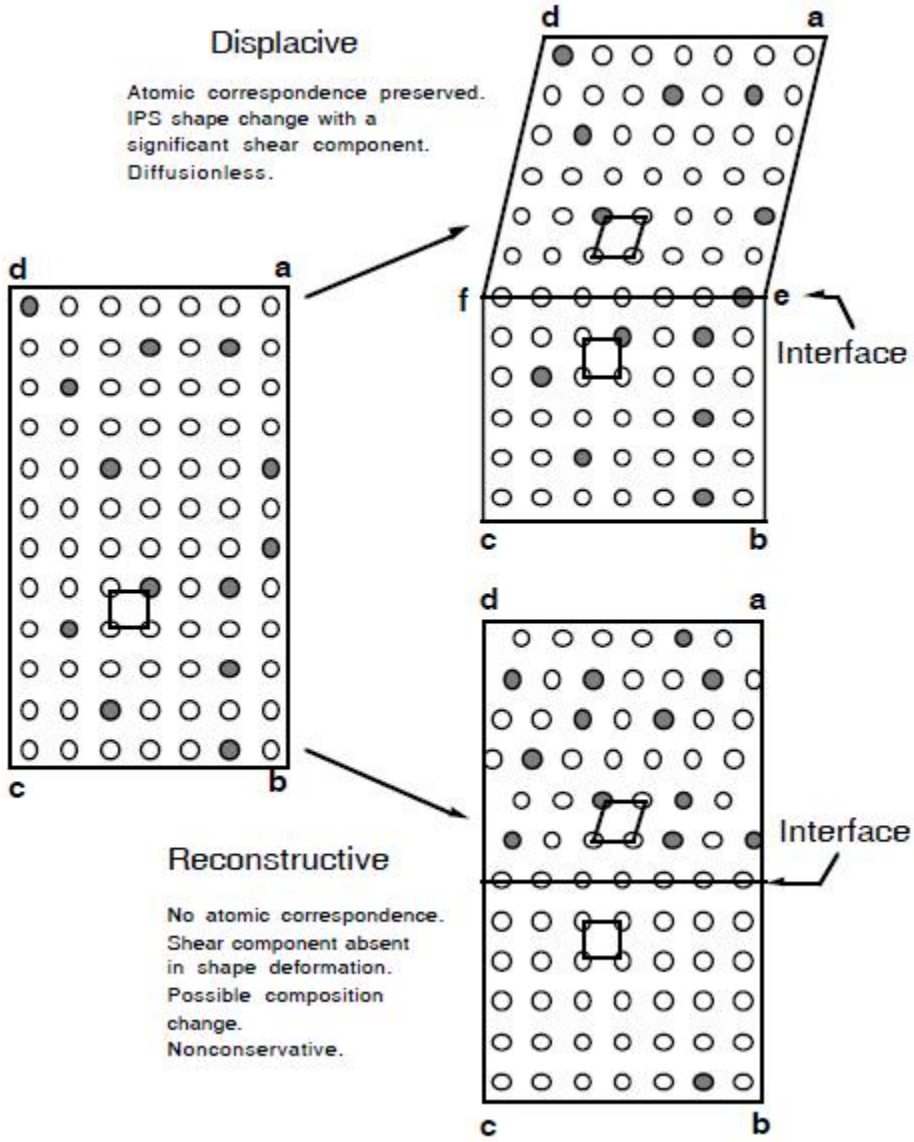


Fig. 3.7 Schematic illustration of mechanisms of displacive and reconstructive transformations [40].

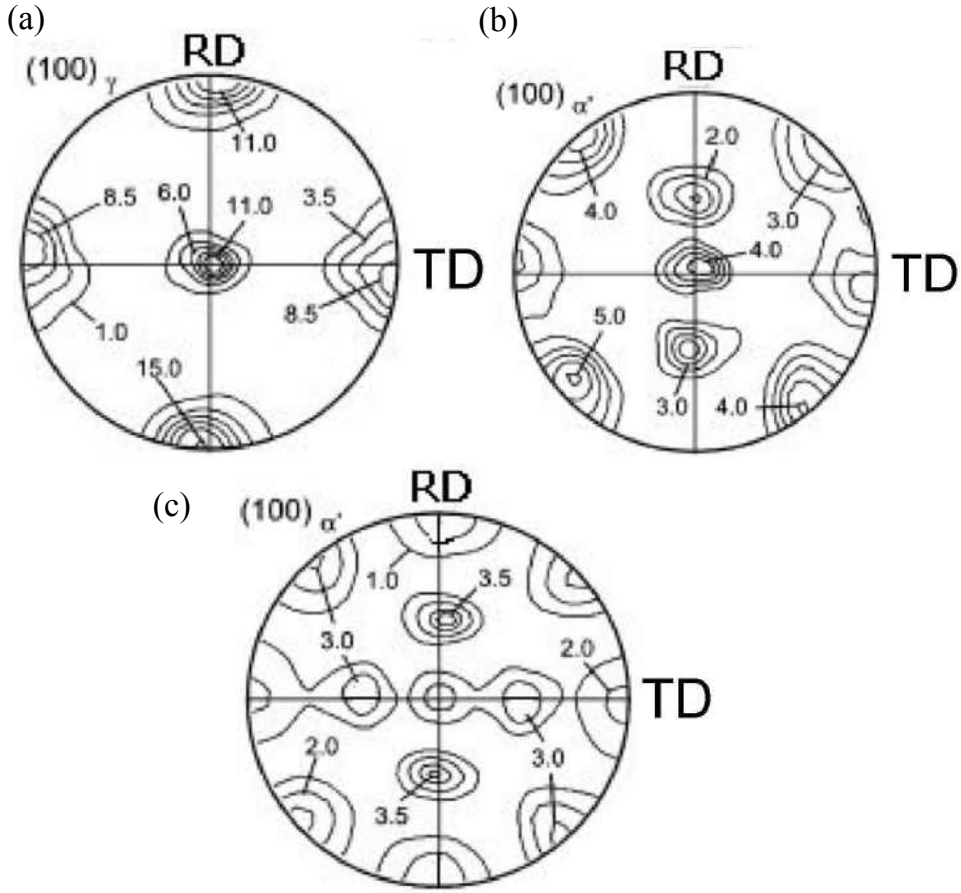


Figure 3.8 (a) Cube type deformation texture in austenite (b) Transformation texture of martensite formed from Cube textured austenite with variant selection. (c) Calculated martensite texture from Cube type austenite texture (without imposing variant selection) [44].

### 3.4.3 Variant selection during reconstructive mechanism

Figure 3.9 shows a comparison between experimentally obtained ODFs of ferrite variants and that theoretically calculated assuming a Kurdjumov-Sachs orientation relationship between the austenite and ferrite [12]. Hot rolling was finished at 815℃ after 80% reduction. As is illustrated in the figure, all variants seem to form in approx equal proportions. Consequently, it describes that there are no favoured ferrite variants due to transformation during hot rolling. This is because transformation by reconstructive mechanism does not lead to a shape deformation so that external stress or strains cannot directly effect on the texture inheritance from austenite to ferrite.

From a microscopic point of view, however, it has been shown that there is local variant selection in the diffusional transformation [51-54]. As mentioned before, low energy orientation relationships in diffusional transformation are due to the minimization of activation energy for nucleation by reducing interfacial energy. So, local variants selection must be related to an interfacial energy minimization criterion. Lee and Aaronson [15, 16] calculated the interfacial energy in various type of ferrite grain formed at austenite grain boundary and Figure 3.10 shows the results according to the inclination angle between a facetted interface and a grain boundary. They suggested that the ferrite whose facetted interface with austenite was closest to the grain boundary would be favored because the activation energy for nucleation decreased as the inclined angle of facetted interface decreased.

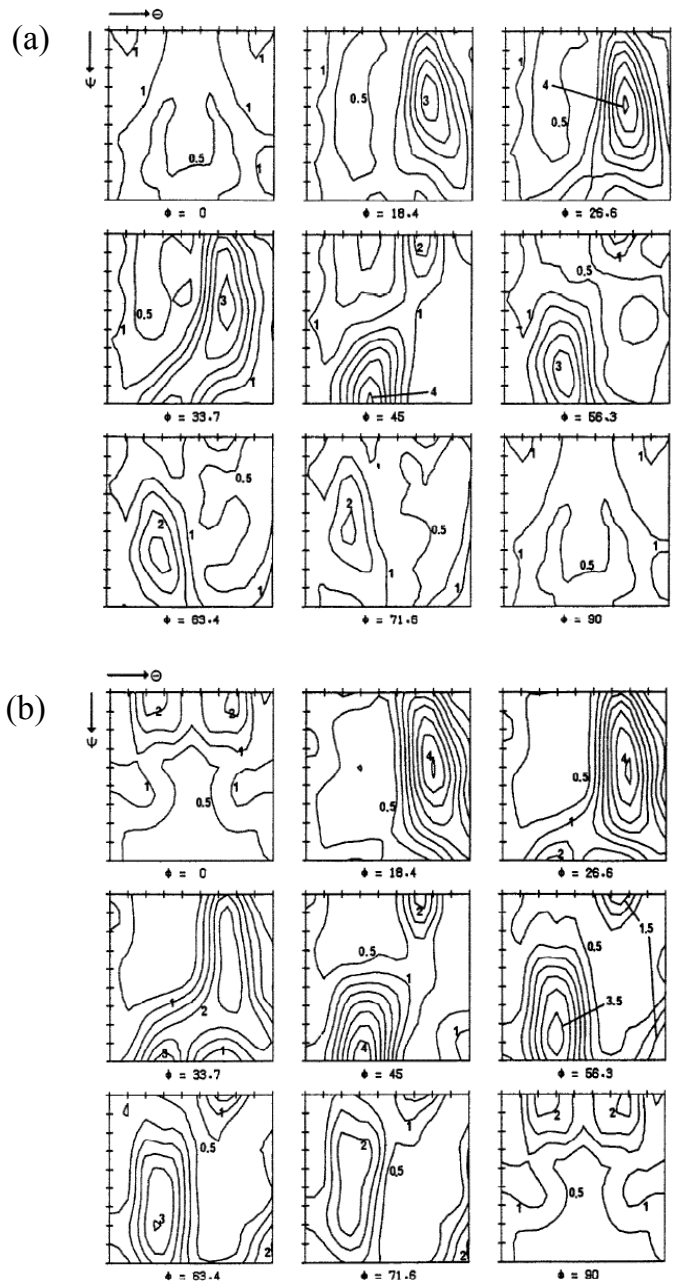


Figure 3.9 (a) ODFs (Roe notation) of ferrite obtained in hot rolled 0.12C-1.47Mn-0.05Nb steel and (b) analytically predicted ODF for ferrite calculated from austenite [12].

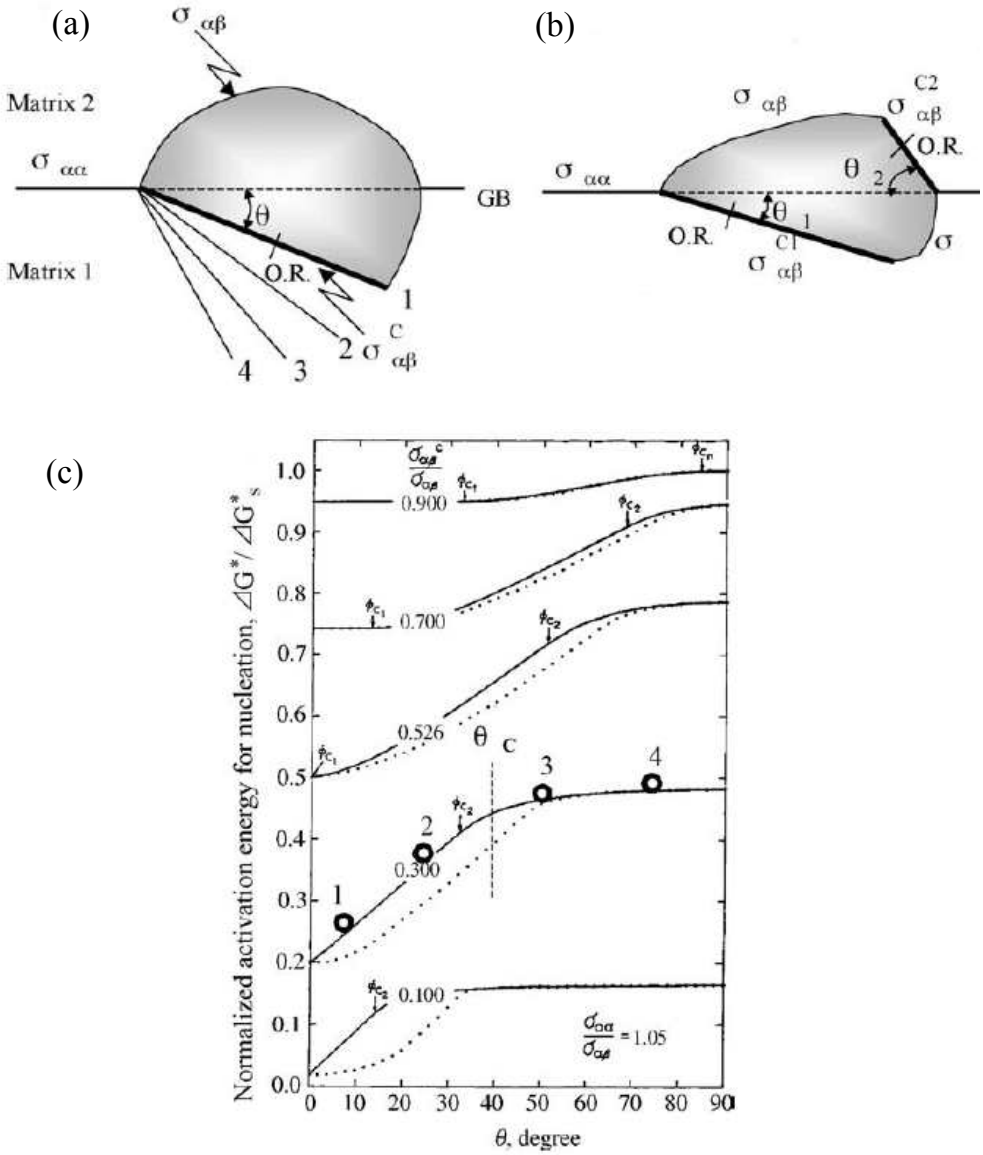


Figure 3.10 Schematic diagram of grain boundary precipitates: (a) one low energy interface and (b) two low energy interfaces. (c) is a change of activation energy for nucleation as a function of a tilt angle to the closest grain boundary of a low energy interface [16].

## 3.5 Comment on variant selection in diffusional transformation

The suggestion by Lee and Aaronson has been consistent with variant selection in diffusional transformation in defined range of inclination angle. However, according to recent reports [42, 51], the criterion leads to difficulties in describing variant selection of precipitates when the inclination angle is larger than $\theta_C$ in Figure 3.10 (c). From calculations, interfacial energy becomes saturated when the inclination is larger than this critical angle. Since there are few benefits in reducing inclination angle when $\theta \geq \theta_C$ in terms of activation energy minimization, it should not affect variant selection.

Adachi et al. [51] have also conducted similar calculations of activation energy due to various nucleation conditions and tried to observed the orientation relationship with respect to the boundary plane orientation. Figure 3.11 shows their calculation results. The activation energy curve shows a similar tendency with results by Lee and Aaronson. They have suggested that precipitates can have a KS orientation relationship even in $\theta \geq \theta_C$ if ferrite has two low energy interfaces (facetted interfaces) because having two such interfaces decreases the activation energy for nucleation. Some 70 allotriomorphic ferrite have been observed in their report and 18 showed double KS orientation relationship. In other words, having two KS orientation relationship which is also called as dual orientation relationship is determined by orientation relationship between adjacent austenite grains and in normal high angle boundary, it is almost impossible to obtain dual orientation [17, 18]. Detain about dual orientation will be discussed in the next chapter.

## 3.6 Summary

Several methods in representing texture and rotation axis have been surveyed. An arbitrary vector was expressed in different crystal coordinates using a rotation matrix, Euler angles as well as axis-angle pairs. To represent macroscopic textures, pole figures, inverse pole figures and orientation distribution functions (ODFs) have been introduced.

Based on a literature review, it is possible to notice that there are certain orientation relationships between austenite and ferrite which are close to a rational relationship such as Kurdjumov-Sachs, Nishiyama-Wasserman, Pitsch and Bain orientation relationships. However, in real cases, there should be an irrational orientation relationship which lead to an invariant line in the interface, because this is necessary to permit glissile interfaces between $\gamma$ and $\alpha$' or because the coherency correlated with the invariant line leads to a reduction in interfacial energy. Basically symmetrical variants have equal possibility of occurrence however; we could see that sometimes particular variants are favoured due to the effect of externally imposed stresses or strains on the shape deformation during transformation. Since reconstructive transformation occurs by long-range atomic diffusion without invariant plane strains, there were no effects of external deformation on the variant selection only except local variant selection by activation energy minimization. However, criteria based on the Lee and Aaronson's calculation have proven to be inexact for certain large facet interface inclination

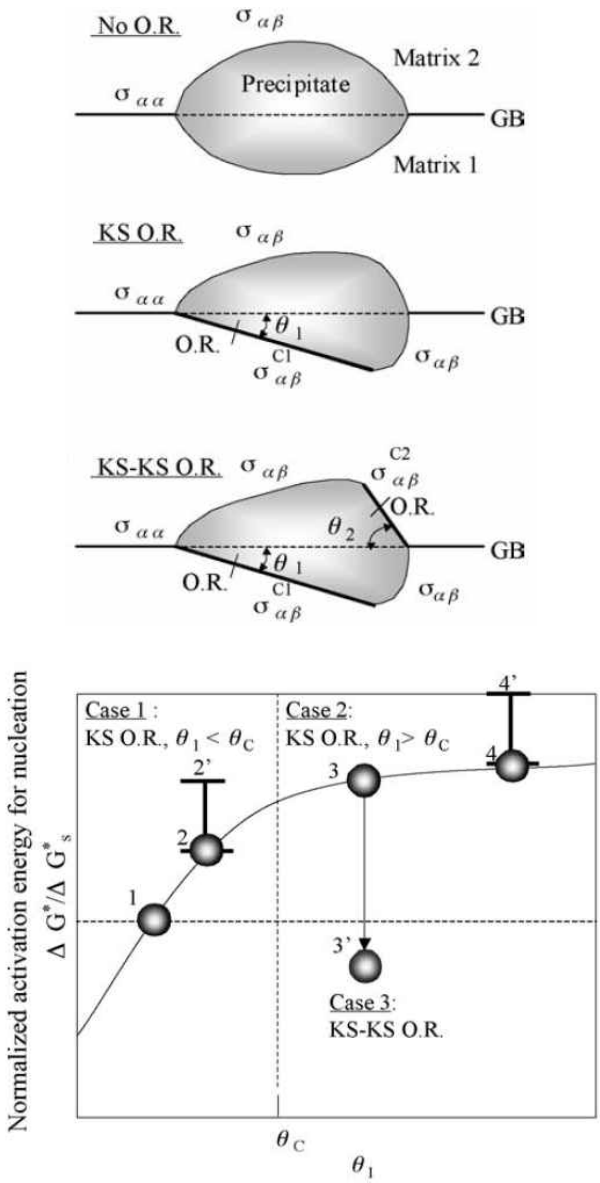


Figure 3.11 Schematic diagrams of grain boundary precipitates and a change of activation energy for nucleation as a function of a tilt angle.

# Chapter 4: Dual Orientation and Variant Selection during Diffusional Transformation

## 4.1 Introduction

With the advent and popularity of electron backscattered diffraction and orientation imaging microscopy [55-57], there has been renewed interest in the concept of crystallographic grain size as opposed to the metallographic grain size. The latter is a measure of the amount of grain surface per unit volume, irrespective of the misorientations between adjacent grains as long as the boundaries can be detected by the metallographic method used.

The former on the other hand, indicates distances over which there is little variation in crystallographic orientation in spite of intervening grain boundaries. The crystallographic grain size is particularly relevant in understanding the toughness of steels because it determines the percolation and roughness of cracks through the structure [58-63]. Whereas a great deal is known about the control of the metallographic grain size, work on crystallographic grain size control is in its infancy. The mathematical framework needed to do this would rely on the ability to calculate transformation textures.

In the case of displacive transformations such as bainite and martensite, the set consisting of the orientation relationship, shape deformation and habit plane is uniquely defined by the phenomenological theory of martensite [1, 2, 35, 64]. It follows that given the orientation distribution of the austenite grains that of each

martensite plate can be calculated relative to the sample reference frame in order to estimate the crystallographic texture, including the effects of variant–selection due to an externally imposed system of stresses [4, 65-67]. An interesting simplification is that because martensite plates are confined to the grains in which they grow, it is not necessary to identify the relative physical locations of individual austenite grains in order to calculate the texture; the calculations can be done independently for each austenite grain and then summed to give the overall texture.

The situation is rather different for transformations which involve the diffusion of all atoms (allotriomorphic ferrite, pearlite), because the transformation products are then able to traverse austenite grain boundaries [19, 68] as illustrated in Figure 4.1. The conventional wisdom is that an allotriomorph ($\alpha$) will nucleate at an austenite grain boundary with a low–energy orientation relationship with one of the austenite ($\alpha/\gamma_2$) grains and a random orientation with the other grain ($\alpha/\gamma_1$) with which it has contact. One side of the allotriomorph will then have a facetted appearance and the other should exhibit a curved boundary. There is, however, long–standing evidence to suggest that an allotriomorph may have a low–energy orientation with both the adjacent austenite grains [28, 30, 69, 70].

These conclusions naturally depend on the degree of deviation from the low–energy orientation. The purpose of the present work was to examine theoretically the chances of an allotriomorph simultaneously achieving a low–energy orientation with both the adjacent austenite grains, as a function of the texture of the original austenite and the precision with which a low–energy orientation is defined. Unlike

martensite, it is necessary in such a model to define the neighbors and orientations of each austenite grain.

## 4.2 Calculation method for dual orientation possibility

### 4.2.1 Methodology for drawing texture

As it mentioned in section 3.2.3, pole figure which is one of the most popular methods to express macroscopic orientation is a representation of particular planes in the crystal coordinate with respect to the sample coordinate system using the stereographic projection. Therefore, orientation of particular variants in crystal can be represented due to the sample coordinate if we know the geometrical position of projected pole in RD (rolling direction) – TD (transverse direction) plane. When crystal is positioned in the center of sphere as illustrated in Figure 4.2 (a), a pole of certain plane P makes its projection in x-y plane (b). For example, we assume this x-y plane corresponds to the RD-TD plane and express all possible poles of {111} planes in positive and negative hemispheres, these poles are projected at 4 points in RD-TD plane. Supposing the sphere has unit radius, then pole P' can be expressed by a unit vector with components [*u, v, w*]. Due to the similar figure of triangle in (d), OP'' is same as 1/ (1+*w*) and 1/ (1-*w*) when P' is in the positive and negative hemisphere respectively. Thus, P'' is represented in RD-TD with [u/ (1$\pm$w), v/ (1$\pm$w)].

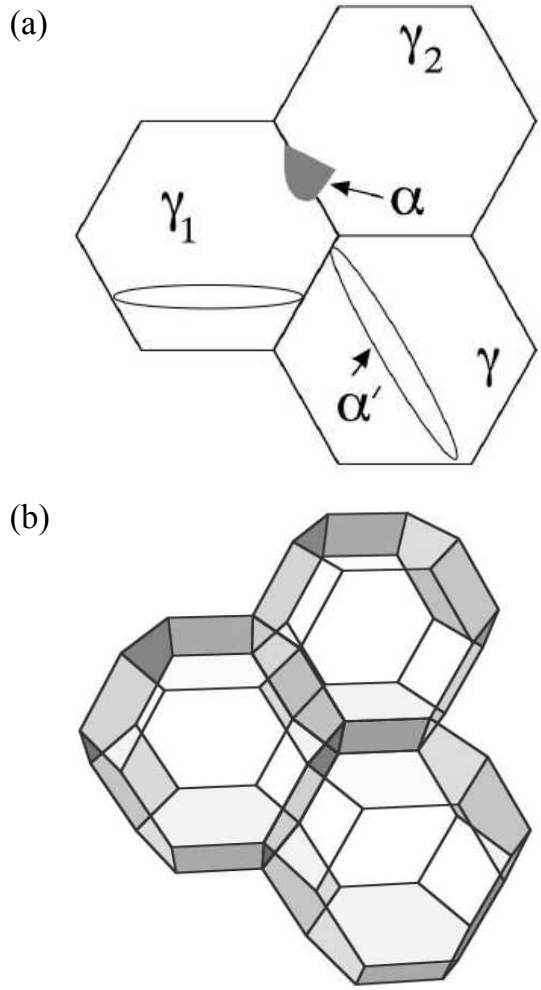


Figure 4.1 (a) martensite plates are confined to the austenite grain in which they nucleate whereas allotriomorphs are not. α and $\gamma_2$ are in a low–energy orientation whereas that between $\alpha$ and $\gamma_1$ will in general be random. (b) space–filling stack of tetrakaidecahedra with a few of the neighbors defined.

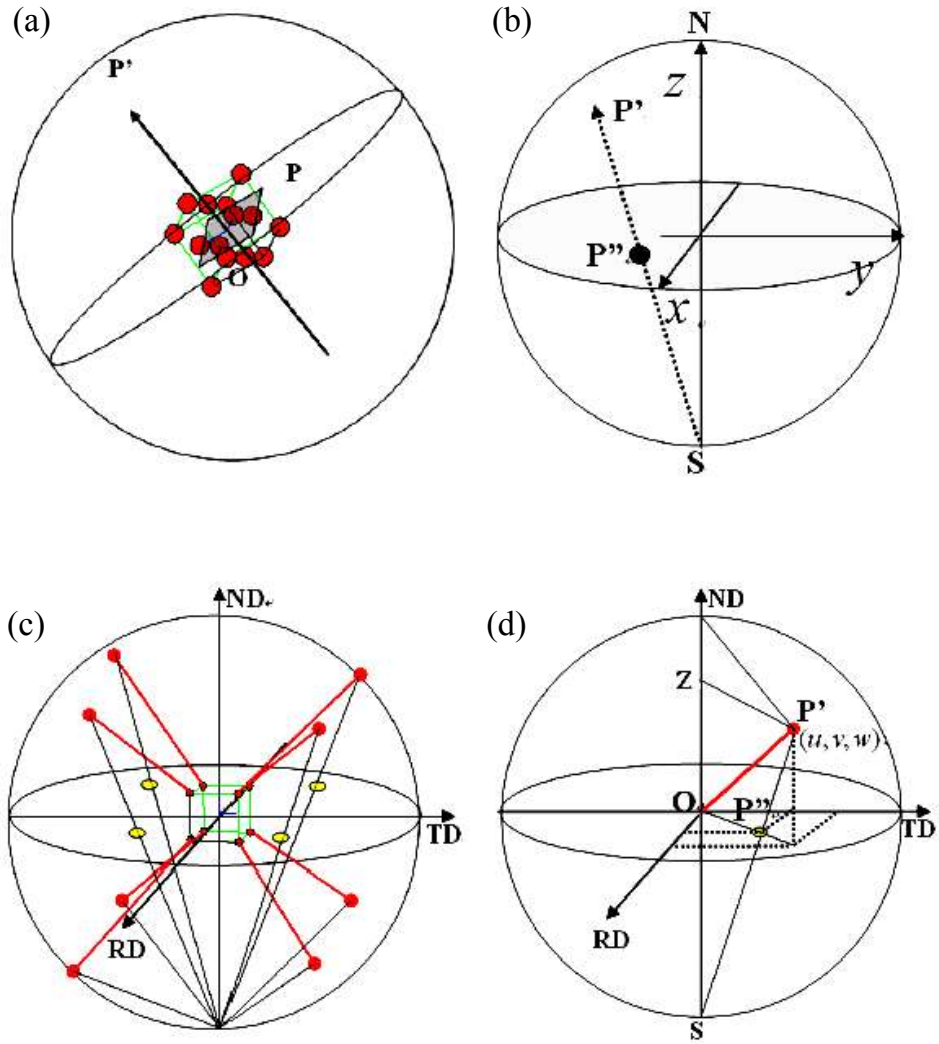


Figure 4.2 (a) a pole P' shows particular plane in crystal and (b) P'' is a projection of P' in x-y plane. (c) 4 variants of {111} plane in crystal projected in RD-TD planes and (d) methods to obtain the geometrical position of P'' in RD-TD plane.

### 4.2.2 Austenite grain structure

Austenite grains are conveniently represented as a stack of identical, space–filling Kelvin tetrakaidecahedra [71-75], each of which consists of eight hexagonal and six square faces, with 36 equal edges, as illustrated in Figure 4.1 (b). For ferrite nucleation at austenite grain surfaces, there are therefore 14 face–sites per grain.

The computer algorithm was constructed so that for each grain orientation relative to the sample frame of reference, it was possible to access the orientations of the fourteen neighboring grains. A total of 1700 austenite grains were created in this way, with one of the grains having its crystallographic axes exactly parallel to those of the sample. The relationship between the sample and austenite crystal axes can be described using Euler angles $\varphi_1$, $\phi$ and $\varphi_2$. These are the three angles by which the sample reference frame must be rotated in order to coincide with that of the crystal. The rotation matrix relating the frames is given by:

$$\begin{pmatrix} \cos\varphi_1\cos\varphi_2 - \sin\varphi_1\cos\phi\sin\varphi_2 & \sin\varphi_1\cos\varphi_2 + \cos\varphi_1\cos\phi\sin\varphi_2 & \sin\phi\sin\varphi_2 \\ -\cos\varphi_1\sin\varphi_2 - \sin\varphi_1\cos\phi\cos\varphi_2 & -\sin\varphi_1\sin\varphi_2 + \cos\varphi_1\cos\phi\cos\varphi_2 & \sin\phi\cos\varphi_2 \\ \sin\varphi_1\sin\phi & -\cos\varphi_1\sin\phi & \cos\phi \end{pmatrix} \tag{4.1}$$

To generate a random set of austenite grain orientations, the Euler angles $\varphi_1$ and $\varphi_2$ (ranging from 0 to 2π) and the value of $\cos\phi$ (between ±1) were selected using a random number generator [36]. Non–random austenite textures were generated relative to the sample axes by setting the first austenite grain to the exact required texture, and then choosing relative to this grain, random rotation axes but

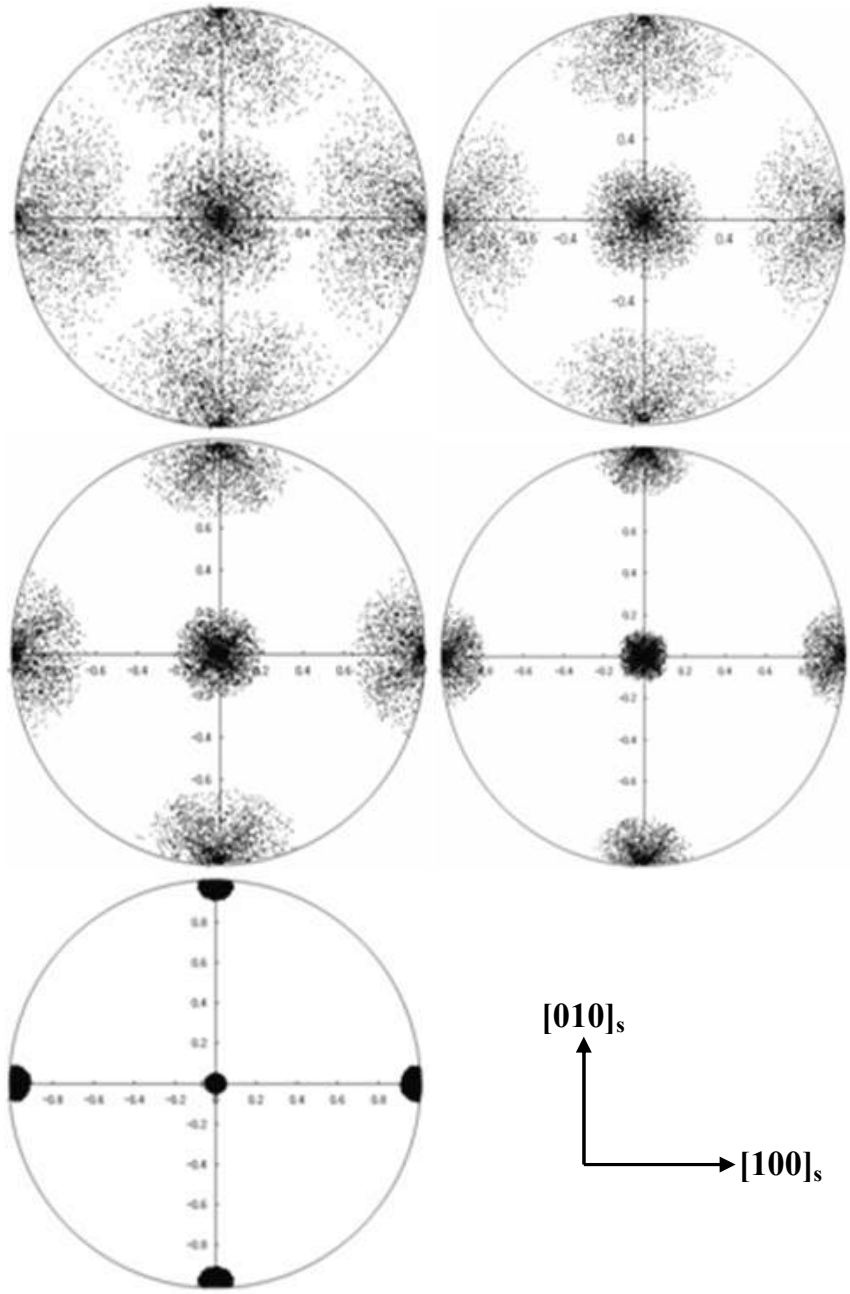


Figure 4.3 Modeled austenite Cube textures as a function of the limiting value of θ.

The (100) pole figures are all plotted relative to the sample axis 'S'.

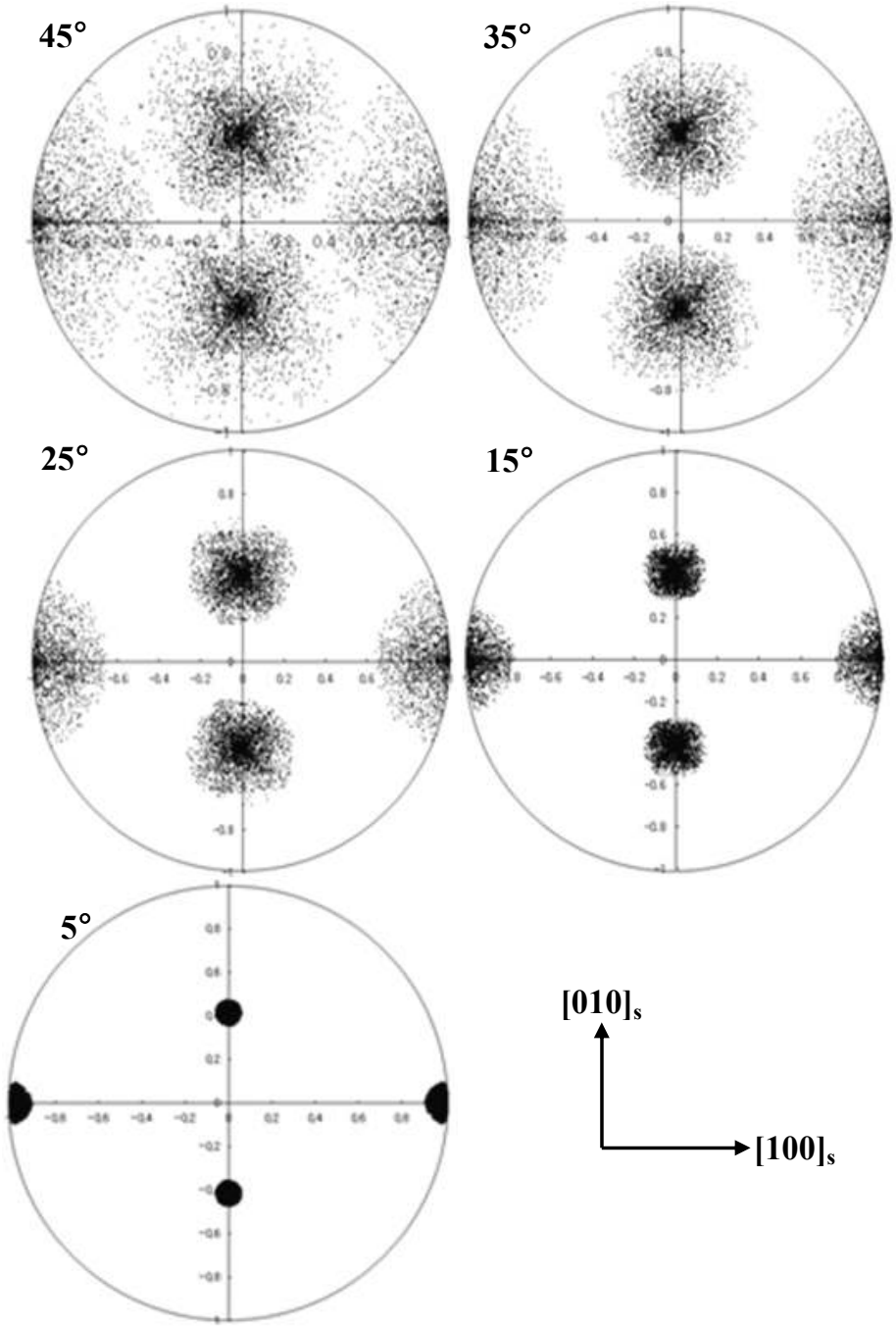


Figure 4.4 Modeled austenite Goss textures as a function of the limiting value of θ.

The (100) pole figures are all plotted relative to the sample axis 'S'.

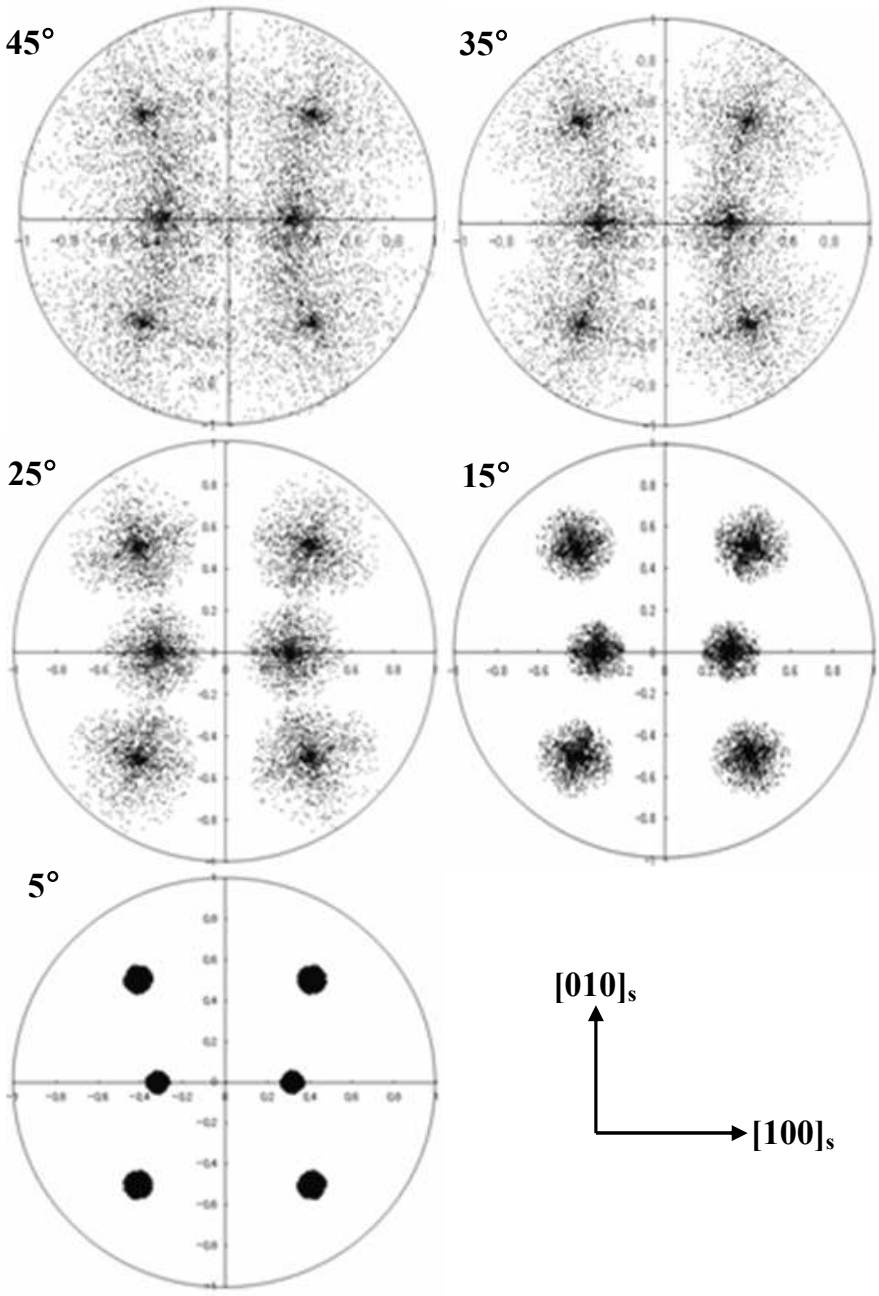


Figure 4.4 Modeled austenite Copper textures as a function of the limiting value of θ. The (100) pole figures are all plotted relative to the sample axis 'S'.

with the right–handed rotation angle limited to the range θ=0~45°[4]; the Goss, Cube and Copper textures were generated in this way and the effect of the limiting value of θ is illustrated in Figure 4.3 to Figure 4.5.

### 4.2.3 Introduction of ferrite texture

In the previous chapter, we could confirm that any grain of martensite or bainite will always have a strict low energy orientation relationship, ($\alpha$ $J_{LE}$ $\gamma$) where $J_{LE}$ marks a low-energy orientation coordinate transformation. It has been assumed deviation angle between rational orientation such as Kurdjumov Sachs and irrational orientation seems less than a few degrees, but it has been known to be essential for displacive transformation due to existence of invariant planes and directions. As it mentioned in section 3.3, however, the most coherent relationships even in reconstructive transformations are likely to be irrational perhaps due to the difference of lattice parameters. We therefore, adopt as the low-energy orientation, one predicted by the crystallographic theory of martensite in order to ensure this irrational orientation relationship between α and γ:

$$(\gamma \quad J_{LE} \quad \alpha) = \begin{pmatrix} 0.579356 & 0.542586 & 0.102537 \\ 0.014470 & 0.133650 & -0.788984 \\ -0.5520000 & 0.572979 & 0.086936 \end{pmatrix} \tag{4.1}$$

Thus,

$$(1\bar{1}1)_{\gamma} = (0.012886 \;\; 0.981915 \;\; 0.978457)_{\alpha} \tag{4.2}$$

$$(011)_{\gamma} = (\overline{0.53753} \;\; 0.706629 \;\; \overline{0.702048})_{\alpha} \tag{4.3}$$

This means that $(1\bar{1}1)_\gamma$ is 0.54° from $(011)_\alpha$ and very nearly parallel though not exactly parallel to $(011)_\alpha$ and $[1\bar{1}1]_\gamma$ is 6.91° from $[\bar{1}1\bar{1}]_\alpha$. This is close to the Kurdjumov–Sachs orientation but is irrational and allows for the existence of a coherent line between the two lattices.

When ferrite was allowed to form on a face between two austenite grains with relative orientation ($\gamma_1$ J $\gamma_2$), Figure 4.1 (a), the corresponding orientations with the ferrite are ($\gamma_1$ J $\alpha$) and ($\gamma_2$ $J_{LE}$ $\alpha$) where the latter is the low–energy variant. It follows that

$$(\gamma_1 \quad J \quad \alpha) = (\gamma_1 \quad J \quad \gamma_2)(\gamma_2 \quad J_{LE} \quad \alpha) \tag{4.4}$$

Both the matrices on the right–hand side of this equation are known because the austenite orientations are set initially and ($\gamma_2$ $J_{LE}$ $\alpha$) is given by Equation 4.1. Ferrite was allowed to nucleate on all 14 faces of each austenite grain. The ferrite in all cases had a low–energy orientation with one austenite grain; since there are 24 crystallographically equivalent such orientations for any given austenite grain, the selection of the particular variant was made at random from the 24 available. The possibility that ($\gamma_1$ J $\alpha$) is close to a low–energy orientation was investigated by studying its deviation from all 24 variants of ($\gamma_1$ $J_{LE}$ $\alpha$). This is done by calculating

$$(\gamma_1 \quad \Delta J \quad \gamma_1) = (\gamma_1 \quad J \quad \alpha)(\alpha \quad J_{LE} \quad \gamma_1) \tag{4.5}$$

where ($\alpha$ $J_{LE}$ $\gamma_1$) is the inverse of ($\gamma_1$ $J_{LE}$ $\alpha$). The axis–angle pair corresponding to $\Delta J$ was calculated; because of the symmetry of the cubic system, for each axis–angle pair there are 23 crystallographically equivalent sets. The particular set with the

lowest angle of rotation ($\Delta$) was selected to assess the closeness of the orientation ($\gamma_1$ J $\alpha$) to the low–energy case. The case where ferrite grain has an exact low–energy orientation with one austenite grain, and at the same time an approximately low–energy orientation (as defined by the maximum permitted deviation $\Delta = \Delta_{max}$) with the adjacent austenite grain is henceforth referred to as a dual orientation for convenience. The procedure was repeated for every single ferrite grain and the resulting transformation texture studied alongside the probability of finding a dual orientation.

## 4.3 Calculated ferrite textures

It is important to note that the issue is to find the probability of the dual orientation phenomenon. The ferrite orientations are therefore studied relative to those of the austenite grains. In contrast, the texture of the austenite prior to transformation is defined relative to the sample frame of reference. The orientation of the austenite texture relative to the sample axes is not relevant to the prediction of the transformation texture relative to the austenite frame of reference. For this reason, the results presented in Figure 4.5 and Tables 4.1, 4.2 are almost identical for all three varieties of austenite texture (Goss, Cube and Copper), any differences arising because of the stochastic process of generating the initial austenite textures.

It is worth pointing out that in Table 4.1, the percentage of dual orientation is exceptionally large when $\Delta_{max} \geq \theta$. This is expected since the the misorientations

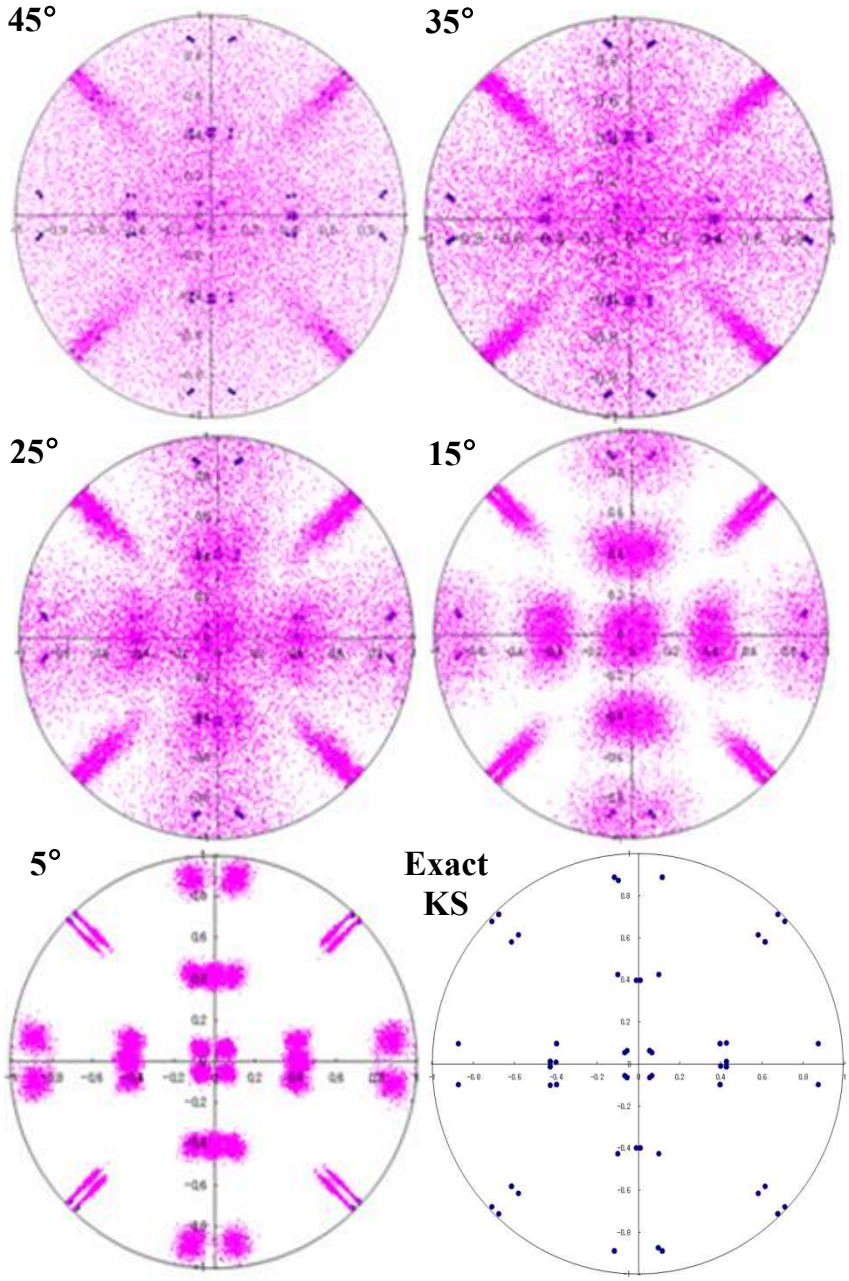


Figure 4.5 Modeled ferrite textures as a function of the limiting value of θ. The (100) pole figures are all plotted relative to the austenite axis 'γ'.

Table 4.1 Calculated percentages of dual orientation as a function of the strength of the austenite texture (related to the angle θ). The dual orientation is here defined for all orientations within $\Delta_{max}=15°$ of the low energy orientation

| Rotation angle, θ | Dual orientation possibility (%) | | | |
|---|---|---|---|---|
| | Random | Cube | Goss | Copper |
| 5 | 1.53 | 100 | 100 | 100 |
| 15 | | 45.6 | 45.3 | 45.0 |
| 25 | | 20.7 | 21.5 | 21.2 |
| 35 | | 11.4 | 11.4 | 12.2 |
| 45 | | 7.6 | 7.1 | 7.3 |

Table 4.2 Calculated percentages of dual orientation as a function of the strength of the austenite texture (related to the angle θ). The dual orientation is here defined for all orientations within $\Delta_{max}=5°$ of the low energy orientation

| Rotation angle, θ | Dual orientation possibility (%) | | | |
|---|---|---|---|---|
| | Random | Cube | Goss | Copper |
| 5 | 0.05 | 45.8 | 45.3 | 45.6 |
| 15 | | 7.3 | 7.3 | 7.3 |
| 25 | | 2.8 | 2.7 | 2.8 |
| 35 | | 1.6 | 1.7 | 1.7 |
| 45 | | 0.8 | 0.8 | 0.8 |

between austenite grains are then smaller than the spread allowed in the definition of the state of dual orientation. The results are interesting because the chance of obtaining a dual orientation when the austenite grains are randomly disposed is found to be negligible. The probability naturally increases as the polycrystalline aggregate tends towards a stronger texture (lower $\theta$), i.e., towards a single crystal.

It should be emphasized that a value of $\Delta_{max}$ as large as $15^\circ$ is a substantial deviation from the low–energy orientation and in general cannot be capable of sustaining an invariant line between the $\gamma$ and $\alpha$. The same applies to $\Delta_{max} = 5^\circ$ so the concept of dual orientation should not be taken to imply that both sides of the allotriomorph (i.e., $\alpha/\ \gamma_1$ and $\alpha/\ \gamma_2$) are capable of developing into displacive transformation products such as Widmanstätten ferrite [76, 77] as is sometimes implied [68, 78]. Displacive transformation requires the existence of the invariant–line. This means that any observation of Widmanstätten ferrite developing from the deviant $\alpha/\ \gamma_1$ side of the allotriomorph will have a low–misorientation boundary between the Widmanstätten ferrite and allotriomorphic ferrite. Such misorientations should be detectable using electron backscattered diffraction methods.

In order to decide on the significance of a particular kind of dual orientation associated with a specific value of $\Delta_{max}$, it is necessary to define a purpose for calculating or measuring the probability of dual orientations. For example, when considering the percolation of cracks through the polycrystalline aggregate, it is the parallelism of cleavage planes in different grains along the crack path that matters. The angle through which the cleavage plane must deviate in order to arrest or

significantly retard its propagation can be used to decide on an appropriate value of $\Delta_{max}$.

## 4.4 Grain edge and corner nucleation

When ferrite nucleates at austenite grain edges it is in contact with three austenite grains. Since the assumption is that the ferrite has a low–energy orientation with one of these austenite grains, the chance of obtaining a dual orientation with at least one of the remaining two austenite grain doubles. Thus in Table 4.1, all of the percentages can be doubled to represent edge nucleation. In the case of corner nucleation, the ferrite grain is in contact with four austenite grains so that the possibility of dual orientation triples. This means that when $\Delta_{max} \geq 2\theta$, the chance becomes 100%, although as emphasized previously, the relevance of a dual orientation diminishes as $\Delta_{max}$ increases relative to the strength of the austenite texture. Although the activation energy for heterogeneous nucleation decreases in the order face→edge→corner, the number density of nucleation sites also decreases in the same order. For this reason, corner nucleation dominates at low undercoolings below the equilibrium transformation temperature and grain–face nucleation at large undercoolings [24]. It follows that the chances of obtaining dual orientations are larger when transformations are carried out at low undercoolings or at very slow cooling rates during continuous cooling.

## 4.5 Summary

If the concept of dual orientation is taken to imply that exact variants of a strict low–energy orientation relationship exists between an allotriomorph and more than one adjacent austenite grain, then the probability of this happening is negligibly small even in strongly textured austenite. However, if the definition is less exacting with deviations of 5° or more permitted, then there is a detectable chance of finding such allotriomorphs. Care must be exercised in setting the level of deviation by identifying the purpose of the work so that the interpretation of the outcome can be treated in context. The calculations here do not allow for experimental error in the determination of orientation relationships, which must add to the chances of falsely detecting dual orientations. It is suggested therefore that any experimental study of the dual orientation phenomenon should report the parameters $\Delta_{max}$, $\theta$ and the error of the experimental method used.

# Chapter 5: New type of Dual Orientation at Special CSL boundaries

## 5.1 Introduction

An allotriomorph ($\alpha$) will in general adopt a low-energy orientation relationship with one of the austenite grains and a random orientation with the other grain with which it has contact. There is, however, long-standing evidence to suggest that of the 24 ferrite-orientations possible in a given austenite crystal, that which is favoured is the one which is able to simultaneously match with both the adjacent austenite grains [28, 30, 69, 70]. In contrast, probability of the dual orientation has been demonstrated by calculation as a function of the deviation angle from rational orientation, $\Delta_{max}$ and the strength of austenite texture which is related to the rotation angle, $\theta$ (Chapter 4) that the probability of simultaneous matching is small even when the parent austenite exhibits macroscopic crystallographic texture.

Ferrite, which is able to achieve a low-energy orientation with both austenite grains, is said to exhibit a 'dual orientation', and such simultaneous matching can only occur for some of the 24 possible orientations; this then provides a mechanism for variant selection during phase transformation. Note that there is a certain amount of subjectivity in claiming the existence of dual orientations because of experimental error and because it is necessary first to define an acceptable level of deviation from an ideal low-energy orientation [18]. In the course of some crystallographic investigations, another phenomenon has been discovered which

may increase the probability of dual orientations, i.e. when the adjacent austenite grains are oriented in such a way that there is a large proportion of lattice points, which are common to the two grains (coincidence site lattices).

## 5.2 Experimental procedures

### 5.2.1 Heat treatment

The chemical composition of the experimental alloy used is Fe–0.595C–0.98Si–1.10Mn–1.50Al wt. %. It is designed so that a small amount of allotriomorphic ferrite can be generated at a relatively high temperature, followed by isothermal transformation to bainitic ferrite and retained austenite. Nearly 20% of austenite is retained in the final microstructure, permitting its crystallographic orientation to be determined without ambiguity. The samples geometry is illustrated in Figure 5.1 (up); the active region was cylindrical, 5 mm diameter and 10 mm long, for use in a push rod BAHR DIL-805 high speed dilatometer with radio frequency induction heating. The procedure is illustrated in Figure 5.1 (down). The sample was first austenitised by heating at 9℃/ s to 1, 200℃ and holding there for 10 min, followed by cooling to the 740℃ where it was held for 15 min to generate allotriomorphic ferrite; it was then quenched to 450℃ for isothermal transformation into bainitic ferrite for 10 min. The cooling rate during each of the steps was 60℃/ s to avoid any unintentional phase transformation. The sample was deformed in tension, by 15% uniform elongation prior to the onset of the ferrite transformation. Note that there is

a significant time gap between the end of deformation and the beginning of ferrite formation.

### 5.2.2 EBSD measurement and accuracy of observations

All samples were etched with 2 vol. % nital solution and areas were identified using microhardness indents for further examination in a scanning electron microscope. The surface of the sample is usually deformed during metallographic preparation, so the indented samples were polished using colloidal silica for 3 min. The orientations of allotriomorphic ferrite and austenite were measured using electron back scattered diffraction (EBSD) on a ZEISS SUPRATM scanning electron microscope.

It is important to comment on the accuracy of the EBSD observations as applied in the present work so as to avoid over-interpretation of the experimental data. Figure 5.3 and 5.4 show stereograms where for perfect and very large crystals, each pole would effectively be a point. However, the retained austenite is in a finely divided state and that contributes to a broadening of diffracted beams; it also will contain dislocations generated by the formation of bainite [79] which result in strain broadening.

Figure 5.3 (a) shows that the angular spread of the individual poles of austenite is much larger than that of the allotriomorphic ferrite, Figure 5.3 (b), which is expected since the ferrite is relatively coarse and grows by diffusional transformation and hence does not inherit the defect structure of the parent phase.

The diffraction from the austenite deteriorates further when it is plastically deformed at 740 ℃, as illustrated in Figure 5.4 (a). We estimate that the poles of austenite are in fact spread over about 5° and those of ferrite over 2°. These values indicate the precision of the measurements reported below and any interpretations must be made in that context.

## 5.3 Numerical method

Whereas the Kurdjumov–Sachs and Nishiyama–Wasserman type orientations are frequently quoted as the orientation adopted by allotriomorphic ferrite, the actual observations usually assume that a $\{110\}_\alpha$ plane is exactly parallel to a $\{111\}_\gamma$ plane. However, techniques such as conventional electron diffraction and EBSD do not have sufficient precision to reach this conclusion. The relationship selected here to represent a low-energy orientation is Kurdjumov–Sachs, simply for the pragmatic reason that it represents a more general case with 24 crystallographic variants per austenite grain, whereas the exact Nishiyama–Wasserman relation only results in 12 such variants. Since the actual orientation relation is likely to be irrational, one must expect 24 variants; the methodology used in this work applies whatever the actual orientation relationship. A specific variant (say number 1) of the Kurdjumov–Sachs orientation can be represented by a rotation matrix:

$$\left(\gamma \quad \mathrm{J}_{\mathrm{LE}}^{1} \quad \alpha\right) = \begin{pmatrix} 0.741582 & -0.66667 & 0.074915 \\ 0.649813 & 0.741582 & -0.166667 \\ 0.166667 & 0.074915 & 0.983163 \end{pmatrix} \qquad (5.1)$$

The other $i$ = 2 to 24 variants can be generated by applying the symmetry operations

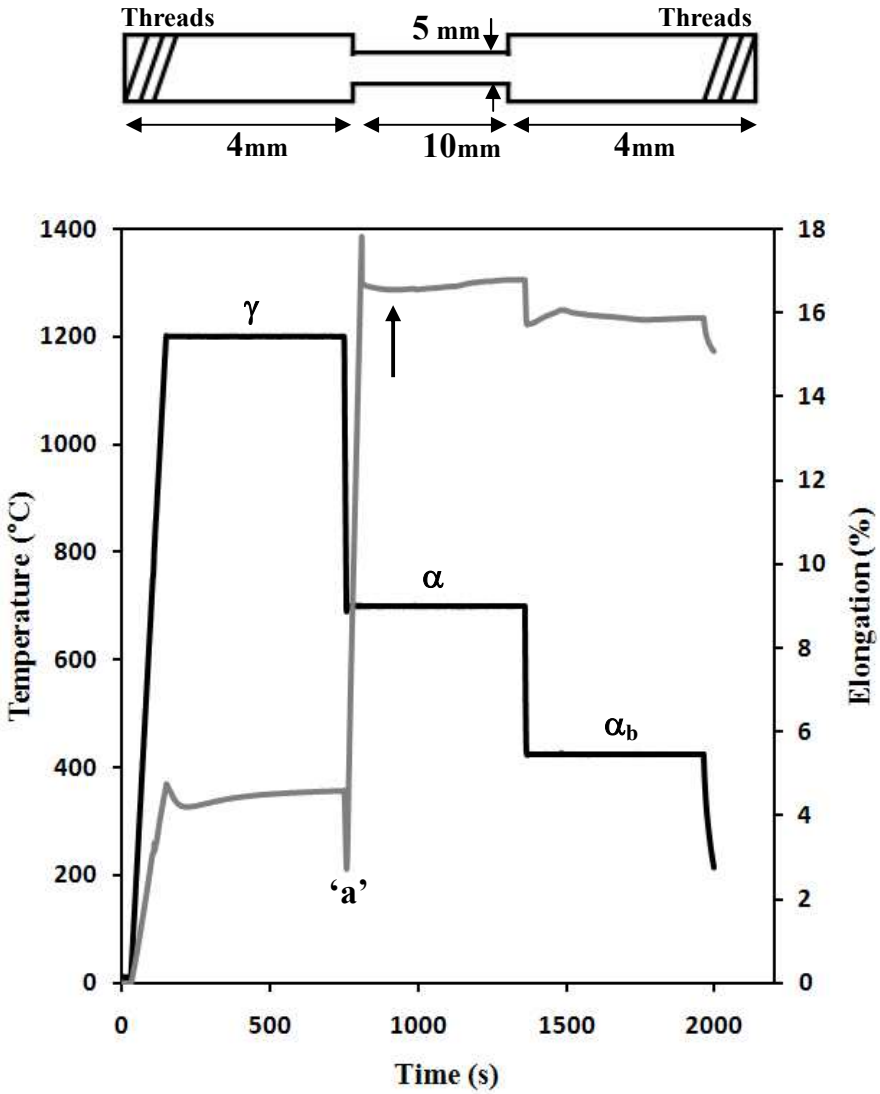


Figure 5.1 The thermo-mechanical procedure for the dilatometric experiments. The deformation step was in some cases omitted for comparison purposes. Austenite, allotriomorphic ferrite and bainitic ferrite are represented by the symbols γ, α and $\alpha_b$, respectively. The point **'a'** marks the beginning of the deformation. The arrow marks the point where allotriomorphic ferrite begins to form during isothermal holding at 740 ℃.

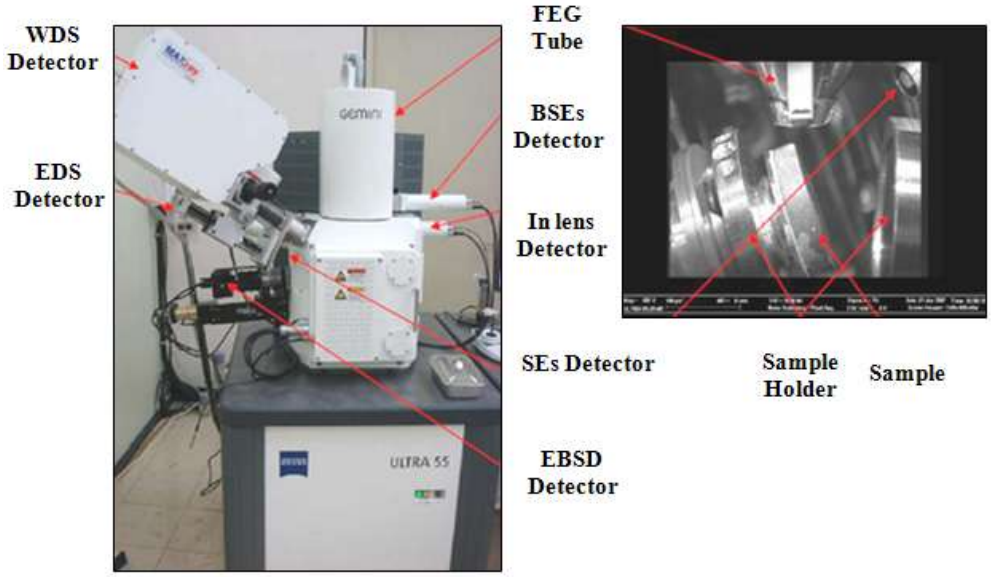


Figure 5.2 Electron back scattered diffraction (EBSD) on a ZEISS SUPRA™ scanning electron microscope with Field Emission Gun used in the experiments. Aperture and working distance was set to 120$\mu$m and 20mm respectively. Acceleration voltage was 20kV.

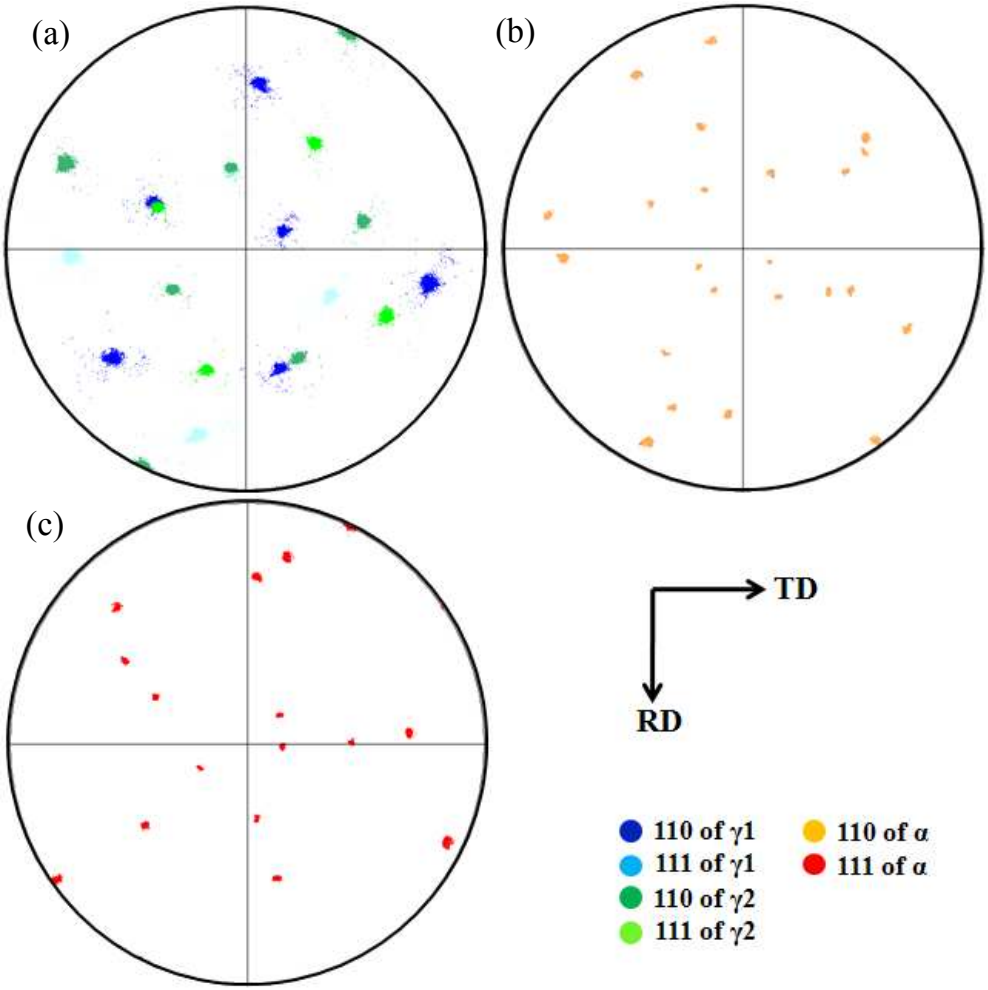


Figure 5.3 (a) {110} and {111} poles from grains of undeformed austenite of the sample illustrated in Figure 5.4. (b) Corresponding {110} pole figure and (c) {111} pole figure of allotriomorphic ferrite that grows from deformed austenite.

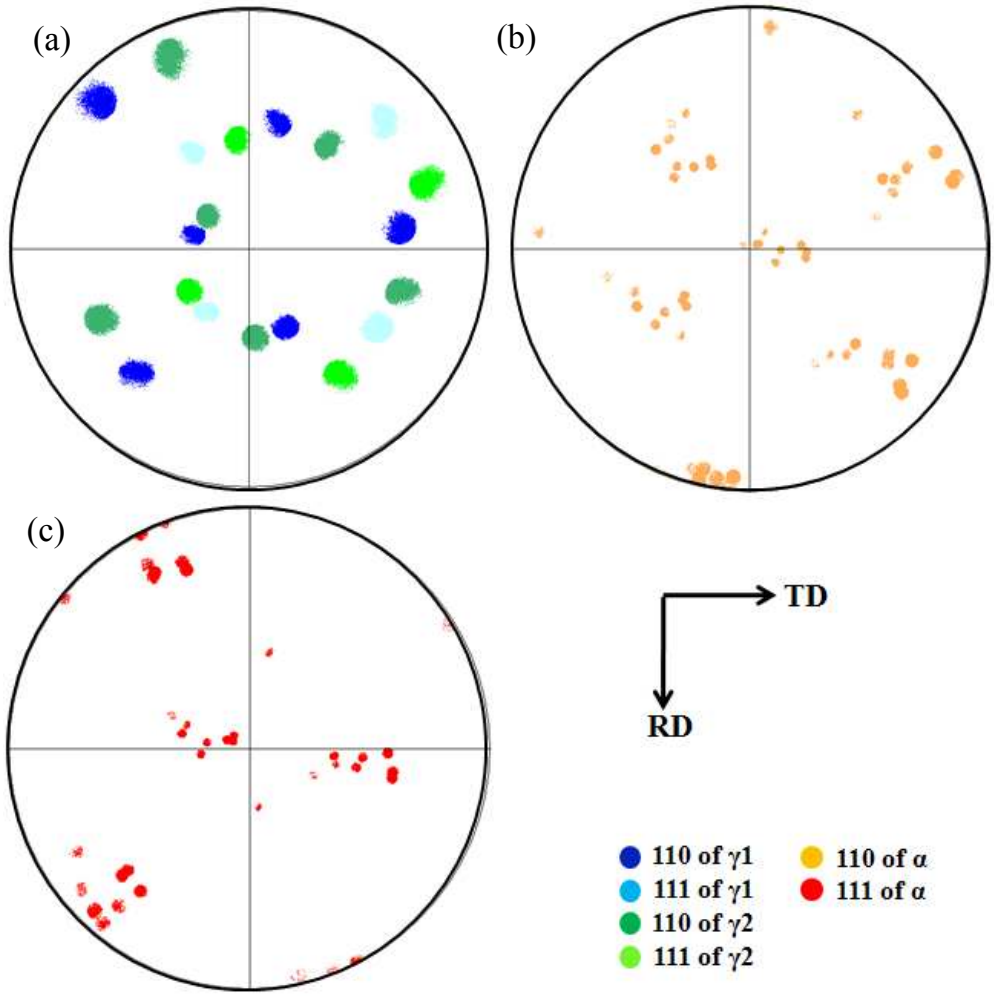


Figure 5.4 (a) {110} and {111} poles from grains of deformed austenite of the sample illustrated in Figure 5.4. (b) Corresponding {110} pole figure and (c) {111} pole figure of allotriomorphic ferrite that grows from deformed austenite. The direction of applied strain is vertical.

of the cubic lattice. Suppose that the $i^{th}$ variant of ferrite forms at a grain boundary between two austenite crystals $\gamma_1$ and $\gamma_2$, the given ($\gamma_1$ $J^i_{KS}$ $\alpha$), it follows that

$$(\gamma_2 \quad J \quad \alpha) = (\gamma_2 \quad J \quad \gamma_1)\left(\gamma_1 \quad J^i_{KS} \quad \alpha\right) \tag{5.2}$$

where ($\gamma_1$ $J^i_{KS}$ $\alpha$) is the inverse of ($\alpha$ $J^i_{KS}$ $\gamma_1$) and ($\gamma_2$ J $\gamma_1$) describes how the two crystals of austenite are related. In order to determine whether the ferrite simultaneously exhibits a low-energy orientation with both of the austenite grains, it is necessary to determine how close ($\gamma_2$ J $\alpha$) is to a Kurdjumov–Sachs orientation. This can be done by defining a 'difference' matrix as follows:

$$(\gamma \quad \Delta J \quad \gamma) = (\gamma \quad J \quad \alpha)\left(\alpha \quad J^i_{KS} \quad \gamma\right) \tag{5.3}$$

This difference matrix can also be expressed as a right-handed rotation h about a specific axis of rotation. Because of the symmetry of the cubic system, there are 24 equivalent axis–angle pairs and the one corresponding to the smallest rotation is chosen here to represent the deviation from an exact Kurdjumov–Sachs orientation.

## 5.4 Classical type of dual orientation

Figure 5.5 shows four ferrite grains at an austenite grain boundary. It is clear from the orientation image that each ferrite grain is related only to one of the adjacent austenite grains, and the data presented in Table 5.1 confirm this. The last column indicates the $\sum$ coincidence site lattice (CSL) number for the austenite grain boundary at which the ferrite nucleates; an absence of a number indicates that the $\gamma/\gamma$ orientation does not coincide with a CSL orientation. It is noticeable that the

ferrite grains grow as layers along the austenite grain boundaries. One reason for this is a small nucleation rate, which then allows the few grains that form to develop along the austenite grain surfaces and these further limits the number density of ferrite grains. Since the focus of the present work is to look at crystallography, it would be useful to increase the nucleation rate.

Not surprisingly, Figure 5.7 shows that the overall rate at which allotriomorphic ferrite forms in a sample, which is deformed prior to transformation, is greater than one in which the ferrite grows from undeformed austenite. It is well known that deformation of the austenite increases the nucleation rate at the austenite grain boundaries. Figure 5.6 shows that this is indeed achieved when the transformation occurs from deformed austenite, with a relatively large number density of ferrite grains at the austenite grain boundaries.

The grains have colours in the orientation image, which are similar to those of the bainite on either side of the grain boundary. Table 5.2 shows that deviation from the exact Kurdjumov–Sachs orientation is significant but small, an indication that each ferrite grain attempts to lattice match with both of the adjacent austenite crystals. Further studies were focused on deformed samples. It is not possible to comment on the generality of this result without extensive observations, but the possibility of such matching must increase when the orientation difference between the adjacent austenite grains is small [18]. It has been pointed out that [30] the small chance of finding a dual orientation relation may be related to the fact allotriomorphic ferrite can grow rapidly into surrounding grains with which it is randomly oriented.

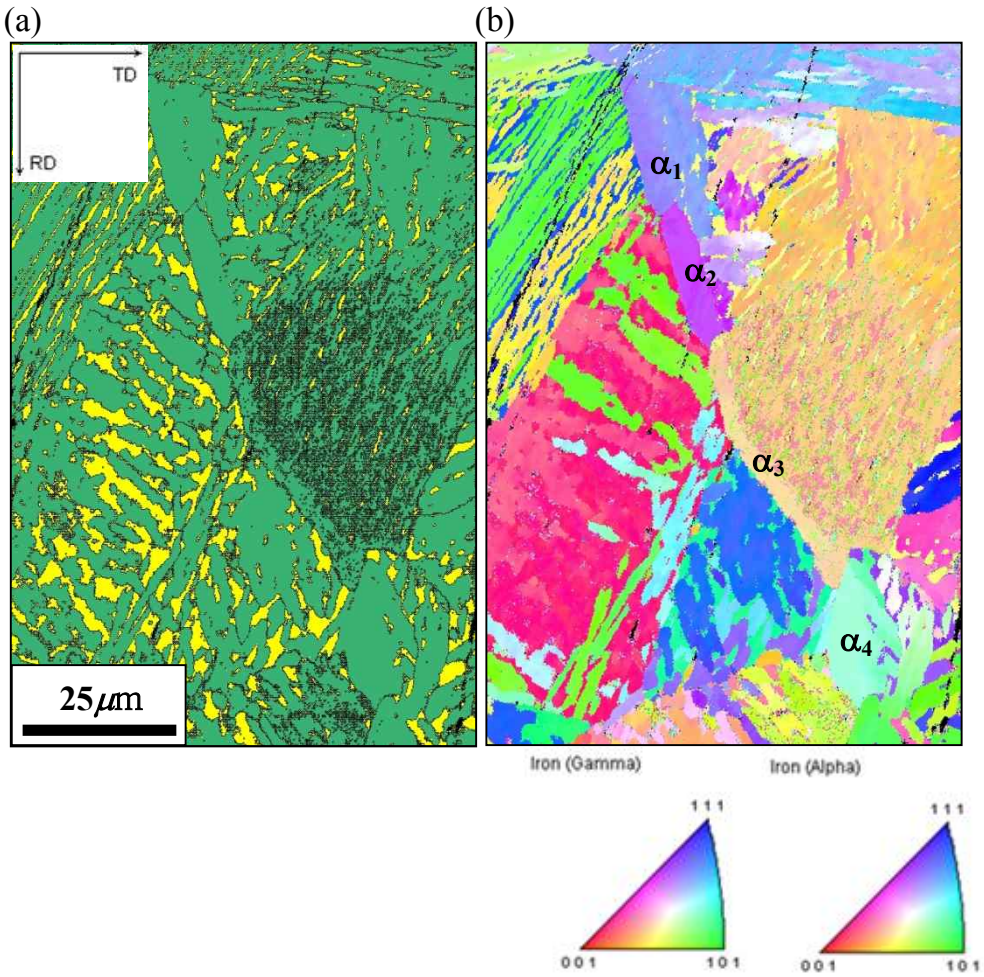


Figure 5.5 Transformation in undeformed sample. (a) Phase map with yellow corresponding to austenite and green to allotriomorphic or bainitic ferrite and (b) orientation map of scanned area.

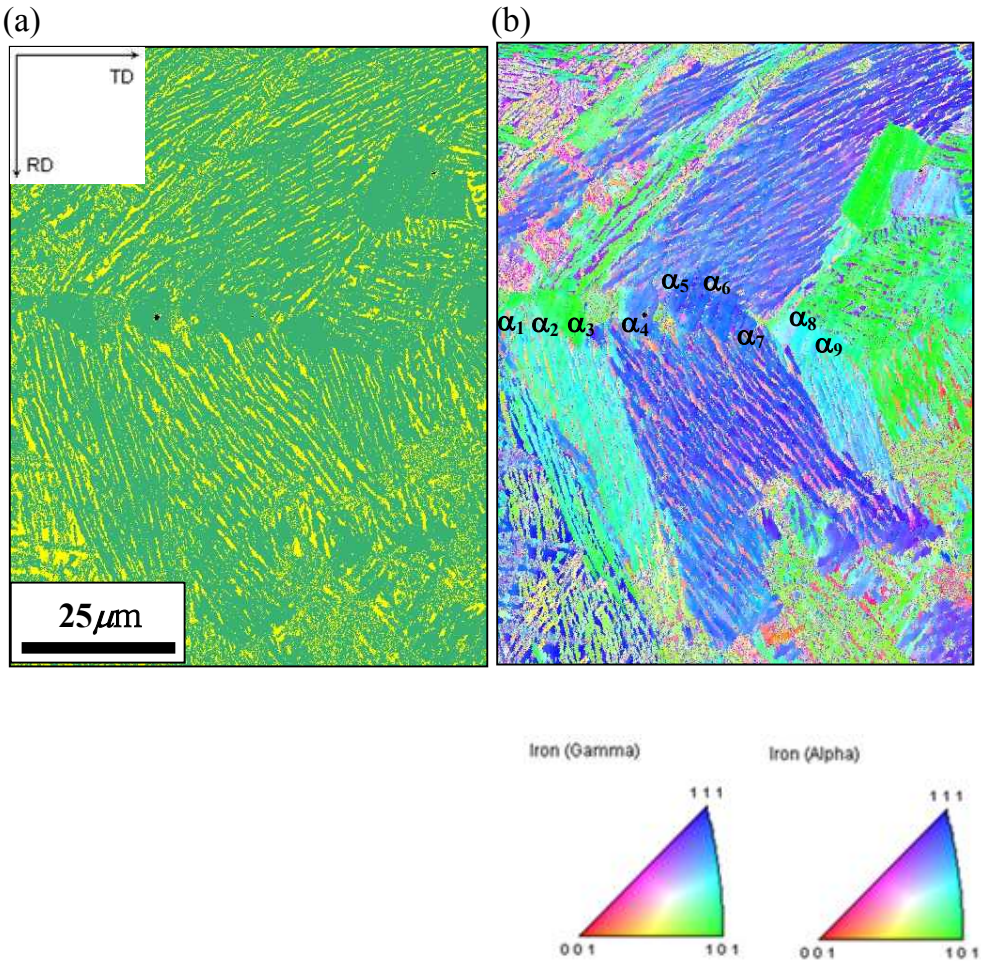


Figure 5.6 Transformation in undeformed sample. (a) Phase map with yellow corresponding to austenite and green to allotriomorphic or bainitic ferrite and (b) orientation map of scanned area

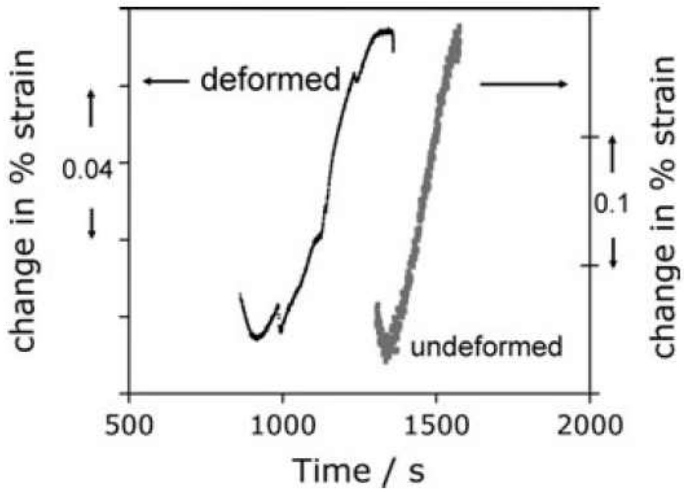


Figure 5.7 Comparison of the rate at which allotriomorphic ferrite forms during isothermal transformation in deformed and undeformed austenite

Table 5.1 Deviation from the exact Kurdjumov-Sachs orientation for the ferrite grains illustrated in Figure 5.5

| Ferrite grains | Deviation axis - angle pairs for ($\gamma$ $\Delta$J $\gamma$) | | | | Σ |
|---|---|---|---|---|---|
| | Adjacent γ 1 | | Adjacent γ 2 | | |
| $\alpha_1$ | [-0.567, -0.659, -0.493] | 1.6° | [0.984, 0.085, -0.153] | 22.0° | - |
| $\alpha_2$ | [-0.696, 0.717, 0.014] | 4.5° | [-0.034, -0.996, -0.074] | 17.0° | |
| $\alpha_3$ | [0.087, -0.289, -0.953] | 1.3° | [-0.743, 0.042, 0.667] | 20.4° | |
| $\alpha_4$ | [0.578, 0.531, 0.618] | 30.4° | [-0.590, 0.734, 0.331] | 2.3° | |
| $\gamma_1$ | | | [-0.530, 0.013, -0.848] | 37.2 | - |
| $\gamma_2$ | [-0.530, 0.013, -0.848] | 37.2 | - | | |

Table 5.2 Deviation from the exact Kurdjumov-Sachs orientation for the ferrite grains illustrated in Figure 5.6

| Ferrite grains | Deviation axis - angle pairs for ($\gamma$ $\Delta$J $\gamma$) | | | | Σ |
|---|---|---|---|---|---|
| | Adjacent γ 1 | | Adjacent γ 2 | | |
| α1 | [0.903, -0.221, -0.365] | 4.1° | [0.956, -0.289, -0.011] | 13.8° | - |
| α2 | [0.560, 0.781, -0.272] | 10.1° | [-0.699, -0.567, 0.434] | 5.2° | |
| α3 | [-0.159, 0.985, 0.061] | 14.6° | [0.016, 0.972, -0.230] | 4.4° | |
| α4 | [-0.527, 0.821, -0.216] | 14.4° | [-0.847, 0.289, -0.444] | 2.9° | |
| α5 | [0.6817, -0.726, 0.086] | 18.9° | [-0.406, -0.898, -0.165] | 4.8° | |
| α6 | [0.863, 0.503, 0.042] | 12.9° | [0.292, 0.934, 0.202] | 4.4° | |
| α7 | [0.010, -0.744, -0.667] | 9.9° | [0.577, -0.096, 0.810] | 10.1° | |
| α8 | [-0.369, -0.613, -0.697] | 4.3° | [-0.872, 0.302, -0.383] | 10.4° | |
| α9 | [0.716, -0.671, 0.189] | 3.8° | [0.958, 0.220, -0.178] | 9.6° | |
| γ 1 | - | | [-0.444, 0.893, -0.079] | 22.4 | - |
| γ 2 | [-0.444, 0.893, -0.079] | 22.4 | - | | |

However, the greatly increased nucleation rate in deformed austenite confines the ferrite grains by impingement so that the chance of observing dual orientations is greatly increased.

## 5.5 Dual orientation at CSL boundaries

Figure 5.8 shows a large number of equiaxed ferrite grains, the crystallographic data for which are listed in Table 5.3, classified into three groups. The interesting feature of the data is that two of the austenite grain boundaries correspond closely to the $\sum = 3$ and $\sum = 11$ $\gamma/\gamma$ orientation. The former of course corresponds to the highest number density of coincidence points and hence a relatively low interfacial energy per unit area; it is not surprising therefore that there is an absence of ferrite grains at the boundary. The first two groups listed in Table 5.3 are grains that have nucleated at the $\sum = 11$ boundary and it is particularly noticeable that most of these ferrite crystals are able to match fairly well to both of the austenite grains related across the $\sum = 11$ grain boundary. In contrast, the ferrite nucleated at the general boundary between $\gamma_3/\gamma_6$ do not fit well with the dual orientation concept. These observations led us to believe that nucleation at austenite grains related by low $\sum$ values would be worth investigating theoretically to see whether such $\gamma/\gamma$ orientations favour the formation of dual orientation ferrite grains.

## 5.6 Calculation of dual orientation at some CSL boundaries

Assuming a specific $\gamma_1/\gamma_2$ orientation relationship defined by an exact $\sum$ value,

and ferrite forming with an exact Kurdjumov–Sachs orientation with $\gamma_1$, it was possible to assess for all 24 variants of ferrite possible in $\gamma_1$ to calculate how far the ferrite grain deviates from the Kurdjumov–Sachs orientation with $\gamma_2$. The results are illustrated in Figure 5.8 and show clearly that the propensity for developing dual orientations is large for $\sum = 11$; even when $\Delta_{max}$ which means the maximum deviation permitted from the exact Kurdjumov-Sachs orientation relationship is set to a low value.

When larger values of $\Delta_{max}$ are permitted in the definition of dual orientations, other $\sum$ boundaries show significant increases in the ability for ferrite to simultaneously match both of the adjacent austenite grains (Table 5.4). Notice that $\sum = 3$ features as the most favoured for the development of dual orientations, but the $\gamma/\gamma$ interfacial energy corresponding to this CSL is very low and hence such boundaries are relatively ineffective as heterogeneous nucleation sites for ferrite. What this also emphasizes is that any model for the prediction of transformation texture, which is based on the selection of variants, which lead to dual orientations, must at the same time take into account the interfacial energy per unit area of the austenite grain boundaries available in the microstructure.

Finally, it is worth noting that there is considerable activity in a related field, that of *grain boundary engineering*, where efforts are made to introduce a large density of coincidence site boundaries in order to control the properties of steels [80, 81]. If such steels transform to allotriomorphic ferrite, then variant selection should play an exaggerated role in the development of crystallographic texture. Finally, it is worth

pointing out that even when the ferrite has a low-energy orientation relationship with austenite, and it displays the same color in an orientation image as the bainite, it remains to be proven that these two phases have the same crystallography. This is because an irrational orientation relation is *necessary* in the case of a displacive transformation such as bainite, but not necessarily so for diffusional transformations such as allotriomorphic ferrite.

## 5.7 Conclusions

In earlier work in Chapter 4, it was demonstrated that the probability of ferrite nucleating with good lattice matching with more than one austenite grain with which it is in contact (dual orientations), is small. This conclusion was not changed significantly by introducing common macroscopically defined crystallographic textures into the austenite (for example, Goss, Cube etc.). However, the macroscopic texture descriptions of the kind considered do not uniquely reflect the orientations between adjacent austenite grains as described, for example, by the coincidence site lattice. It is found in the present work that certain coincidence site lattices favour the development dual orientations. This has been verified both experimentally and theoretically and may explain early work where the probability of observing dual orientations was noted to be significant. It also appears that the chance of observing dual orientations increases when transformation occurs from deformed austenite since the associated high rate of nucleation prevents the spread of allotriomorphic ferrite. It would be useful in future work to build up a three-

dimensional picture of the crystallography, one which includes the indices of the grain boundary plane. This could be done using serial sectioning based on focused ion beam machining.

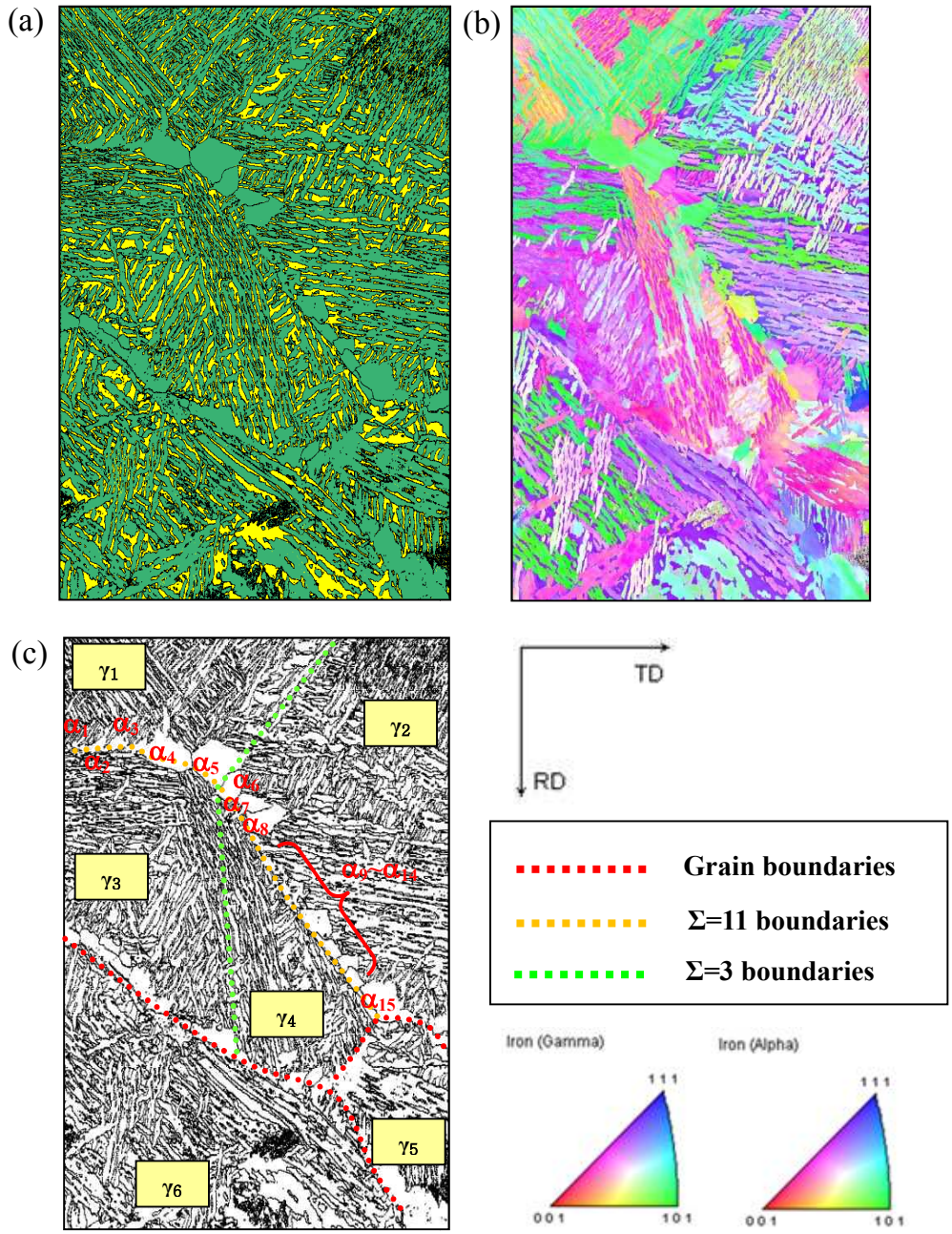


Figure 5.8 Transformation in sample of same condition with Figure 5.6. (a) phase map with yellow corresponding to austenite and green to allotriomorphic or bainitic ferrite, and (b) orientation map, (c) image quality map of scanned area.

Table 5.3 Deviation from the exact Kurdjumov-Sachs orientation for the ferrite grains illustrated in Figure 5.8. Notice that the axis-angle pairs relating $\gamma_1$/ $\gamma_2$ and $\gamma_2$/ $\gamma_4$ correspond quite closely to that expected from $\sum = 11$ at a 50.5° about <011>

| Group 1 | Deviation axis - angle pairs for ($\gamma$ $\Delta$J $\gamma$) | | | | Σ |
|---|---|---|---|---|---|
| | With respect to $\gamma_1$ | | With respect to $\gamma_3$ | | |
| α1 | [0.903, -0.221, -0.365] | 4.1° | [0.206, -0.866, 0.454] | 3.1° | |
| α2 | [0.843, 0.138, -0.519] | 4.8° | [0.618, -0.749, 0.234] | 2.5° | |
| α3 | [-0.048, -0.989, 0.133] | 3.9° | [-0.851, 0.497, 0.165] | 4.6° | |
| α4 | [0.028, -0.713, -0.700] | 4.9° | [-0.047, -0.697, -0.714] | 6.8° | |
| α5 | [0.742, -0.334, -0.580] | 1.9° | [-0.285, 0.925, -0.249] | 4.2° | |
| γ 1 | - | | [0.004, 0.745, 0.667] | 47.4° | 11 |
| γ 3 | [0.004, 0.745, 0.667] | 47.4° | - | | 11 |

| Group 2 | Deviation axis - angle pairs for ($\gamma$ $\Delta$J $\gamma$) | | | | Σ |
|---|---|---|---|---|---|
| | With respect to $\gamma_2$ | | With respect to $\gamma_4$ | | |
| α6 | [0.643, 0.752, -0.154] | 11.2° | [0.507, -0.856, 0.097] | 30.9° | |
| α7 | [0.410, -0.911, -0.001] | 7.8° | [-0.442, 0.680, 0.583] | 3.4° | |
| α8 | [-0.112, -0.278, -0.953] | 4.6° | [0.319, 0.926, -0.197] | 5.1° | |
| α9 | [0.748, 0.662, 0.032] | 5.4° | [0.286, 0.306, -0.907] | 2.9° | |
| α10 | [-0.450, 0.438, -0.777] | 5.3 | [-0.259, 0.275, -0.925] | 17.6° | |
| α11 | [0.917, 0.094, 0.386] | 27.3°° | [-0.827, -0.365, 0.426] | 5.4° | |
| α12 | [-0.908, 0.285, 0.304] | 5.5° | [-0.739, 0.656, -0.147] | 20.3° | |
| α13 | [-0.300, -0.679, -0.669] | 7.3° | [0.935, -0.343, 0.084] | 9.6° | |
| α14 | [-0.992, 0.095, 0.073] | 5.2° | [-0.752, 0.425, 0.501] | 19.4° | |
| α15 | [0.712, -0.564, 0.416] | 8.5° | [0.585, 0.511, 0.629] | 10.3° | |
| γ 2 | - | | [-0.059, 0.699, -0.713] | 50.3° | 11 |
| γ 4 | [-0.059, 0.699, -0.713] | 50.3° | - | | 11 |

| Group 3 | Deviation axis - angle pairs for ($\gamma$ $\Delta$J $\gamma$) | | | | Σ |
|---|---|---|---|---|---|
| | With respect to $\gamma_3$ | | With respect to $\gamma_6$ | | |
| α16 | [0.968, 0.205, 0.139] | 1.6° | [0.824, -0.018, 0.565] | 24.1° | - |
| α17 | [0.097, -0.928, 0.359] | 12.3° | [-0.292, -0.715, -0.635] | 5.6° | |
| α18 | [-0.947, -0.302, -0.101] | 25.5° | [-0.850, 0.473, -0.229] | 3.4° | |
| α19 | [0.988, 0.053, -0.138] | 22.5° | [-0.634, -0.659, -0.404] | 1.8° | |
| α20 | [0.167, 0.540, -0.824] | 5.2° | [-0.107, -0.986, 0.123] | 12.4° | |
| α21 | [-0.282, 0.835, -0.470] | 3.8° | [0.121, -0.991, 0.041] | 8.0° | |
| α22 | [0.879, -0.240, 0.411] | 2.9° | [-0.698, 0.621, 0.354] | 13.4° | |
| α23 | [0.032, -0.845, -0.532] | 16.3° | [0.476, 0.214, -0.852] | 4.9° | |
| $\gamma$ 3 | - | | [0.809, 0.498, 0312] | 31.2 ° | |
| $\gamma$ 6 | [0.809, 0.498, 0312] | 31.2 ° | - | | |

Table 5.4 Calculated percentage of dual orientation at austenite grains related by the coincidence site lattice orientation indicated. $\Delta_{max}$ represents the maximum deviation permitted from the exact Kurdjumov-Sachs orientation relationship

| $\sum$ | Dual orientation percentage (%) | | | |
|---|---|---|---|---|
| | $\Delta_{max} = 1°$ | $\Delta_{max} = 5°$ | $\Delta_{max} = 10°$ | $\Delta_{max} = 15°$ |
| 3 | 25 | 25 | 50 | 75 |
| 5 | 0 | 0 | 0 | 0 |
| 7 | 0 | 0 | 0 | 0 |
| 9 | 0 | 0 | 16.66 | 20.83 |
| 11 | 8.33 | 25 | 16.66 | 50 |
| 13a | 0 | 0 | 30.33 | 30.33 |
| 13b | 0 | 0 | 0 | 0 |
| 15 | 0 | 0 | 16.66 | 20.83 |
| 17a | 0 | 0 | 30.33 | 30.33 |
| 19a | 0 | 0 | 16.66 | 16.66 |
| 19b | 0 | 12.5 | 25 | 50 |
| 21a | 0 | 25 | 29.16 | 29.16 |

# Chapter 6 Selective Grain Growth Phenomenon and Variant Selection

## 6.1 Introduction

The influence of interfacial and strain energy on the activation energy for nucleation varies with transformation mechanism [40]. For displacive transformations, the product phase always has a coherent or semi-coherent interface with the parent phase but the transformation is accompanied by a large shape deformation, which so that strain energy dominates nucleation. On the other hand, diffusional nucleation and growth at relatively high temperatures, as in allotriomorphic ferrite formation relaxes strains so that interfacial energy dominates the process.

It was confirmed in section 3.4 that variant selection is related to both interfacial and strain energies accompanying the transformation. For displacive transformation, variant selection is dominated by an interaction between shape strain and external stress or strain [4, 5, 9, 45, 48, 82]. Interfacial energy as a function of the crystallographic orientation of parent and product phases seems to control variant selection in the case of reconstructive transformations. However, as it mentioned in section 3.5, the suggestion by Lee and Aaronson [15, 16] based on interfacial energy minimization has been consistent with variant selection only in limited circumstances.

Their interpretation on variant selection based on interfacial energy assumes

intrinsically that the orientations of precipitates are determined at nucleation stage, and does not change during the growth. However, when precipitates evolve at the grain boundaries of the deformed parent phase, their growth can be affected by the difference in stored energy between adjacent parent phase grains as well as the characteristics of interface. It follows that a consideration of the crystallography in terms of growth as well as nucleation may reveal the true mechanism for diffusional transformations.

In this chapter, the effect of transformation from deformed austenite on the selection of variants of ferrite has been investigated. The effect of stored energy differences in influencing these phenomena is revealed.

## 6.2 Experimental procedures

### 6.2.1 Heat treatment

The chemical composition of alloy used this experiments is Fe-0.595C-0.98Si-1.10Mn-1.50Al wt. % for heat treatment on a deformation dilatometer. Cylindrical samples 5 mm in diameter and 10 mm in length were heated at 9 ℃/s to 1200℃ and held for 10 min., followed by cooling to the 740℃ with -70 ℃/s to hold for 15 min. to form allotriomorphic ferrite. If necessary, approximately 30 % compressive strain was applied after cooling to 740℃ before ferrite formation starts. The sample was then quenched to 425℃ and austempered for 10 min. followed by cooling to ambient temperature. The fraction of retained austenite was about 20% due to the

suppression of cementite by Si and Al. The contents enable the direct analysis of orientation relationship between austenite and ferrite. Figure 6.1 (a) shows the heat-treatment path and corresponding dilatation strains.

### 6.2.2 EBSD measurement

Samples were polished using the standard specimen preparation method and etched with 2 vol. % nital solution for analysis using optical microscope. Specific areas for EBSD mapping was marked with micro-indentation. Then the surface of samples were polished again with colloidal silica for 3 min. Crystallographic orientations of austenite and ferrite were measured using electron back scattered diffraction (EBSD) on a ZEISS SUPRATM scanning electron microscope. Step size for orientation mapping was 0.05 μm.

### 6.2.3 Evaluation of stored energy in deformed austenite grains

The pattern quality (or image quality) of the orientation map can be a measure of the stored energy because it is associated with the density of defects such as dislocations [83] , but it is also affected by the sample preparation method or by lattice distortion during bainitic and martensitic transformation. Another method to evaluate the stored energy is utilizing the average dislocation density from following relationship with maximum flow stress [84]:

$$\rho = \left[\frac{\sigma_{m\,ax}}{k_M M \mu_T b}\right] \qquad (6.1)$$

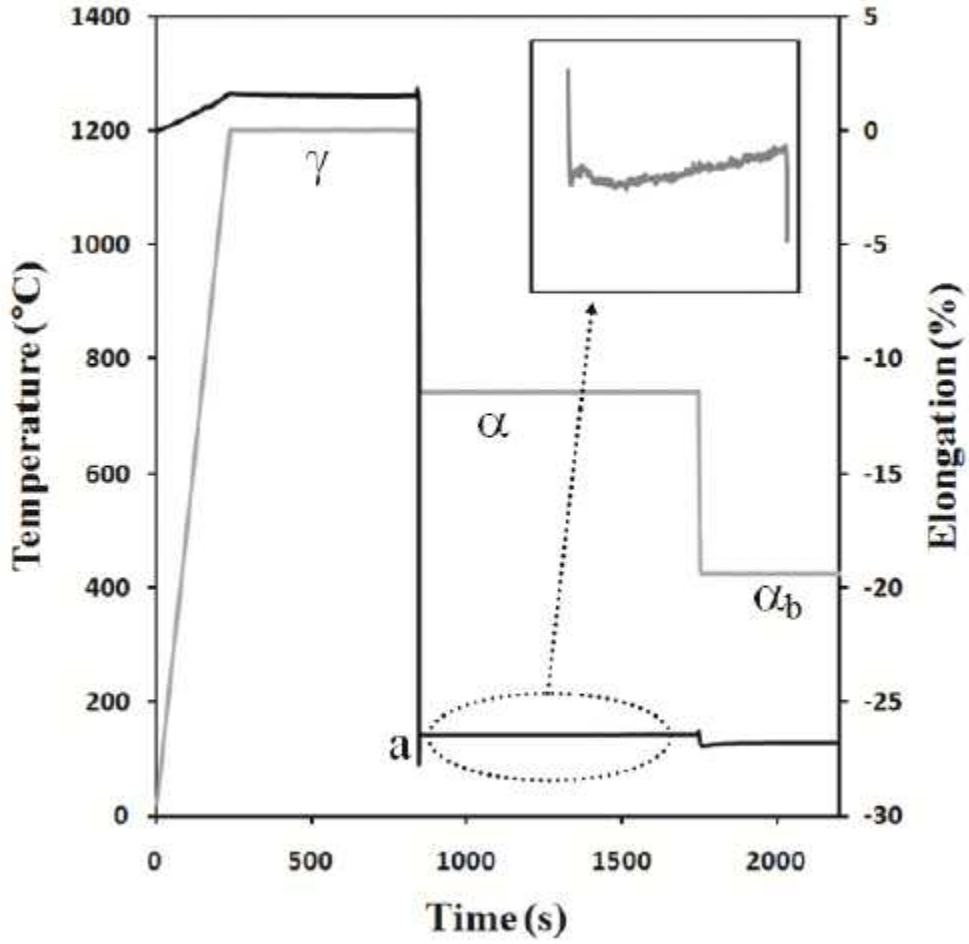


Figure 6.1 (a) The thermo-mechanical procedure for the dilatometric experiments The deformation step was in some cases omitted for comparison purposes. Austenite, allotriomorphic ferrite and bainitic ferrite are represented by the symbols γ and α respectively. The point '**a'** marks the point where allotriomorphic ferrite begins to form during isothermal holding at 740℃.

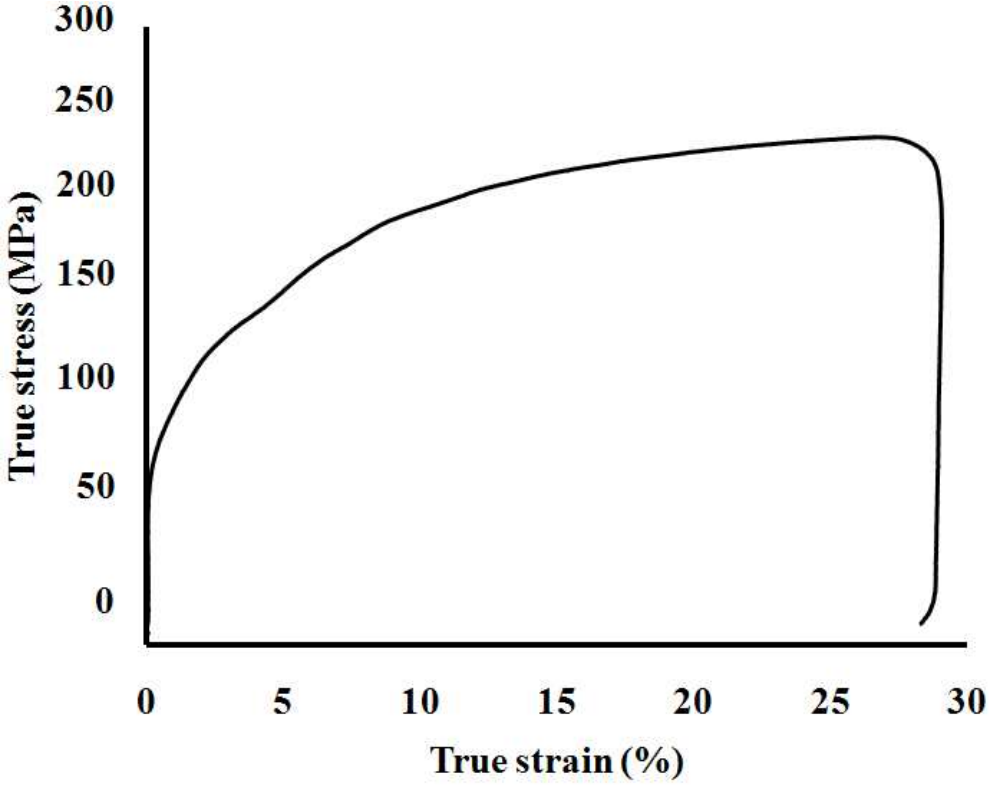


Figure 6.1 (b) The flow curve for 30% compressive deformation step corresponding to (a) at 740℃. The maximum flow stress was evaluated as about 220MPa.

where $k_M$ is a constant to be 0.15, $M$ is taken as 3.11 for mean Taylor factor. The maximum flow stress $\sigma_{max}$ was evaluated as 220MPa during 30% compressive deformation at 740℃ (Figure 6.1 (b)). $\mu_T$ is a temperature dependent shear modulus:

$$\mu_T = \mu_0 \left[1 + \left(\frac{T - 300}{T_M} \cdot \frac{T_M}{\mu_0} \cdot \frac{d\mu_T}{dT}\right)\right]^2 \quad (6.2)$$

In austenite, $T_M$=1810 K, $\left(\frac{T_M}{\mu_0} \cdot \frac{d\mu_T}{dT}\right)$= -0.91 and $\mu_0$=8.1×10$^{10}$ Jm$^{-3}$. Since the energy per unit length of dislocation line is approximately equal to $0.5\mu_0 b^2$, the stored energy per unit volume due to the new dislocations introduced by the plastic deformation can be expressed as:

$$W = 0.5\mu_0 b^2(\rho - \rho_0) \quad (6.3)$$

where $\rho_0$ is about 10$^{12}$ m$^{-2}$ for fully recrystallized austenite and $b$ is 2.5×10$^{10}$ m for the magnitude of Burgers vector. The Taylor factor is usually mentioned as the slip resistance or the sum of shears required attaining a given deformation. So, a higher Taylor factor indicates a greater plasticity and hence dislocation density inside the grain [85-87]. With these assumptions the stored energy is proportional to the Taylor factor and can be evaluated as follows:

$$\Delta G_{def} = W \frac{M_j(g_j)}{\overline{M}} \quad (6.4)$$

where $M_j$ is Taylor factor for grain $j$ having grain orientation $g_j$ and $\overline{M}$ is the mean Taylor factor value of the aggregate.

## 6.3 Orientation of allotriomorphic ferrite to adjacent austenite grains

### 6.3.1 Undeformed sample

Figure 6.2 shows phase and orientation maps of ferrite formed at a grain boundary. Without prior deformation of austenite, the allotriomorphic ferrite has a layer-like morphology when the driving force for nucleation is small, as shown in Figure 6.2. The orientation relationship between austenite and ferrite is summarized in Table 1. It gives a representative behavior that ferrite has an orientation relationship with one of adjacent austenite grains. Figure 6.3 (a) shows the trace of the grain boundary plane and $\{111\}_\gamma$, $\{110\}_\gamma$ poles together with the $\{111\}_\gamma$ plane which is most parallel to the grain boundary, marked as a circle. According to Lee et al., as the close-packed plane in the austenite becomes parallel to the grain boundary plane, the activation energy for nucleation of ferrite is reduced. Table 6.1 indicates that all ferrite grains have an orientation relationship with the $\gamma_2$ grain which has $\{111\}$ plane closest to the grain boundary plane, which agrees well with Lee et al [51-54]. This kind selection of variant is known to be sensitive to the curvature of boundary plane, but above results confirm that the orientation relationship between ferrite and austenite is dominated by orientation of grain boundary plane and thus the interfacial energy between ferrite and austenite.

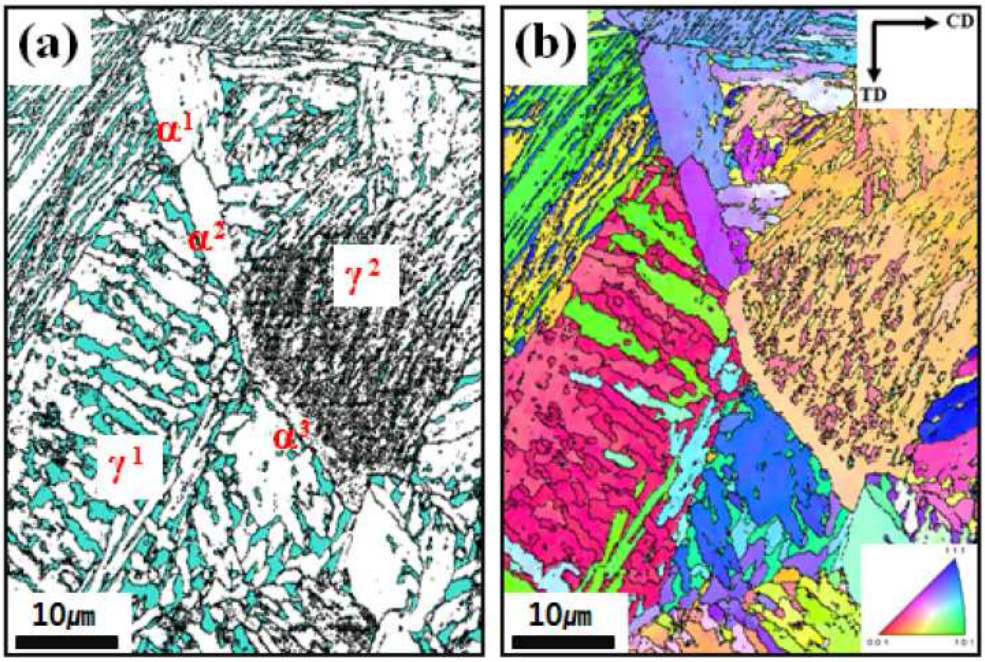


Figure 6.2 Transformation in un-deformed sample. (a) phase map with blue corresponding to the austenite and white to allotriomorphic ferrite or bainitic ferrite, and (b) orientation map.

Table 6.1 Deviation from the exact Kurdjumov-Sachs orientation for the ferrite grains illustrated in Figure 6.2

| Grain | Deviation axis-angle from KS relationship | | | | Σ |
|---|---|---|---|---|---|
| | with respect to r1 | | with respect to r2 | | |
| $\alpha^1$ | [0.98 0.09 -0.15] | 22.0° | [-0.57 -0.66 -0.49] | 1.6° | |
| $\alpha^2$ | [-0.03 -0.99 -0.07] | 17.0° | [-0.70 0.72 0.02] | 4.5° | |
| $\alpha^3$ | [-0.74 0.04 0.67] | 20.4° | [0.09 -0.29 -0.95] | 1.3° | |
| $\gamma^1$ | [-0.530 0.013 -0.848] | 37.2° | - | | - |
| $\gamma^2$ | - | | [-0.530 0.013 -0.848] | 37.2° | - |

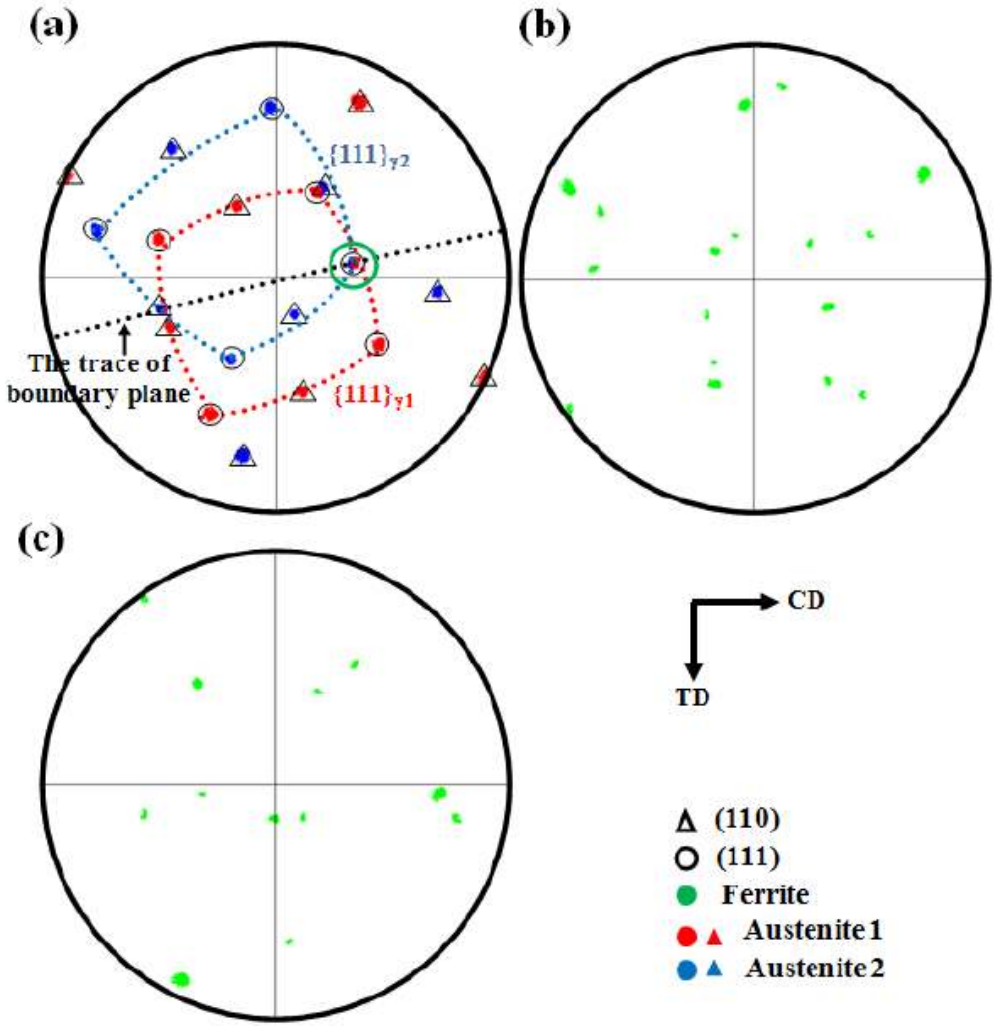


Figure 6.3 (a) {110} and {111} pole figure from two adjacent austenite grains of un-deformed sample illustrated in Figure 6.2. (b) {110} pole figure and (c) {111} pole figure from ferrite nucleated at boundaries. The trace of grain boundary plane indicates the locus of grain boundary plane normal.

### 6.3.2 Deformed sample: nucleation at high energy boundaries

Figure 6.4 represents EBSD mapping around ferrite grains nucleated at a grain boundary in deformed austenite. The stored energy in austenite is evaluated with Equation 6.4. Both austenite grains in Figure 6.4 has similar stored energy of 20 $Jmol^{-1}$ and Figure 6.5 (a) indicates that the {111} plane of $\gamma_1$ grain is almost parallel to the grain boundary plane. In this case, all ferrite grains in grain boundary have KS orientation relationship with $\gamma_1$ grain as shown in Table 6.2. This confirms that the crystallographic variant is controlled by the interfacial energy. Another EBSD mapping in the vicinity of ferrite grains is given in Figure 6.6. The stored energy of deformed austenite grain is evaluated to be 27 $Jmol^{-1}$ and 19 $Jmol^{-1}$ for $\gamma_1$ and $\gamma_2$ grains, respectively. From the grain boundary plane and {111} plane of adjacent austenite grain in Figure 6.7 (a), it is presumed that ferrite prefer to have an orientation relationship with $\gamma_1$ grain which has closest parallel {111} plane to the grain boundary plane. But surprisingly, 13 of 15 ferrite grains have an orientation relationship with $\gamma_2$ (Table 6.3). This contradicts what is expected from the minimization of interfacial energy, which would favour low-energy orientation relationship with $\gamma_1$.

From the analysis of orientation relationship in Figures 6.2 to 6.6, it is notable that the interfacial energy has a substantial effect on the orientation characteristics of ferrite unless there are large differences in stored energy of adjacent austenite grains. Given much a difference, it may be favorable for ferrite to grow in the austenite grain with higher stored energy if interface characteristics at both sides are

equivalent. Generally, ferrite in grain boundary has a semi-coherent interface with one of adjacent austenite grain representing the orientation relationship and incoherent interface with the other austenite grain.

The movement of incoherent interface is faster than semi-coherent one. As shown in Figure 6.8, let us assume two ferrite grains ($\alpha_m$ and $\alpha_n$) growing into austenite grain ($\gamma_m$ and $\gamma_m$). Since $\alpha_m$ and $\alpha_n$ has incoherent interface with $\gamma_m$ and $\gamma_n$, respectively, faster growth direction of $\alpha_m$ is toward $\gamma_m$ and $\alpha_n$ is toward $\gamma_n$. Then, if the difference in stored energy of $\gamma_m$ and $\gamma_n$ is large enough to make the growth of $\alpha_m$ overwhelm that of $\alpha_n$, eventually the $\alpha_m$ will block $\alpha_n$.

In this case, the apparent orientation of ferrite grain will dominated by the difference in relative growth rate rather than the contribution from interfacial energy. For instance, ferrite grain of $\alpha_8$ in Figure 6.6 has an orientation relationship with $\gamma_1$, which will give it advantage in interfacial energy; however, it is surrounded by large ferrite grains due to the sluggish growth. It may be attributed to the slower growth of $\alpha_8$ into the $\gamma_2$ which has lower stored energy than $\gamma_1$ into which other ferrite grains grow. Furthermore, it is noted that 13 of 15 ferrite grains in Figure 6.6 have orientation relationship with $\gamma_2$ austenite, which allow them to grow into the $\gamma_1$ austenite that has higher stored energy and thus possibly provides faster growth kinetics.

Figure 6.9 shows the influence of stored energy difference between adjacent austenite grains on the deviation angle from low energy orientation relationship, which verifies more clearly that local variant selection in deformed sample is

determined by growth control when stored energy is big enough. Since $\gamma_1$ has close packed plane whose (111) plane is closest to the grain boundary plane and grain boundary plane normal pole is far away from (111) variant of $\gamma_2$, ferrite should have low energy orientation relationship with $\gamma_1$. Irrational orientation relationship between ferrite and austenite showed very small deviation angles from ($\alpha$ $J_{LE}$ $\gamma_1$) but huge deviations from ($\alpha$ $J_{LE}$ $\gamma_2$) when stored energy difference were negligible.

However, ferrite shows low energy orientation relationship with $\gamma_1$ whose stored energy is smaller than $\gamma_2$ when energy difference is more than 10 J/mol and it corresponds to experimental results in black and gray colored ellipsoidal regions in the figure 6.9. It was also possible to observe the shifting of these two different tendencies when stored energy differences are 5 J/mol and 7 J/mol therefore, ferrite had low energy orientation relationship with $\gamma_1$ as well as $\gamma_1$. Consequently, we can see from these results that local variant selection during diffusional transformation is determined by *growth selection* when stored energy difference between two adjacent austenite grains is big enough and controlled by *nucleation selection* when there was no stored energy difference (ferrite nucleation in un-deformed austenite) or energy difference is very small.

The Lee et al. model involves '*nucleation selection*', whereas the present work also indicates growth selection whose transformation occurs from heterogeneously deformed austenite.

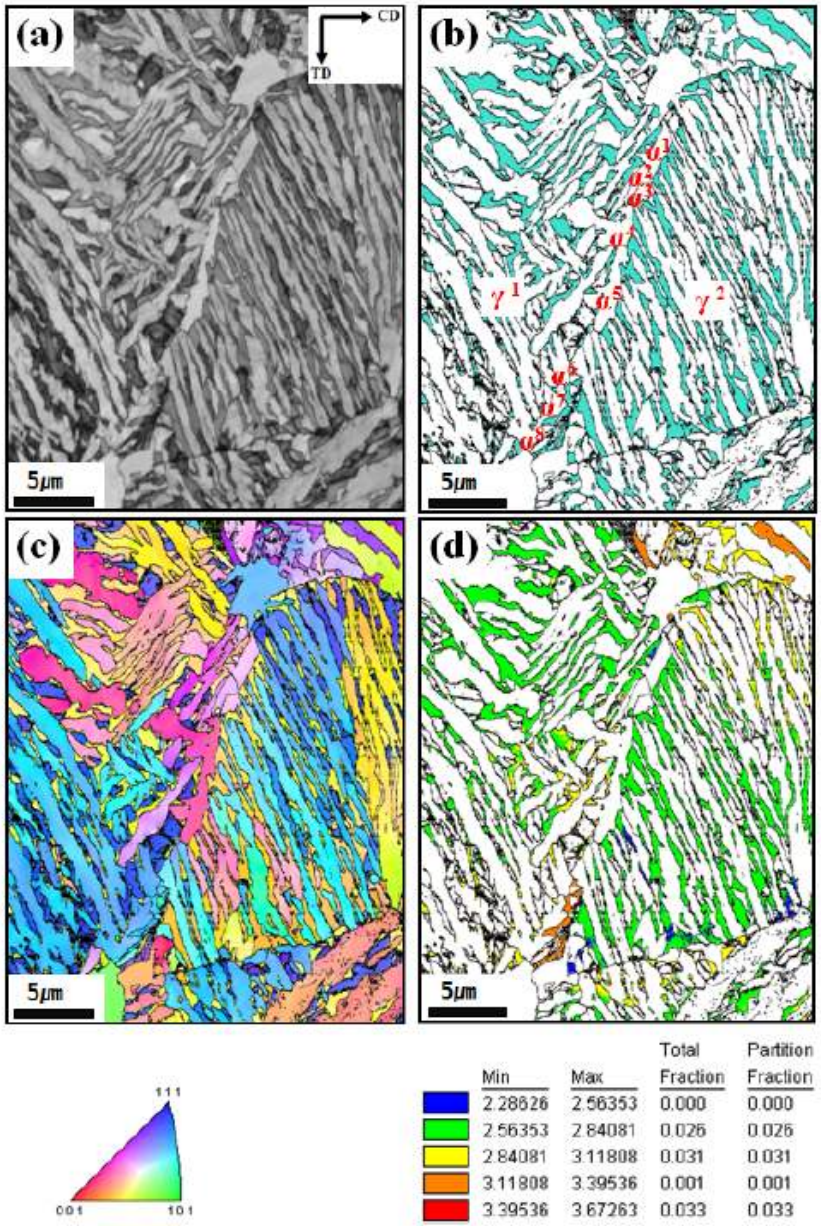


Figure 6.4 Transformation of ferrite nucleated at high angle boundaries when calculated stored energy of 1 and 2 are almost same as 20 $Jmol^{-1}$ (a) image quality map, (b) phase map with blue corresponding to the austenite and white to allotriomorphic ferrite or bainitic ferrite, (c) orientation map and (d) Taylor factor map.

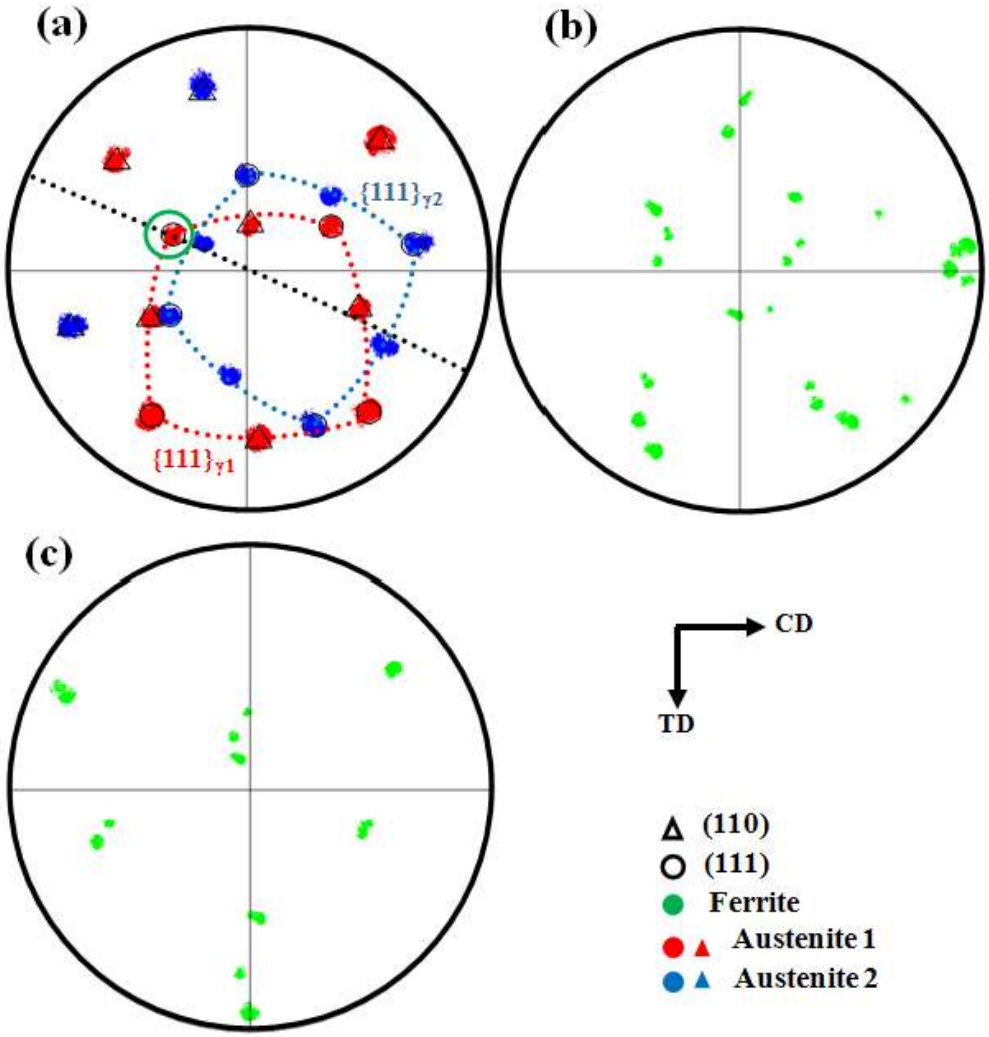


Figure 6.5 (a) {110} and {111} pole figure from two adjacent austenite grains of deformed sample illustrated in Figure 6.4. (b) {110} pole figure and (c) {111} pole figure from ferrite nucleated at boundaries.

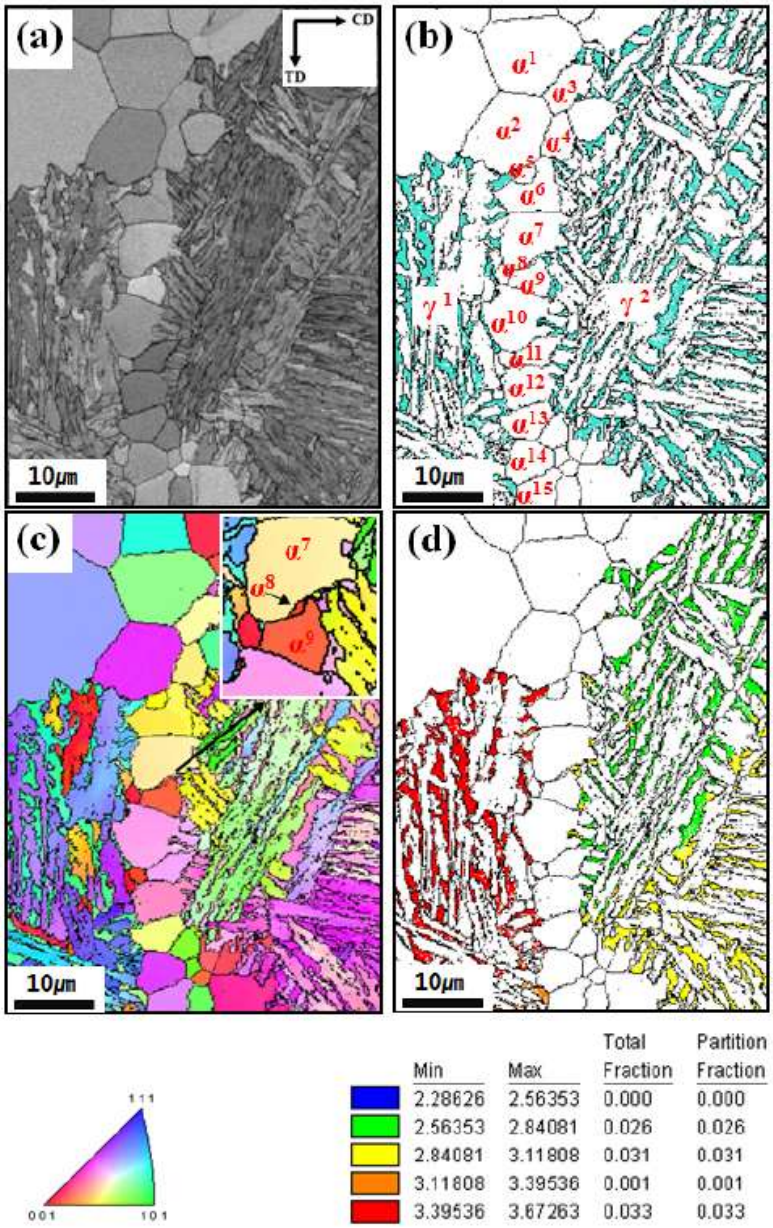


Figure 6.6 Transformation of ferrite nucleated at high angle boundaries when calculated stored energy of 1 and 2 are 27 $\mathrm{Jmol^{-1}}$ and 19 $\mathrm{Jmol^{-1}}$ respectively. (a) image quality map, (b) phase map with blue corresponding to the austenite and white to allotriomorphic ferrite or bainitic ferrite, (c) orientation map and (d) Taylor factor map.

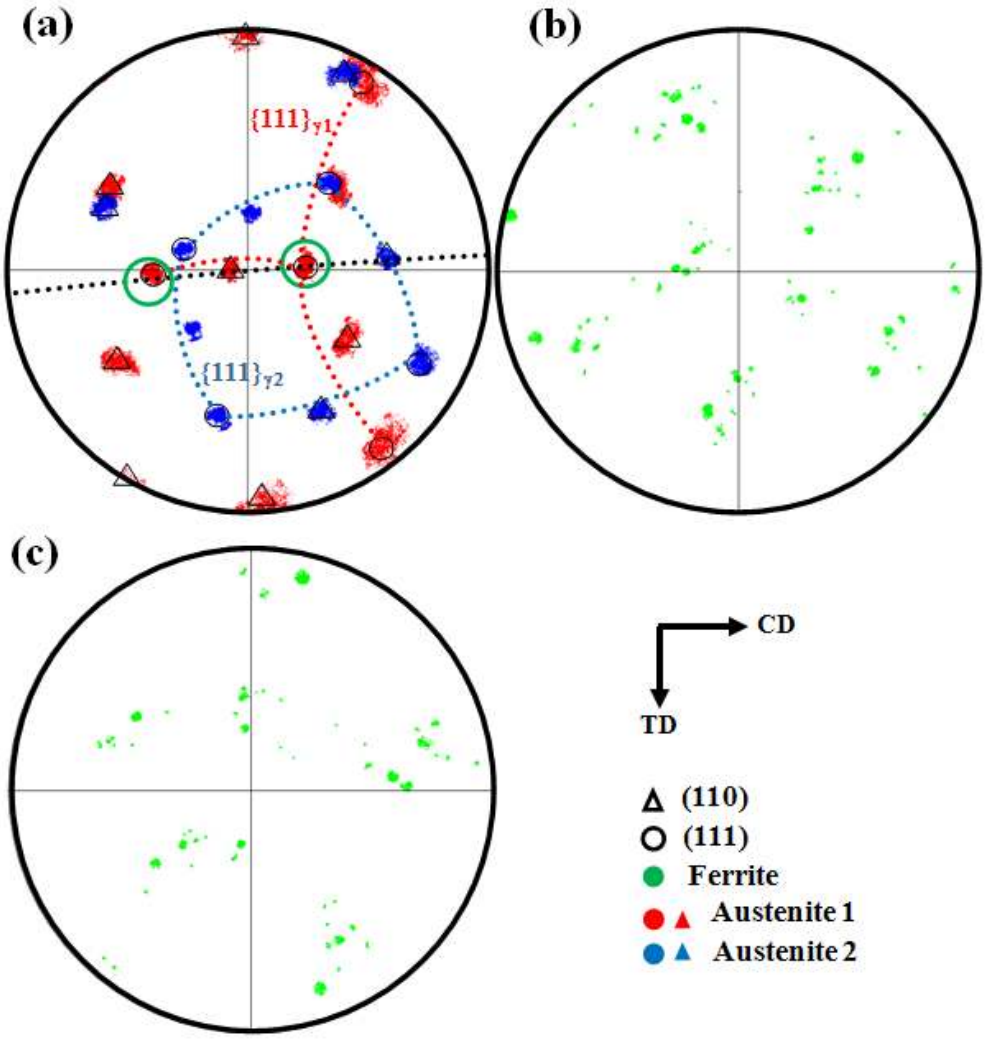


Figure 6.7 (a) {110} and {111} pole figure from two adjacent austenite grains of deformed sample illustrated in Figure 6.6. (b) {110} pole figure and (c) {111} pole figure from ferrite nucleated at boundaries.

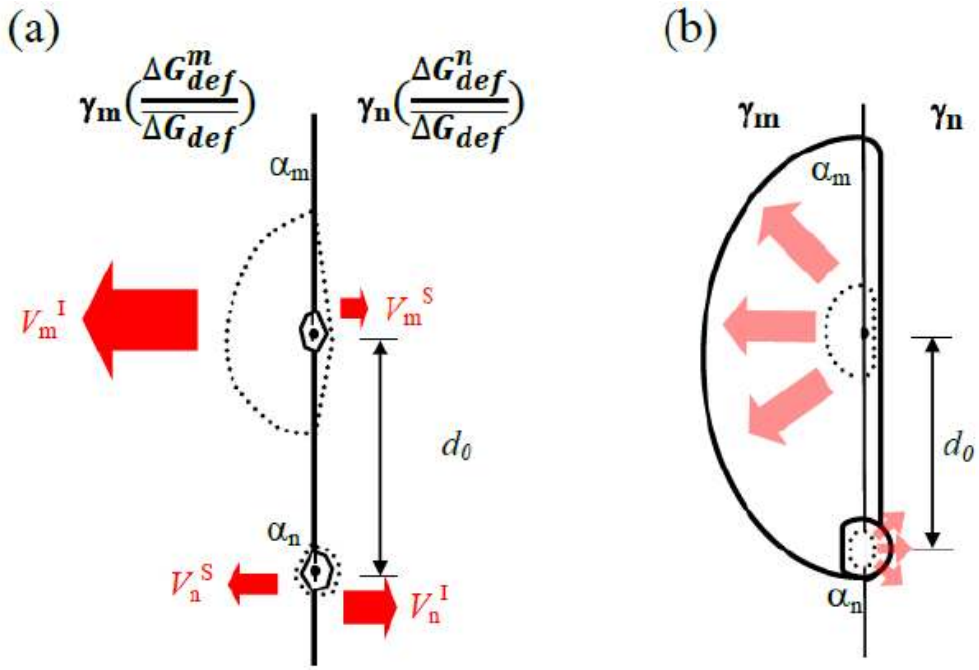


Figure 6.8 A schematic diagram illustrating the relative interface movement velocity to the austenite which have different stored energy $\Delta G_{def}$ (a). $\Delta G^m_{def}$ and $\Delta G^n_{def}$ are correspond to the stored energy of $\gamma_m$ and $\gamma_n$ respectively and $\overline{\Delta G_{def}}$ is the average stored of adjacent austenite grains. (b) shows the condition for stifling the growth of a ferrite grain by adjacent other ferrite grains.

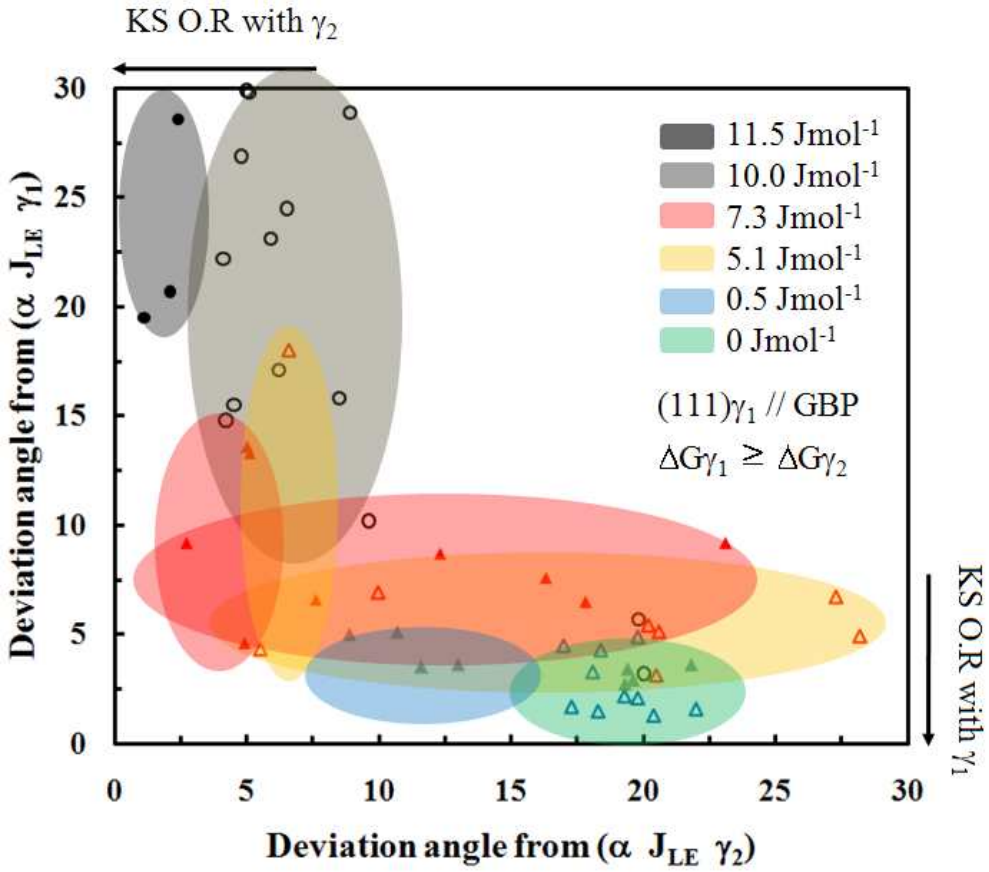


Figure 6.9 The deviation angles from Kurdjumov-Sachs orientation relationship with various stored energy difference between adjacent two austenite grains, $\gamma_1$ and $\gamma_2$.

### 6.3.3 Deformed sample: nucleation at twin boundaries

When grain boundary nucleated ferrite has an orientation relationship with both adjacent austenite grains, it is said to possess 'dual orientation' and $\gamma/\alpha$ interfaces on both sides tend to be semi-coherent. Since dual-orientated ferrite can minimize the interfacial energy compared with the ferrite having orientation relationship with one of the austenite grains, the nucleation of dual oriented ferrite is energetically favorable. However, the chance for ferrite to have dual-orientation is strongly dependent on the orientation of adjacent austenite grains. It was shown in the previous Chapter 5 that the possibility of dual orientation can be increased when neighboring austenite grains have certain CSL orientation relationship such as $\Sigma$ =11 or $\Sigma$=3. Both semi-coherent interface of dual oriented ferrite will have similar interface velocity, which is slower than that of incoherent interface.

Figure 6.10 shows an EBSD map of ferrite nucleated at a twin boundary. Ferrite group 1 and group 2 show the grains nucleated at $\gamma_1/\gamma_2$ and $\gamma_2/\gamma_3$ boundaries. Group A and B correspond to the marked regions A and B respectively in Figure 6.10 (c) and Figure 6.11 (a) and (b) represent the details. Ferrite grains which belong to the same group show a similar morphology as well as crystallographic orientation. The twin boundary trace and $\{111\}_\gamma$, $\{110\}_\gamma$ poles in Figure 6.12 indicate that both austenite grains have $\{111\}_\gamma$ plane nearly parallel to grain boundary plane, which permits the dual orientation of ferrite. Even for ferrite nucleated between austenite grains having different stored energies by deformation, dual orientation is still preferred. Figure 6.13 shows ferrite grains formed at a twin boundary where the

stored energy of adjacent austenite grains $\gamma_1$ and $\gamma_2$ is 26 $Jmol^{-1}$ and 18 $Jmol^{-1}$, respectively. Figure 6.14 shows that one can find $\{111\}_\gamma$ plane in both adjacent austenite grain almost parallel to the grain boundary plane, which enables ferrite to have dual orientation with both austenite. In this case, it is difficult to observe the effect of stored energy on orientation characteristics of ferrite because the interfaces between austenite and ferrite in both sides possibly have semi-coherent boundary, therefore a difference in migrating velocity is difficult to expect.

Meanwhile, Figure 6.15 shows ferrite formed in austenite boundary and its surroundings. The orientation of both austenite grains in Table 6.4 indicates they are twin-related. But the $\{111\}_\gamma$ poles in austenite and the locus of grain boundary plane in Figure 6.16 show that the grain boundary plane is not parallel to twin plane. This means that the ferrite forms in incoherent twin boundary and thus has difficulty to have the dual orientation. One of $\{111\}_\gamma$ planes of $\gamma_2$ grain is approximately parallel to the trace of the boundary plane, which implies that ferrite having orientation relationship with $\gamma_2$ will be favorable with respect to the interfacial energy. However, Table 6.4 indicates that most of ferrite grains have KS relationship with $\gamma_1$ grain. It is noted that the stored energy of $\gamma_1$ and $\gamma_2$ grains by deformation is evaluated to be 18 $Jmol^{-1}$ and 28 $Jmol^{-1}$. This suggests that ferrite grains having incoherent interface with $\gamma_2$ grain can have beneficial effect in growth from the difference in stored energy. The other side of $\gamma/\alpha$ interface of that ferrite is likely to be semi-coherent interface representing the orientation relationship. The orientation characteristics of ferrite in Figure 6.15 reflects growth controlled orientation

characteristics of ferrite can occurs at incoherent twin boundary as well as general high angle boundary provided that sufficient difference in stored energy between adjacent austenite grain is given. Figure 6.17 summarizes analysis results on the orientation characteristics of ferrite which forms along austenite grain boundary.

## 6.4 A Model for growth control

Growth controlled orientation characteristics of ferrite is analogous to the strain-induced selective grain growth during recrystallization in steels in the context of anisotropic growth of product phase [88-90]. However, since the structural transformation is a different process from recrystallization, a separate analysis is necessary to examine quantitatively the effect of anisotropic growth of ferrite on the orientation characteristics. In this section, a simple model is proposed for growth controlling by taking into account the γ/ α interface migration velocity as a function of stored energy in austenite and calculating a critical time for fast growing grain to block the growth of other grain.

### 6.4.1 Representation of interface velocity

During the growth of ferrite, the movement of α/γ interfaces is represented as [91] :

$$v = M\left(\Delta G_{chem} + \Delta G_{def}\right) \tag{6.5}$$

where $\Delta G_{chem}$ is the chemical driving force and interface-controlled growth is implicitly assumed. $M$ is the interface mobility expressed as follows:

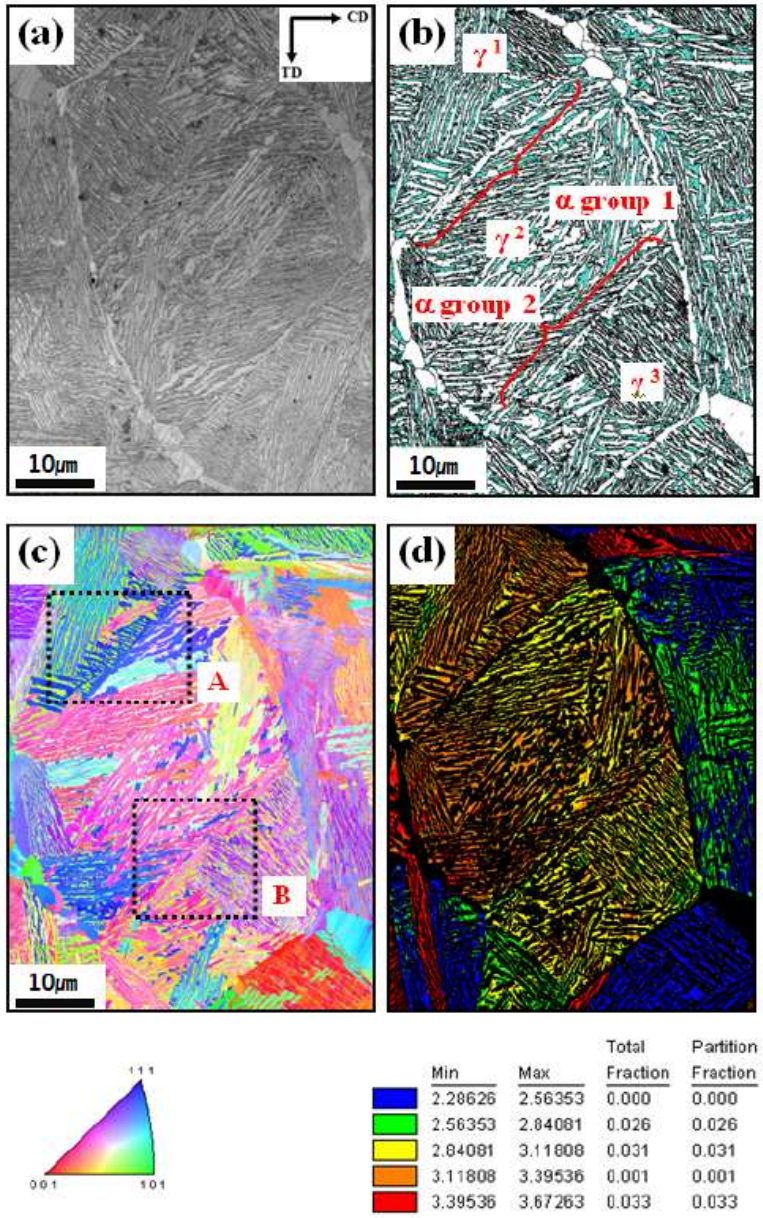


Figure 6.10 Transformation of ferrite nucleated at twin angle boundaries when calculated stored energy of $\gamma_1$ and $\gamma_2$ are 22 $Jmol^{-1}$ and 21 $Jmol^{-1}$ respectively. (a) image quality map, (b) phase map with blue corresponding to the austenite and white to allotriomorphic ferrite or bainitic ferrite, (c) orientation map and (d) Taylor factor map.

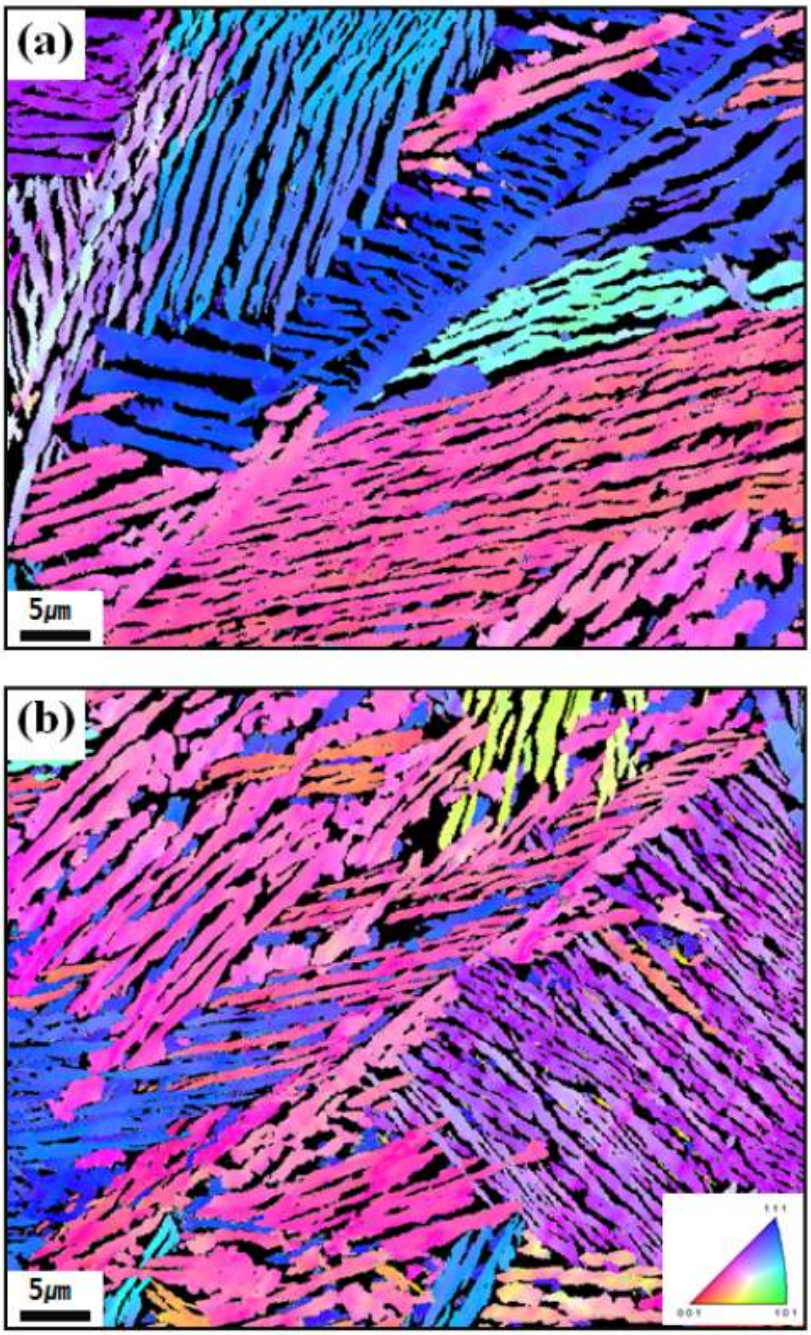


Figure 6.11 Orientation map of magnified area. (a) and (b) corresponds to the section **A** and **B** respectively in Figure 6.9 (c).

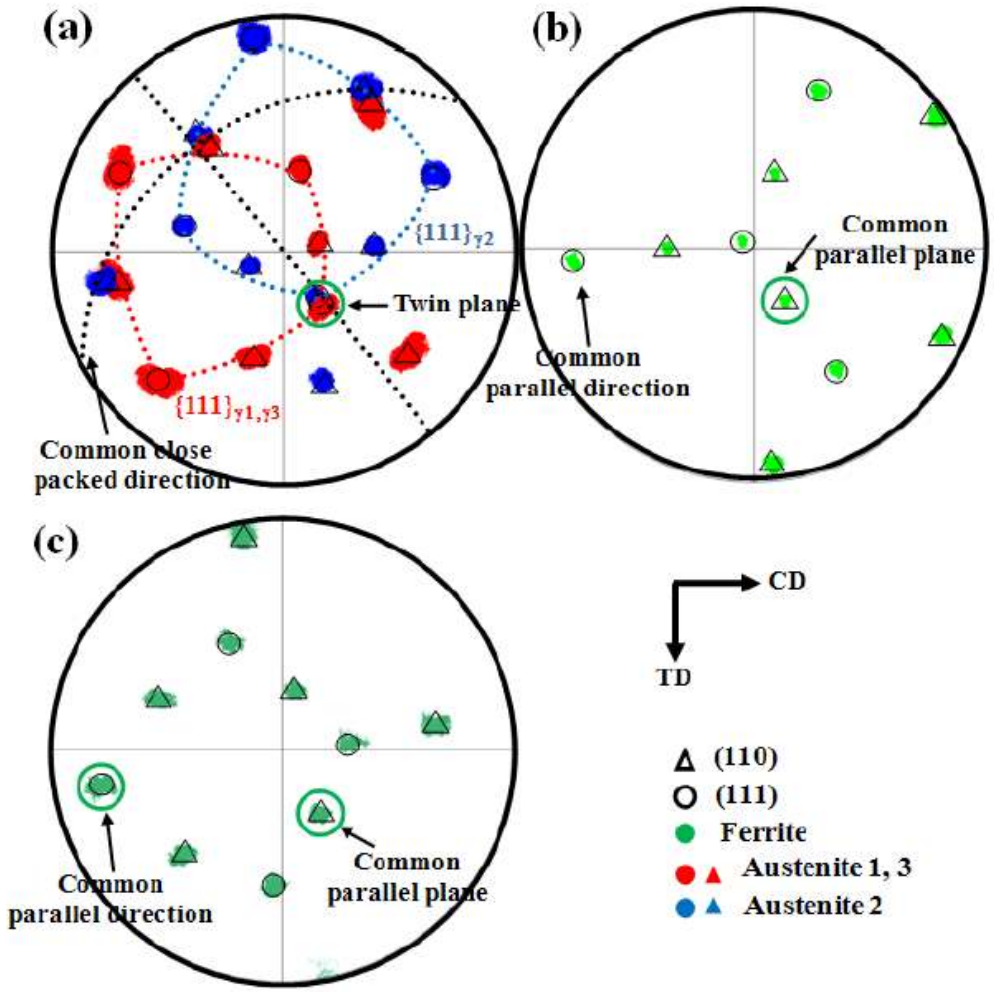


Figure 6.12 (a) {110} and {111} pole figure from two adjacent austenite grains of deformed sample illustrated in Figure 6.10. (b) and (c) are {110} and {111} pole figure from ferrite in section **A** and section **B** respectively. Notice that the orientation of 1 and 3 are almost same.

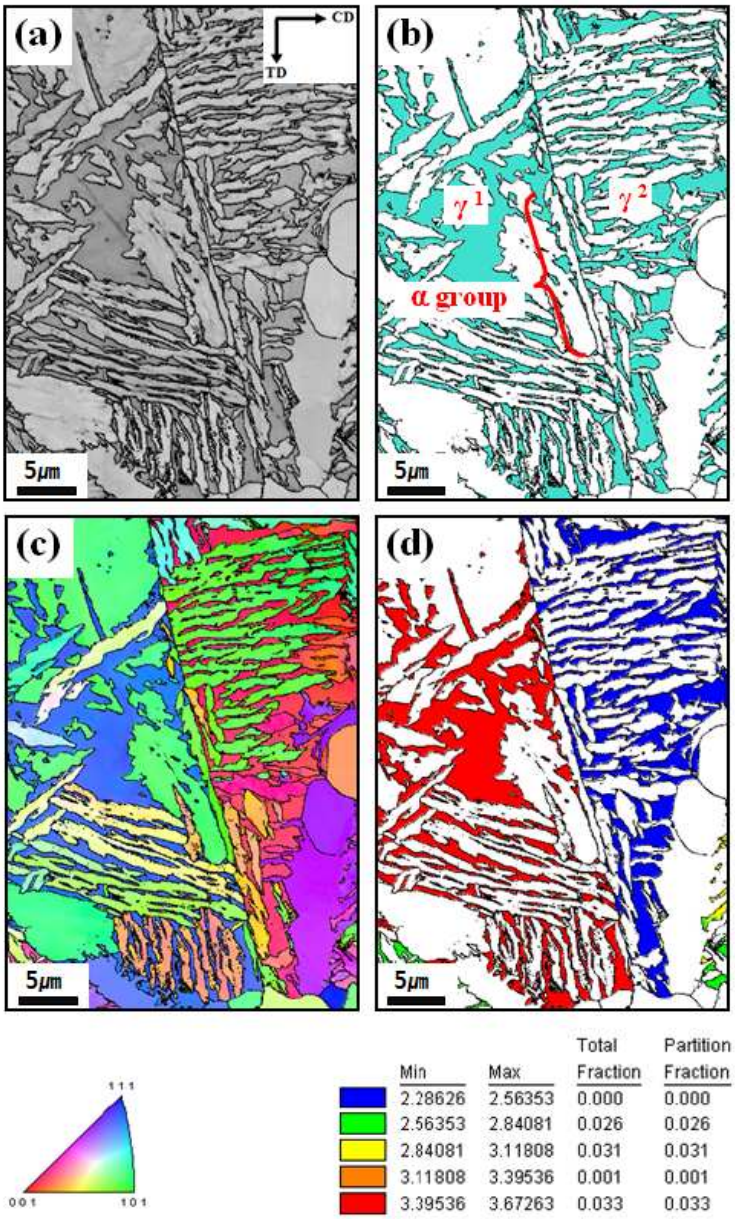


Figure 6.13 Transformation of ferrite nucleated at twin angle boundaries when calculated stored energy of 1 and 2 are 26 $Jmol^{-1}$ and 18 $Jmol^{-1}$ respectively. (a) image quality map, (b) phase map with blue corresponding to the austenite and white to allotriomorphic ferrite or bainitic ferrite, (c) orientation map and (d) Taylor factor map.

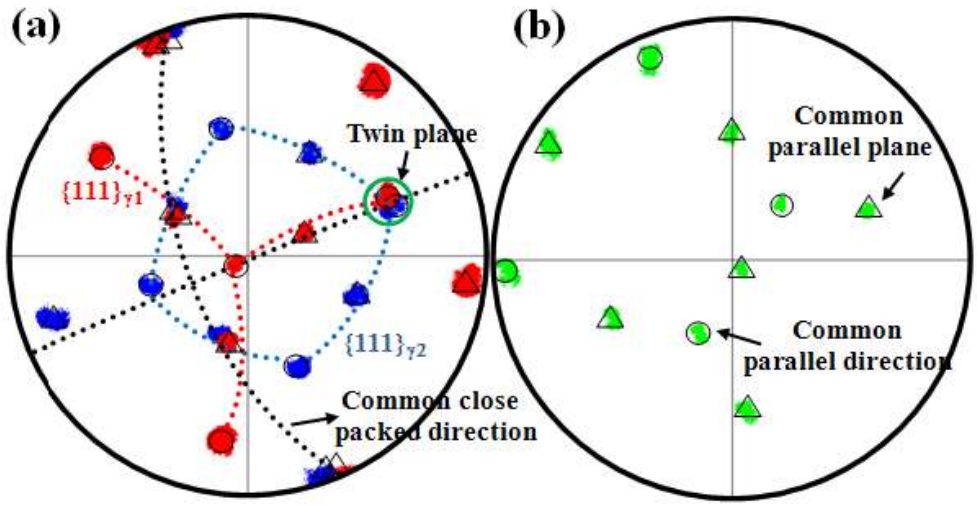


Figure 6.14 {110} and {111} pole figure from two adjacent austenite grains of deformed sample illustrated in Figure 6.12. (b) {110} and {111} pole figure of ferrite.

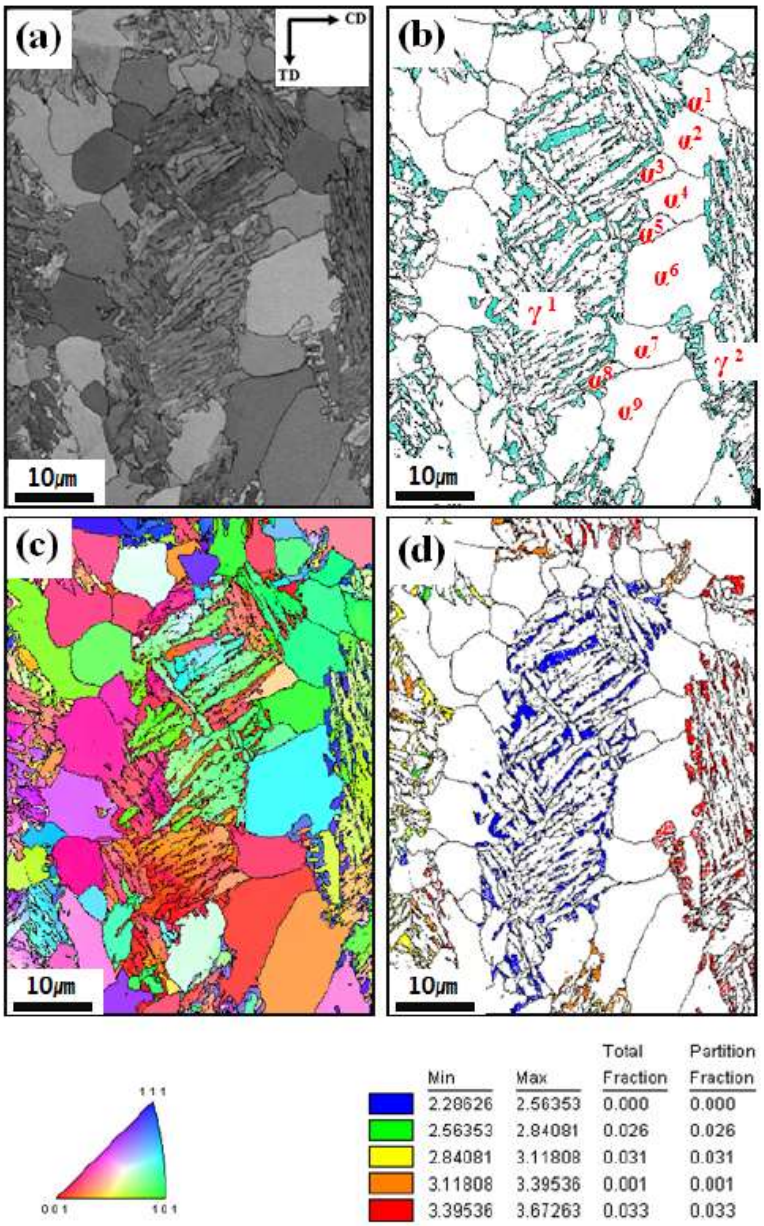


Figure 6.15 Transformation of ferrite nucleated at incoherent twin angle boundaries when calculated stored energy of $\gamma_1$ and $\gamma_2$ are 18 $Jmol^{-1}$ and 28 $Jmol^{-1}$ respectively. (a) image quality map, (b) phase map with blue corresponding to the austenite and white to allotriomorphic ferrite or bainitic ferrite, (c) orientation map and (d) Taylor factor map.

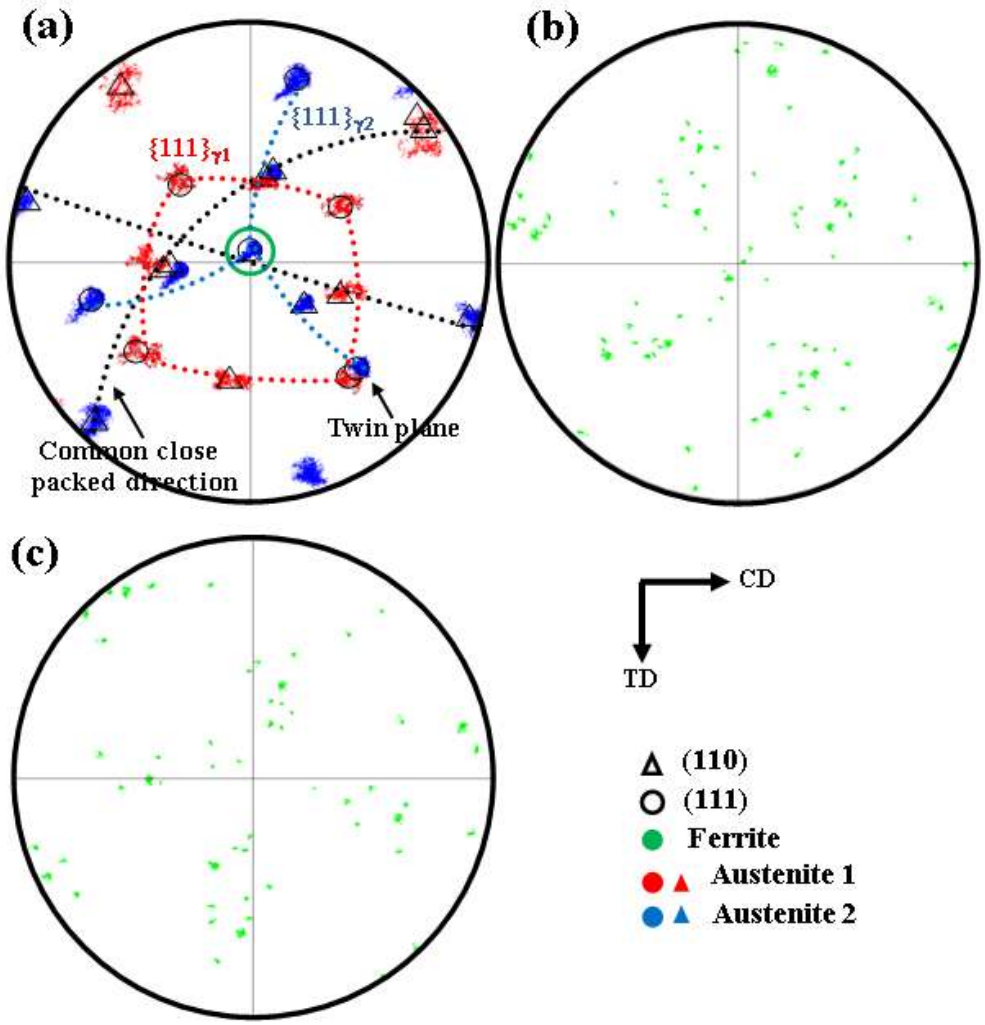


Figure 6.16 (a) {110} and {111} pole figure from two adjacent austenite grains of deformed sample illustrated in Figure 6.14. (b) {110} pole figure and (c) {111} pole figure from ferrite nucleated at boundaries.

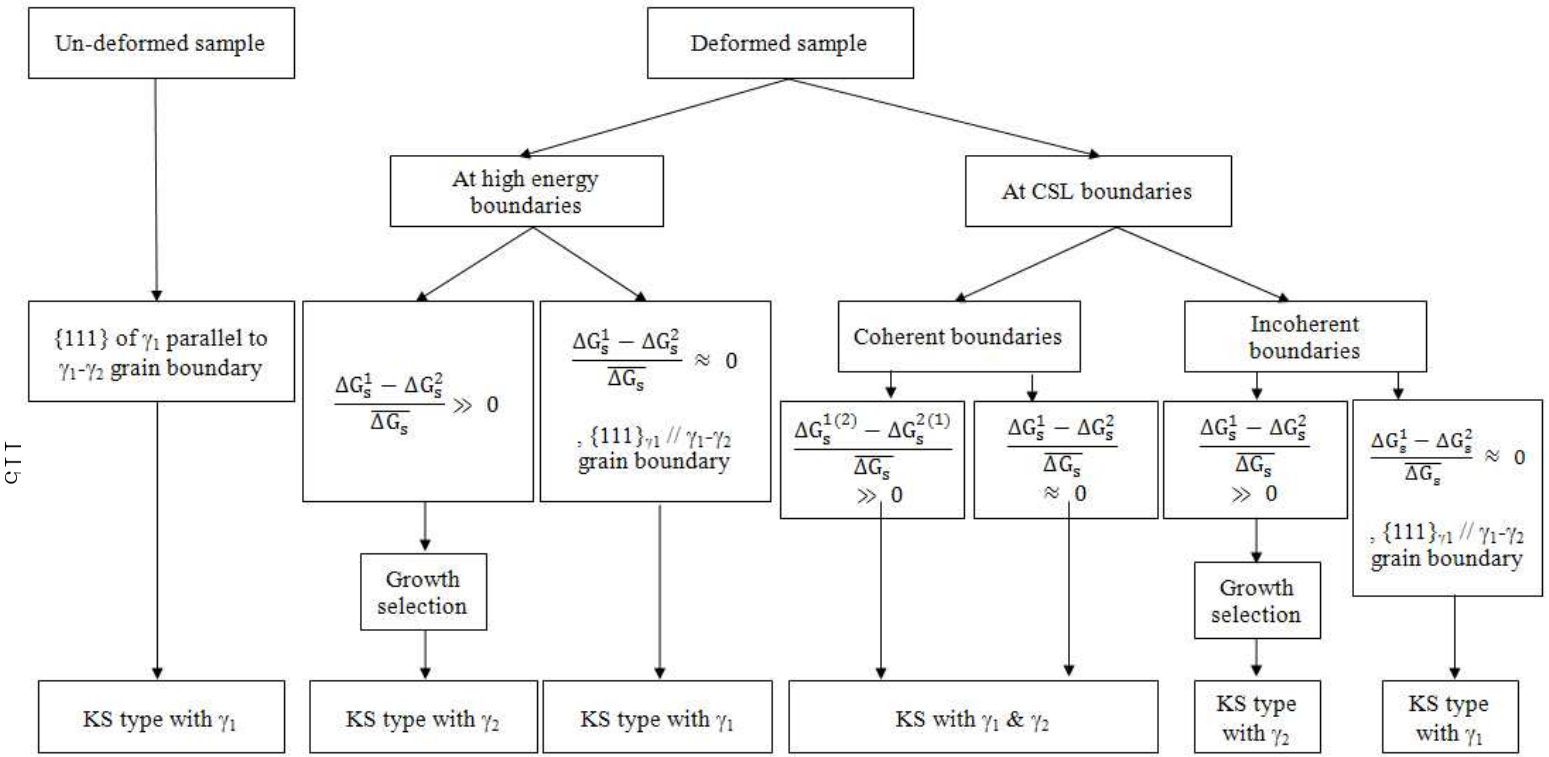


Figure 6. 17 Diagram illustrating the total summary of experimental results. Remember that $\Delta G_s^1$ and $\Delta G_s^2$ is the stored energy by strain field of dislocations in each $\gamma_1$ and austenite $\gamma_2$ grains respectively. $\overline{\Delta G_s}$ is the mean strain energy between two adjacent austenite grains

$$M = M_0 \exp\left(-\frac{Q_M}{RT}\right) \quad (6.6)$$

Here, $M_0$ is pre-exponent and $Q_M$ is the activation energy for migration of iron tom across the interface. Combining 6.5 and 6.6 will give the interface velocity as:

$$v = M_0 \exp\left(-\frac{Q_M}{RT}\right)\left(\Delta G_{chem} + \Delta G_{def}\right) \quad (6.7)$$

$\Delta G_{def}$ is a combination of a intrinsic stored energy during deformation(negative value) and a plastic lattice misfit strain energy (positive value). If there is 0.6% misfit during ferrite transformation at 700℃, elastic strain energy is calculated as about 10 $\mathrm{MJm^{-3}}$ [92]. Since ideal plastic strain energy is around a tenth of elastic strain energy [93, 94], the total plastic strain energy during deformation is close to 1 $\mathrm{MJm^{-3}}$. Considering the normal intrinsic stored energy in heavily worked austenite is about 180 J/mol (25 $\mathrm{MJm^{-3}}$), plastic strain energy by lattice misfit can be negligible so, only intrinsic stored energy was regarded as total deformation energy. The pre-exponential factor $M_0$ is reported to be around 58 and 29 mm mol $\mathrm{J^{-1}s^{-1}}$ for incoherent and semi-coherent interfaces [91, 95] respectively. $Q_M$ is known to be about 140 kJ/mol for the incoherent boundary [96, 97] but there are few available values for the semi-coherent interface. Recently, Santofimia et al [98] reported that 180 kJ/mol for the semi-coherent boundary showed a good agreement with experimental results in calculating the phase fraction. So the same value is assumed here.

### 6.4.2 A condition for growth controlling

The growth controlling of orientation characteristics of ferrite in Figure 6.8 suggests a possibility that the growth of $\alpha_n$ can be blocked by $\alpha_m$ which has faster growth kinetics due to the difference in stored energy of adjacent austenite grains. As shown in Figure 6.8 (b), assuming $d_0$ is a distance between two ferrite nuclei, the critical time ($t_c$) for faster growing $\alpha_m$ to successfully block its neighbor will be given as:

$$(v_m^I - v_n^I)t \geq d_0 \tag{6.8}$$

The number of precipitates per unit area of grain boundary can be calculated from the nucleation rate per unit area boundary and time for nucleation.

$$N_A = \boldsymbol{I}\boldsymbol{t} \tag{6.9}$$

For t=1s (site saturation of ferrite nuclei was over within 1s), $d_0$ is:

$$d_0 = \sqrt{\frac{1}{N_A}} \tag{6.10}$$

According to the classical approach to the nucleation rate explained on section 2.3, $I$ per unit area of boundary can be expressed as follows:

$$I = \frac{k_B T}{h} n_s^f \exp\left\{-\frac{\left(K_2^f G^* + Q\right)}{k_B T}\right\} \tag{6.11}$$

where $n_s^f$ is a site factor representing the density of nucleation sites per unit area of boundary, which is given by:

$$n_s^f = K_1^f \frac{1}{2\delta^2} \tag{6.12}$$

where δ means atomic spacing and taken as $2.5\times10^{-10}$m [29]. $K_1^f$ is a factor expressing the fraction of the total number of face sites set as $6.9\times10^{-8}$ and $K_2^f$ is a shape factor affecting the γ/ α interface boundary energy per unit area taken as $2.6\times10^{-3}$. $Q$ is an activation energy for self diffusion of iron, 240 kJ/mol [25]. The critical free energy barrier, $G^*$, is given by:

$$G^* = \frac{16\pi\sigma_{\gamma\alpha}^3}{3\left(\Delta G_{chem} + \Delta G_{def}\right)^2} \tag{6.13}$$

Here, $\sigma_{\gamma\alpha}$ is interfacial energy which is supposed to be 0.992 J/m$^2$ [99] for incoherent boundary and 0.03 $\mathrm{Jm}^{-2}$ for a semi-coherent interface [91]. The molar chemical driving force $\Delta G_{chem}$ represented in figure. 2.3 was calculated as -209 $\mathrm{Jmol}^{-1}$ by using MatCalc software package [100] when $Ae_3$ temperature is 835℃. Combining Equation 6.10 to 6.13 will bring the critical time which is necessary, as mentioned for ferrite which has faster growth kinetics to obstruct the neighboring ferrite grains. The change of the critical time will describe a relative possibility of growth controlling depending on the difference in stored energy of adjacent austenite grains or the grain boundary characteristics of austenite.

## 6.5 Analysis from the calculation results

In equation 6.8, we can calculate the critical time for variant selection, $t_c$ by growth control when growth length of $\alpha_m$ is equal to $d_0$ added growth length of $\alpha_m$ This value can be used as a criterion to evaluate the possibility of growth control by

comparing the time with total transformation time of allotriomorphic ferrite. If $t_c$ is quite smaller than transformation time, it would be acceptable to think that local variant selection during diffusional transformation is determined by growth control.

Figure 6.18 shows the change of critical time for growth controlling at conventional high angle boundary as a function of the stored energy difference and chemical driving force. It indicates that an increase in stored energy difference will shorten the critical time, making growth control occur readily. Figure 6.18 also indicates an increase of chemical driving force will decrease the critical time, promoting the occurrence of growth controlled orientation selection. This is quite different from the effect of chemical driving force on orientation characteristics of bainite and martensite. For displacive transformations, the orientation of product phase is influenced by the interaction between shape deformation and externally applied stress or strain and the orientation is more strongly affected by the interaction as the ratio of chemical driving force to overall driving force ($\triangle G_{chem}/(\triangle G_{chem}+\triangle G_{def})$) decreases [67]. The effect of chemical driving force on growth controlled orientation selection comes from the change of the distance between ferrite nuclei, $d_0$. When $\triangle G_{chem}$ is 200, 150, 100, 50 $Jmol^{-1}$, $d_0$ is calculated to be 0.03, 0.05, 0.12 and 0.57$\mu$m. It is because fewer nucleation sites are activated as the driving force is decreased. Consequently, for given stored energy difference, smaller chemical driving force will require more time for faster growing ferrite to block the neighboring ferrite. In other words, unlike to the displacive

mechanism, growth controlled orientation selection will readily occur as the chemical driving force increases.

It is confirmed experimentally that the growth controlled orientation characteristics is hardly observed even with difference in stored energy provided that ferrite can make a dual orientation with both austenite grains. This situation is captured in calculation by regarding all interfaces between ferrite and austenite as semi-coherent interface, assuming $M_0$ and $Q_M$ in Equation 6.6 to be 29 mm mol J $^{-1}$s$^{-1}$, 180 kJmol$^{-1}$. The calculation results in Figure 6.19 show similar trend on the effect of stored energy difference and chemical driving force compared with previous figure. But it is noted that the critical time for growth controlling is drastically prolonged. The calculated critical time implies that the growth controlling is actually difficult to occur. This indicates that the difference in stored energy is not that effective when ferrite has the dual orientation because the slower growth kinetics of semi-coherent boundary makes it difficult to utilize the energetic advantage and that is why we cannot observe the growth controlled orientation characteristics of ferrite nucleated along coherent twin boundary of austenite.

## 6.6 Conclusions

The orientation characteristics of ferrite nucleated along a grain boundary have been investigated. It is confirmed that orientation is affected by that of the boundary plane relative with respect to the close-packed planes in the adjacent austenite grains and the deformation of austenite prior to ferrite formation. The following

conclusions can be drawn:

(1) When transformation is from undeformed cases, the orientation of γ/ γ grain boundary plane has a major influence on that of ferrite. Ferrite adopts an orientation relationship in which the $\{111\}_{\gamma}$ plane becomes the most parallel to that of the grain boundary, consistent with Lee et al.

(2) The orientation characteristics of allotriomorphic ferrite which forms from deformed austenite can be classified into two classes. When the stored energy of adjacent austenite grain is negligible, orientation of ferrite is mainly influenced by the orientation of grain boundary plane, i.e. the close-packed plane is nearly parallel to the grain boundary plane. Meanwhile, when difference of the stored energy is remarkable, the criterion by orientation of grain boundary plane does not describe well the orientation characteristics of ferrite. The orientation analysis indicates that the ferrite is likely to have the orientation relationship with austenite grain with lower stored energy. It allows the ferrite to have incoherent interface with the other austenite grain with higher stored energy, which possibly provides energetic advantage in growth. At coherent twin boundary along which the ferrite can have a dual orientation with both austenite grain, the orientation characteristics of ferrite is mostly governed by the dual orientation phenomena regardless the difference in stored energy of austenite grains.

(3) A model for growth controlled orientation selection is proposed. The calculation results successfully capture the influence of the stored energy difference of

adjacent austenite as well as the grain boundary characteristics on the occurrence of growth controlled orientation selection in allotriomorph ferrite formation.

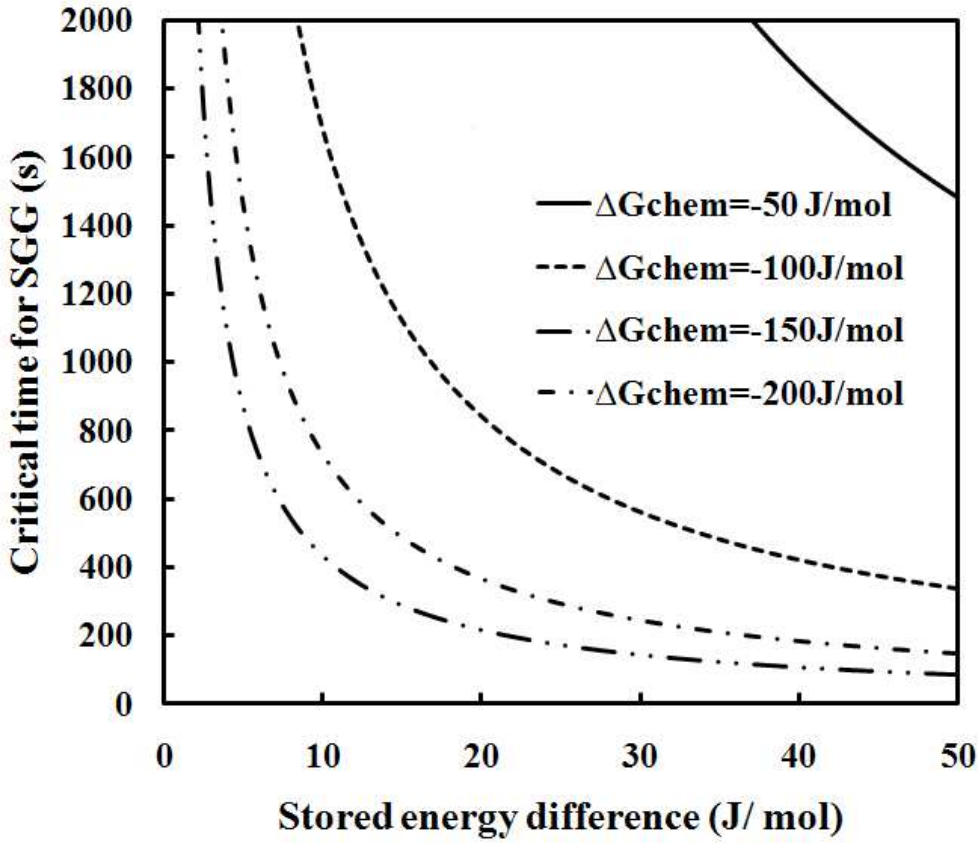


Figure 6.18 Calculations result of critical time for selective growth according to the chemical driving force for transformation and stored energy difference between austenite grains when ferrite nucleate at high energy boundary.

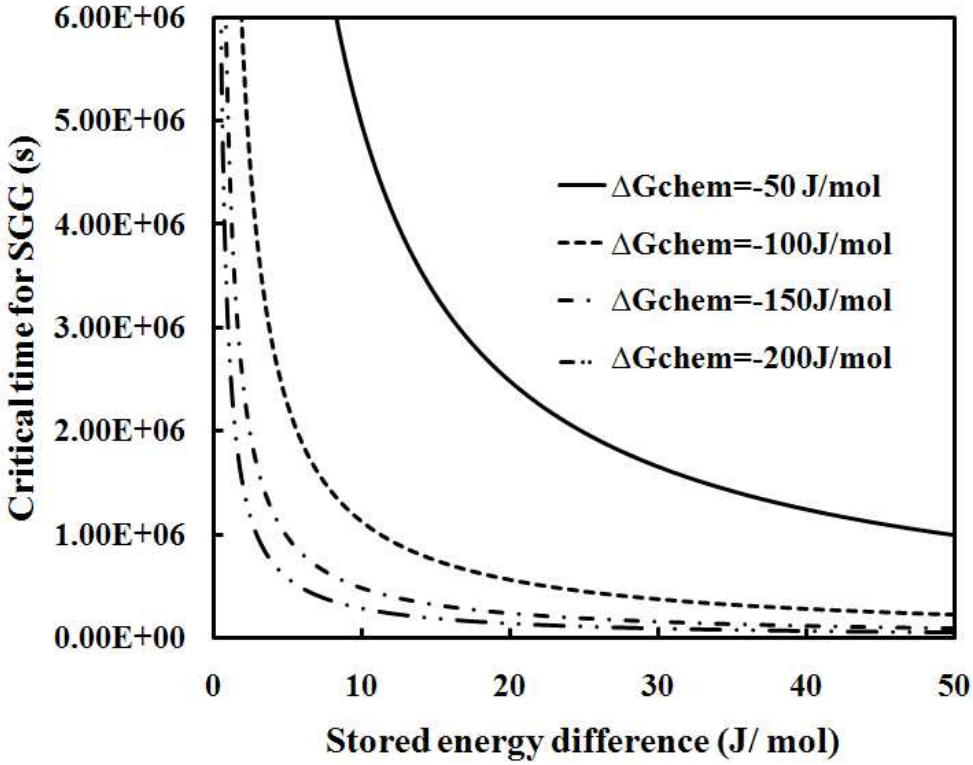


Figure 6.19 Calculations result of critical time for selective growth according to the chemical driving force for transformation and stored energy difference between austenite grains when ferrite nucleate at twin boundary.

Table 6.2 Deviation from the exact Kurdjumov-Sachs orientation for the ferrite grains illustrated in Figure 6.4

| Grain | Deviation axis-angle from KS relationship | | | | Σ |
|---|---|---|---|---|---|
| | with respect to r1 | | with respect to r2 | | |
| $\alpha^1$ | [0.43 -0.01 0.90] | 2.7° | [0.59 -0.68 0.41] | 19.3° | |
| $\alpha^2$ | [-0.19 -0.40 0.89] | 5.0° | [0.18 -0.27 -0.94] | 8.87° | |
| $\alpha^3$ | [0.94 0.16 0.28] | 2.9° | [0.44 0.70 0.54] | 19.6° | |
| $\alpha^4$ | [-0.92 0.16 0.35] | 3.6° | [0.37 0.27 -0.88] | 21.8° | |
| $\alpha^5$ | [-0.97 0.08 0.23] | 3.4° | [0.36 -0.92 -0.12] | 19.4° | |
| $\alpha^6$ | [-0.8 0.11 -0.59] | 3.6° | [-0.41 -0.13 0.90] | 13.0° | |
| $\alpha^7$ | [-0.45 -0.01 -0.89] | 5.1° | [-0.35 0.01 0.93] | 10.7° | |
| $\alpha^8$ | [-0.11 0.14 -0.98] | 3.5° | [-0.19 -0.09 0.96] | 11.6° | |
| $\gamma^1$ | [-0.43 0.28 0.85] | 38.2° | - | | - |
| $\gamma^2$ | - | | [-0.43 0.28 0.85] | 38.2° | - |

Table 6.3 Deviation from the exact Kurdjumov-Sachs orientation for the ferrite grains illustrated in Figure 6.6

| Grain | Deviation axis-angle from KS relationship | | | | Σ |
|---|---|---|---|---|---|
| | with respect to r1 | | with respect to r2 | | |
| $\alpha^1$ | [0.09 0.54 0.84] | 24.5° | [-0.2 -0.32 -0.92] | 6.53° | |
| $\alpha^2$ | [-0.96 -0.03 -0.27] | 17.1° | [-0.02 0.95 -0.08] | 6.17° | |
| $\alpha^3$ | [-0.55 0.68 0.47] | 26.84° | [-0.09 -0.04 -0.99] | 4.81° | |
| $\alpha^4$ | [0.64 0.44 0.62] | 30.4° | [0.32 -0.15 -0.93] | 5.02° | |
| $\alpha^5$ | [-0.16 -0.92 0.35] | 15.84° | [0.02 0.37 -0.92] | 8.47° | |
| $\alpha^6$ | [0.18 -0.54 -0.82] | 32.4° | [0.18 0.45 0.87] | 4.84° | |
| $\alpha^7$ | [0.54 -0.68 -0.49] | 28.9° | [0.92 -0.27 -0.26] | 8.86° | |
| $\alpha^8$ | [0.81 0.49 0.24] | 3.2° | [-0.1 -0.70 0.64] | 20.0° | |
| $\alpha^9$ | [0.99 0.104 0.01] | 5.74° | [-0.10 -0.73 0.68] | 19.8° | |
| $\alpha^{10}$ | [0.10 0.99 -0.06] | 14.81° | [-0.71 -0.02 0.69] | 4.21° | |
| $\alpha^{11}$ | [-0.71 0.69 -0.03] | 10.2° | [0.85 0.24 0.45] | 9.6° | |
| $\alpha^{12}$ | [-0.86 0.47 -0.11] | 15.5° | [0.38 0.91 -0.12] | 4.47° | |
| $\alpha^{13}$ | [0.70 0.61 -0.36] | 23.1° | [0.06 -0.67 0.73] | 5.88° | |
| $\alpha^{14}$ | [-0.23 0.82 0.517] | 30.4° | [0.59 -0.35 0.71] | 5.08° | |
| $\alpha^{15}$ | [0.98 -0.18 -0.04] | 22.2° | [0.75 -0.53 0.37] | 4.05° | |
| $\gamma^1$ | [0.43 -0.89 -0.10] | 36.0° | - | | - |
| $\gamma^2$ | - | | [0.43 -0.89 -0.10] | 36.0° | - |

Table 6.4 Deviation from the exact Kurdjumov-Sachs orientation for the ferrite grains illustrated in Figure 6.14

| Grain | Deviation axis-angle from KS relationship | | | | Σ |
|---|---|---|---|---|---|
| | with respect to r1 | | with respect to r2 | | |
| $\alpha^1$ | [0.70 0.28 0.65] | 7.8° | [0.56 0.19 0.80] | 16.6° | |
| $\alpha^2$ | [0.79 0.31 0.52] | 12.0° | [0.57 0.81 -0.07] | 14.0° | |
| $\alpha^3$ | [0.54 -0.39 -0.75] | 8.3° | [0.23 0.9 0.3] | 12.3° | |
| $\alpha^4$ | [-0.05 -0.95 0.3] | 5.4° | [0.82 0.45 0.34] | 18.3° | |
| $\alpha^5$ | [-0.12 -0.9 0.34] | 5.7° | [0.1 -0.85 -0.5] | 19.0° | |
| $\alpha^6$ | [0.05 0.98 0.13] | 9.4° | [-0.18 -0.98 0.01] | 16.7° | |
| $\alpha^7$ | [0.20 -0.59 -0.77] | 3.9° | [0.12 0.77 -0.62] | 15.0° | |
| $\alpha^8$ | [-0.93 0.35 0.01] | 2.0° | [0.06 0.53 -0.84] | 6.7° | |
| $\alpha^9$ | [0.86 -0.08 0.49] | 4.4° | [-0.97 -0.23 0.05] | 19.6° | |
| $\gamma^1$ | [-0.61 -0.63 0.57] | 59.3° | - | | 3 |
| $\gamma^2$ | - | | [-0.61 -0.63 0.57] | 59.3° | 3 |

# Chapter 7 Texture Prediction by Artificial Neural Network Approach

## 7.1 Introduction

Interstitial free (IF) steels have been used widely in the automotive industry for last couple of decades because of their excellent formability which enables automobile body panels to be manufactured in complicated shapes. With the ongoing necessity for weight reduction, recent trends on IF steels have focused on stronger varieties to create category designed interstitial free high-strength steels (IFHS). However, a deterioration of deep drawability has been reported [101, 102] due to P and Mn addition which solution strengthens.

Deep drawability related with the existence of the γ-fibre texture (ND// $\{111\}_{\alpha}$) development during recrystallization stage, known to be controlled by the chemical composition and processing route, especially the extent of cold rolling [103-106]. It is therefore important to understand the effect of each alloying element and cold rolling condition on the formation of γ-fibre texture. The precipitation behavior in IFHS steels has been studied [33, 101, 102, 107, 108] however, quantitative analysis in terms of according to the Mn, P and Ti contents was not carried out. The effect of cold rolling condition on the γ-fibre texture has been comparatively well-investigated but, the mechanism for texture development is known to be different according to the amount of reduction [104, 109, 110]. With this in mind, the present study focused on the prediction of γ-fibre texture using artificial neural network.

## 7.2 Details of modeling

A neural network is a parameterized nonlinear model and its flexibility makes it able to discover more complex relationships in data than traditional statistical models [111]. Bayesian probability theory was used to provide a unifying framework for data modeling which offers several benefits in solving over fitting problem and handling uncertainty as natural manner [112-115]. The variables included in the dataset accumulated for analysis are listed in Table 7.1 along with the means and standard deviations. The full 1064 set consisted of experiments collected from published data. The comparison of measured values and calculated values using fully trained committee of model is illustrated in Figure 7.1 in terms of texture intensity. It shows almost a linear fit to the entire data set, which indicates fully trained committee-models in this work, is in accord with the real experimental data.

## 7.3 Results and discussions

To investigate the γ-fibre texture development after recrystallization according to the amount of strains, different cold rolling reduction rate was applied for calculation and Figure 7.2 shows the calculated intensity. The average uncertainty value of predicted was about 9.94(×random). Under the severe reduction rate over 85%, results showed the general tendency that γ-fibre texture intensity continuously and gradually increased all over the section as reduction rate increased.

Table 7.1 Properties of the dataset used in creating the neural network models

| Variables | Minimum | Maximum | Average | St.Dev. |
|---|---|---|---|---|
| C (wt%) | 0.0019 | 0.0045 | 0.0035 | 0.0006 |
| Mn (wt%) | 0.006 | 0.84 | 0.3333 | 0.2254 |
| Si (wt%) | 0 | 0.047 | 0.0106 | 0.0146 |
| P (wt%) | 0 | 0.091 | 0.0363 | 0.0291 |
| S (wt%) | 0.0033 | 0.014 | 0.0072 | 0.0019 |
| Al (wt%) | 0 | 0.051 | 0.0258 | 0.0215 |
| Ti (wt%) | 0.035 | 0.07 | 0.052 | 0.0122 |
| Nb (wt%) | 0 | 0.043 | 0.0118 | 0.0128 |
| B (wt%) | 0 | 0.004 | 0.0009 | 0.0014 |
| N (wt%) | 0.0014 | 0.004 | 0.0032 | 0.0006 |
| crr (%) | 50 | 98 | 75.9429 | 12.8034 |
| AnTemp. (°C) | 650 | 833 | 705.1071 | 45.7922 |
| pi1(degree) | 0 | 90 | 47.5 | 28.14 |
| pi(degree) | 45 | 45 | 45 | 0 |
| Intensity (×random) | 0 | 22.2 | 5.548 | 4.3666 |

- AnTemp. : annealing temperature (℃)
- Phi1($\varphi_1$), Pi($\Phi$) : Euler angles (degree)
- Intensity (×random) : multiples of intensity with respect to a random or uniform distribution of orientations

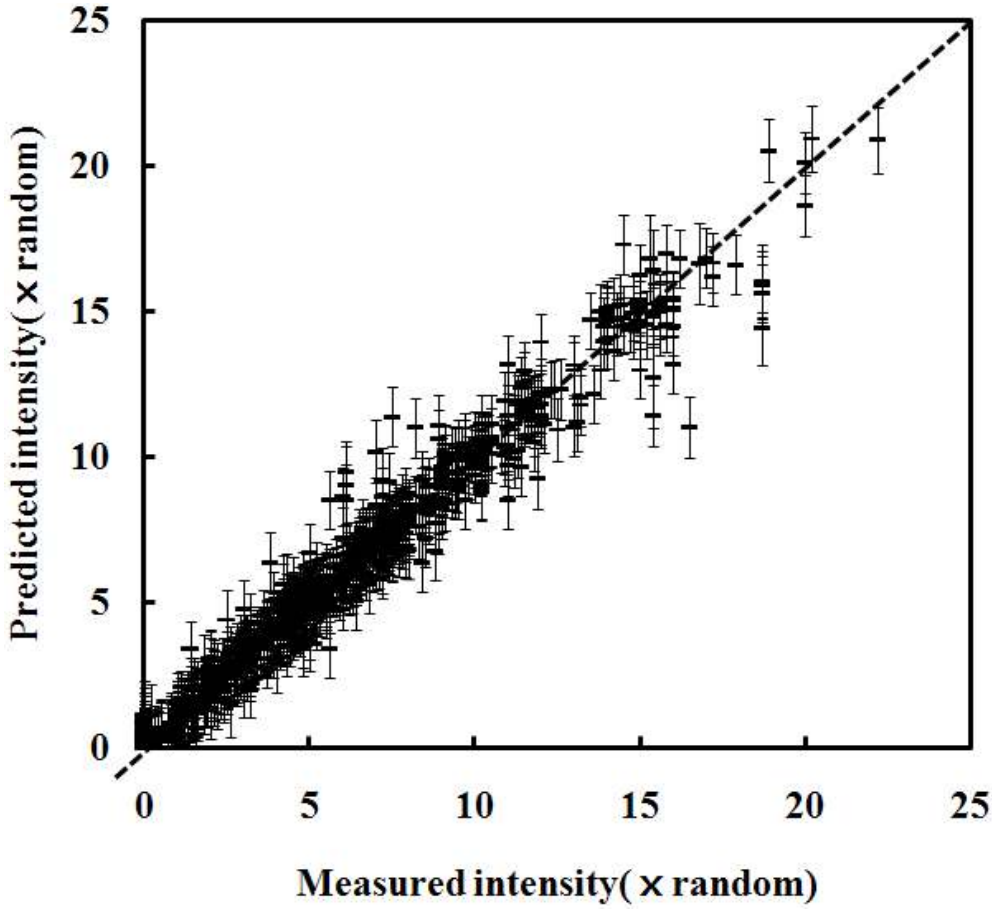


Figure 7.1 Comparison of measured and values calculated using the fully trained committee of models. The unit of texture intensity is the multiples of intensity with respect to a random or uniform distributed orientation.

As reduction rate decrease however, it was observed that there was no significant changes in {111}⟨110⟩ component and maximum intensity moved toward {111}⟨110⟩ from {111}⟨112⟩. Since {112}⟨110⟩ component of α-fibre texture into which {111}⟨112⟩ component can selectively grow is developed by the increase of cold rolling reduction rate [116], it would be reasonable to think that the change of {111}⟨110⟩ become smaller and smaller as the cold rolling reduction rate decreases.

Another important factor in γ-fibre texture would be an influence of recrystallization temperature because it is not only directly involved in the growth velocity of recrystallized grain but also closely connected with the formation of various types of precipitation. Figure 7.3 shows the formation of various Ti compounds according to the temperature change for recrystallization. Fe(Ti+Nb)P is known to be harmful for {111} texture development because it brings the consumption of Ti and Nb leading to the reduction of stabilizing elements in alloys to fix the C and N. For different reasons, TiC is known to sharpen the intensity of γ-fibre texture [108]. The prediction in Figure 7.4 clarifies this temperature-dependent texture change. The uncertainty of the result at 700℃ which was used for data set was calculated as 0.95 and the maximum intensity was 7.1 for this temperature. Since there was lack of data in the range from 720℃ to 780℃, the predicted intensity had quite higher uncertainty as 5.0 than 700℃. However, predicted results showed very good accordance with the microscopic observation results in Figure 7.3 that texture intensity especially in {111}⟨112⟩ component decrease dramatically

as annealing temperature decrease when temperature 720℃.

Since these precipitates have different chemical compositions, P, Mn and Ti may also affect to change of γ-fibre texture. Based on the model, texture intensity was calculated according to the P and Mn contents as well as Ti contents and the results are displayed in Figure 7.5. The annealing temperature and cold rolling reduction was assumed to be 700℃ and 55% respectively. P content was changed from 0.051 wt. % to 0.091 wt. % in Figure 7.5 (a) and Mn from 0.04 wt. % to 0.84 wt. % in Figure 7.5 (b). Both calculated results shows similar trends that texture intensity decrease sharply as P and Mn contents increase. This is thought to be related with the diffusivity of carbon according to the P and Mn contents. It is well known that both Mn and P strongly interact with C [117] and so, decrease the diffusivity of C in the matrix. Consequently, TiS formed in high temperature in Figure 7.3 would not be transformed into $Ti_4C_2S_2$ and TiC which have benefit to make {111} texture [108]. It is noticeable here that the absolute value of maximum intensity change according to the Mn content is much larger than one of P content, which implies the interaction of Mn with C is exceedingly stronger than P.

Ti effect has been well explained in many studies [118-120]. Generally it has been known that FeTiP always formed before the formation of TiC in high Ti steel whose Ti content is around 0.06 wt. % however, in low Ti steel, weight percent of TiC precipitation increase at the temperature over 700℃. So, γ-fibre texture intensity was assumed to be increased according to the Ti content only in the low Ti content range. Texture intensity was calculated when Ti content changes from 0.027%

to 0.067 wt. % and the result in Figure 7.5 (c) properly coincide with the suggestion from previous works. The intensity increased up to the 0.047 wt. % and after that, it decreased. Differently from the previous result, however if we changes the P contents from 0.0086 wt. % to 0.0012 wt. % (Figure 7.5 (d)), it was shown that the intensity increased up to the high level of Ti content, which was different result from previous one. Although detail thermodynamic analysis was not carried out in this work, it is not difficult to presume from Figure 7.5 that high Ti content increase amount of TiS during reheating and weight percent of $Ti_4C_2S_2$ and TiC will also be increased but they would not have chance to be transformed into FeTiP due to the low level of P content.

## 7.4 Summary

An artificial neural network has been used to investigate the effect of complex thermo-mechanical processing parameters on the γ-fibre texture after recrystallization. The model used input data in form of chemical composition, cold rolling reduction, recrystallization temperature and texture intensities. The output of this model was represented in terms of texture intensities. Especially the investigation has been focused on texture changes according to the cold rolling reduction as well as Mn, P and Ti contents known to mostly affect to {111} recrystallization texture. From the calculation results we could confirm that high cold rolling reduction rate and low Mn as well as P contents appears to improve the γ-fibre texture after recrystallization. Moreover, it was shown that Ti content change

have differently influence on the texture according to the P contents. In high P content region, high level of Ti was harmful for development of the γ-fibre texture but texture intensity was increased as Ti content increase in low P content region.

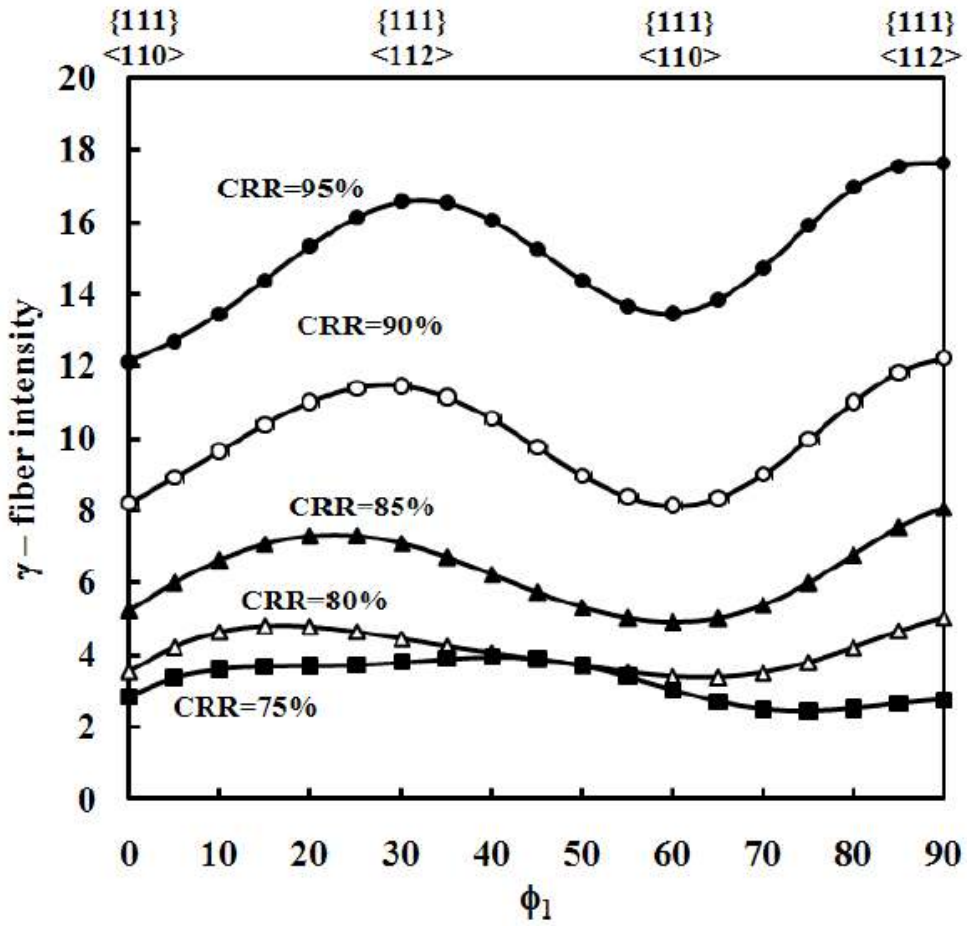


Figure 7.2 Calculated -fibre texture intensity according to various cold rolling reduction rate from 75%-95%. The fundamental condition for chemical composition and annealing temperature was assumed to be same as [121]

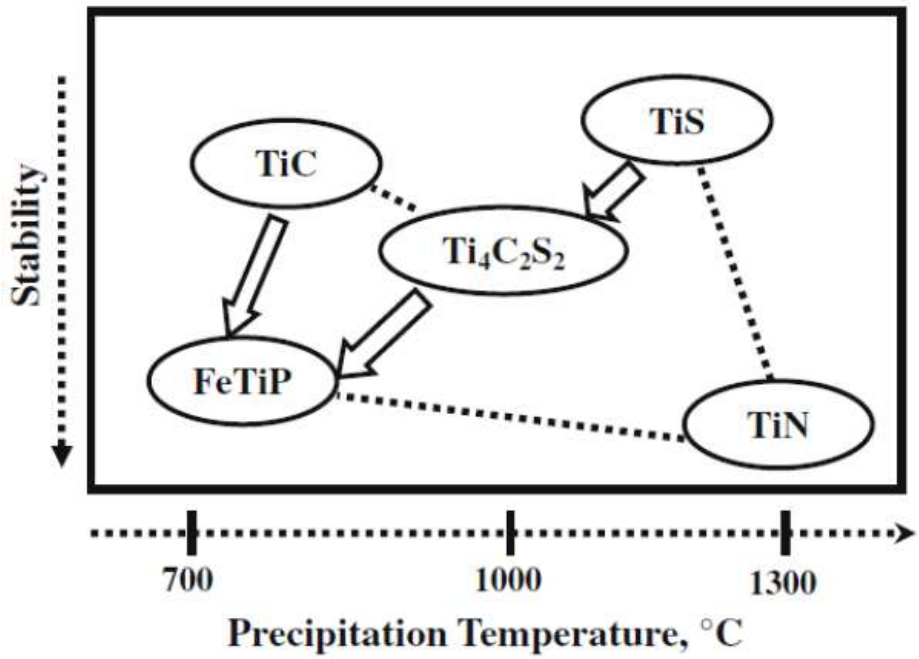


Figure 7.3 Schematic illustration of stability of various Ti precipitations according to the temperature [108]

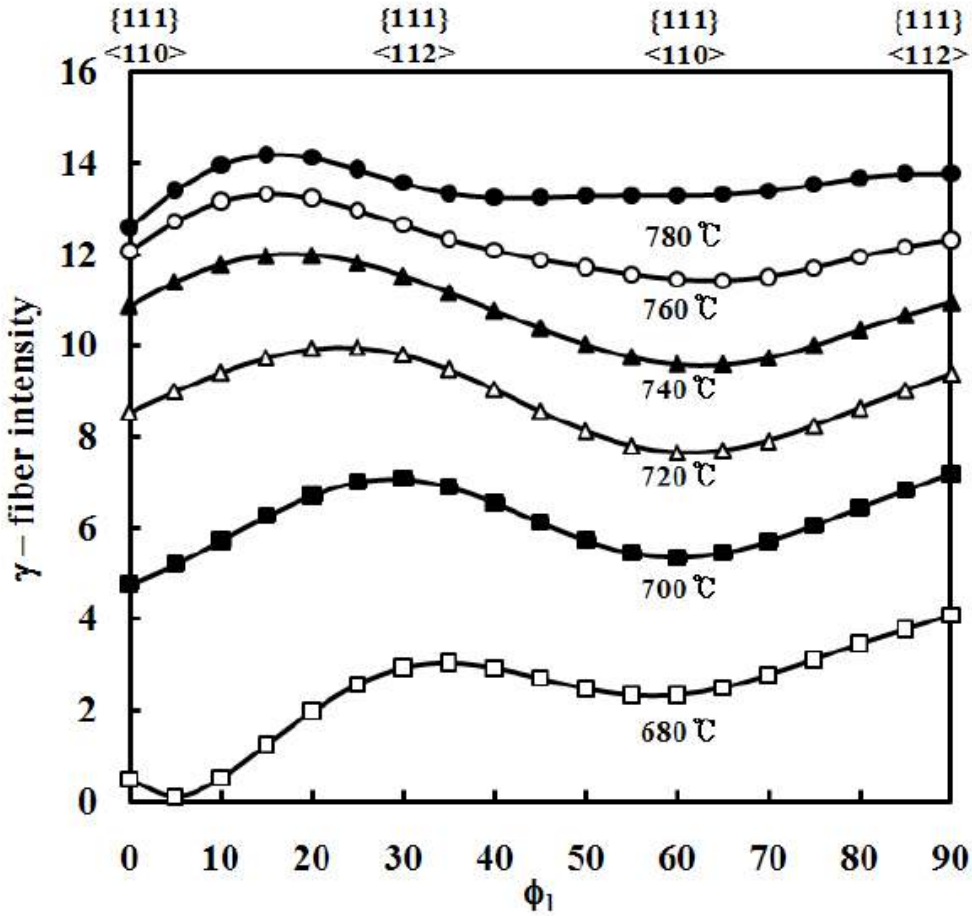


Figure 7.4 The calculated γ-fibre texture intensity according to recrystallization temperature. The fundamental condition for chemical composition and cold rolling reduction was assumed to be same as [33]

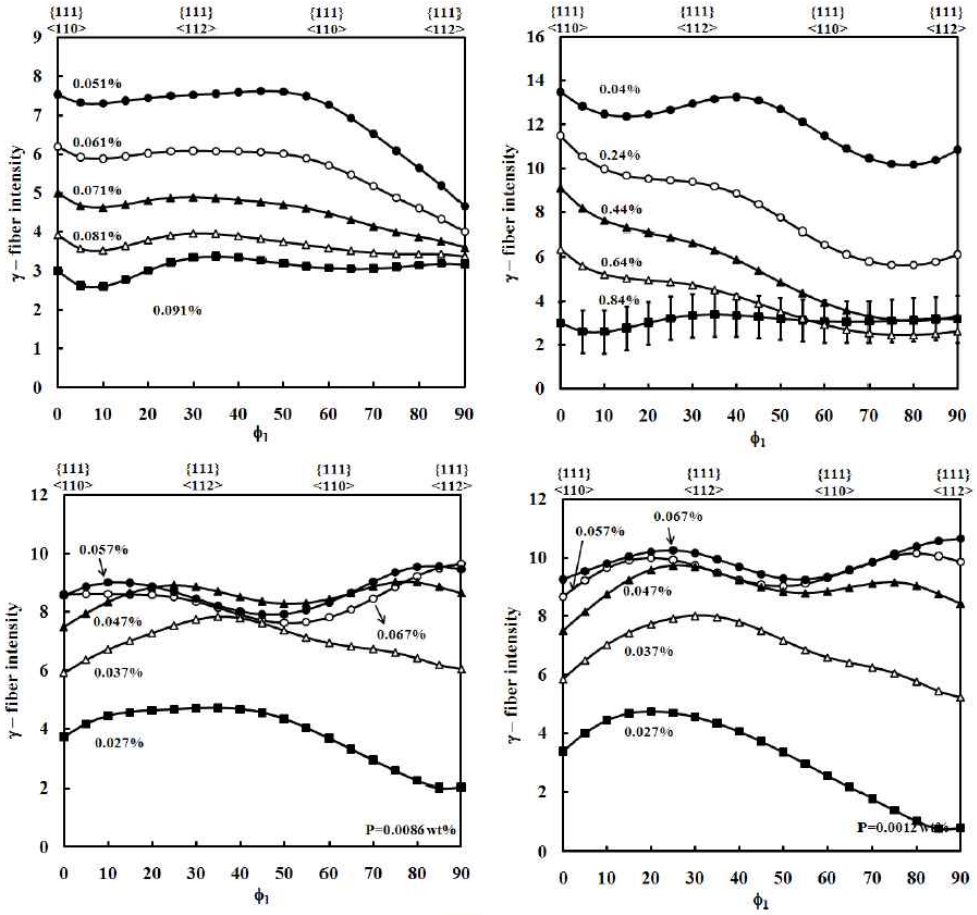


Figure 7.5 Calculated -fibre texture intensity according to P content (a), Mn content (b), Ti content with 0.086 wt. % P (c) and Ti content with 0.0012 wt. % P (d). The fundamental condition for cold rolling reduction as well as annealing temperature was assumed to be same as

# Chapter 8 Conclusions

In the case of displacive transformations, the set consisting of the orientation relationship, shape deformation and habit plane is uniquely connected by the phenomenological theory of martensite; crystallographic texture including variant selection can therefore be estimated theoretically as a function of an externally imposed system of stresses. Although efforts has been also made to demonstrate the effect of external stresses or strains the orientation of allotriomorphic ferrite during diffusional transformation, there is no direct influence perceived due to the easy relaxation of strain energy. Nonetheless, some variant selection has been observed resulting from the so-called 'dual orientation', and factors which make nucleation easier.

Favoured variants of ferrite are those which achieve simultaneous lattice matching with two or more adjacent austenite grains. To predict the theoretical possibility of such dual orientations at grain faces, edges and corners, calculations has been performed to reveal sensitivity to the parameters $\theta$ and $\Delta_{max}$ which indicate right-handed rotation angle and tolerance angle for rational orientations. The probability of this happening by pure chance has been forward to be small, even in strongly textured austenite.

However, it is discovered that the chance of observing dual orientations is significant when ferrite nucleates at certain coincidence site lattice boundaries of austenite. This novel result has also been verified by electron back scattered

diffraction (EBSD) experiments where $\sum = 3$ or $\sum = 11$ boundaries are form to be particularly favorable.

The interfacial energy for the nucleation of ferrite could be decreased by reducing inclination angle between a facetted interface that has a low energy, and the grain boundary plane of austenite. Thus, particular orientation relationships that happen to lead to a low inclination angle would be favoured. However, this criterion leads to difficulties in describing variant selection of precipitates when the inclination is large than a critical value, $\theta_c$ especially when ferrite evolves from deformed austenite grains.

To deal with this difficulty, a model has been developed by considering the hard impingement during ferrite grain growth. From several experimental results and simulations, it has been confirmed that the orientation of ferrite is affected by mainly three by reasons: the orientation of boundary plane relative to adjacent austenite grains, the deformation of austenite prior to ferrite formation and the interface characteristics of boundary. Without deformation of austenite prior to the ferrite transformation, the orientation of the grain boundary plane has a major influence on at of the ferrite. It has been observed that ferrite has an orientation relationship with austenite such that the $\{111\}_\gamma$ plane is aligned as parallel as possible to the grain boundary plane. This follows the suggestion of previous studies on variant selection of grain boundary ferrite. It is suggested that the orientation of ferrite is influenced by that of the grain boundary plane when the difference in stored energy of adjacent austenite grains is negligible. When this is

not the case, the criterion dominates in growth selection.

A pattern recognition approach has been also performed using an artificial neural network to investigate the effect of complex thermo-mechanical processing parameters on the ferrite texture in interstitial-free steels, with a focus on the technologically important γ-fibre texture. It approaches that the texture intensity is sensitive to the cold rolling reduction and concentration of alloying components such as Mn, P and Ti.

# Appendix A Texture Development during Reverse Transformation

## A.1 Introduction

Transformation induced plasticity (TRIP) steels are known for their combination of strength and formability and therefore, are used in the automotive industry to contract safe and efficient. [122-124]. These properties of steels have been improved by grain refining, especially in low-carbon TRIP steel [125, 126]. One important step of thermal treatment in this grain refining process is the intercritical annealing which converts the initial martensitic microstructure of cold rolled materials into martensite, retained austenite and recrystallized martensite phases. Since the properties are controlled by the phase fractions, texture and morphologies, it is necessary to understand the recovery, recrystallization and phase transformation stages. It is established that these properties are determined by competition between recovery and recrystallization as well as recrystallization and phase transformation [127, 128], is determined by parameters such as heating rate, intercritical annealing temperature, annealing time, cooling rate and annealing temperature etc. [129-131]. Although many microscopic analysis have been performed as a function of these experimental parameters [127, 128], texture evolutions is not understood. Thus, we have tried to illuminate the transformation texture development during reverse transformation in this work.

## A.2 Experimental procedures

Fe-0.12C-5.8Mn-0.47Si-3.1Al wt. % low carbon manganese TRIP steel has been used in this experiment. The details of alloy preparation has been presented in report by Suh et al. [125]. After cold-rolling, specimen was heated to 780 ℃ for 2 min and a volume fraction of retained austenite of 0.3 was obtained upon cooling to ambient temperature with 10℃/s. Samples were polished using the standard specimen preparation to the colloidal silica for 3min. Crystallographic orientations of phases were measured using electron back scattered diffraction (EBSD) on a ZEISS SUPRA$^{TM}$ scanning electron microscope. Step size for orientation mapping was 0.05$\mu$m.

## A.3 Results and discussions

Figure A.1 (a) is an image quality map of scanned area and (b) the orientation map. Since the hot-rolled structure is a mixture of elongated ferrite and martensite, coarse ferrite stretched in the rolling direction (RD) is assumed to be fully recrystallized δ-ferrite and other phases to be mixture of un-recrystallized martensite, recrystallized martensite and austenite. To confirm each phases from the scanned area, phase map with grain orientation spread map was illustrated in Figure A.1 (c). In general, it is impossible to separate ferrite from martensite in a phase map due to their same crystal structure.

**(a)**

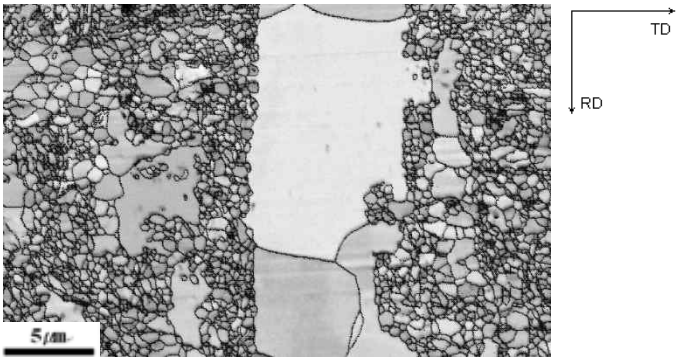


**(b)**

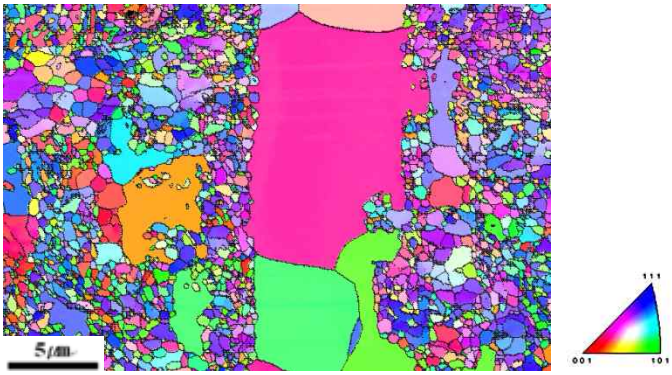


**(c)**

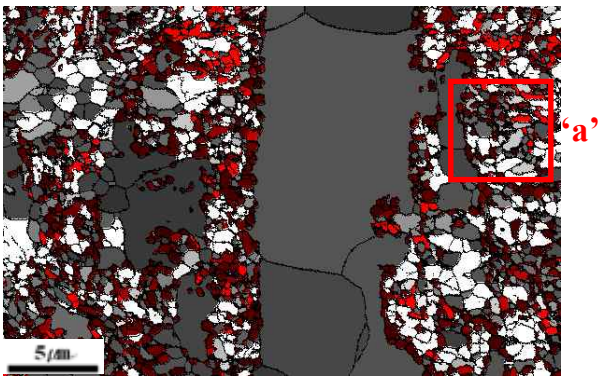


Figure A.1 (a) Image quality map of scanned area (b) orientation map (c) phase map with grain average misorientation map. Red color corresponds to the austenite and white color to martensite or recrystallized phase from martensite. Grains which have grain orientation spread (GS) value less than 1.5 were illustrated by gray scale.

However, several methods such as Kernel average misorientation (KAM) map [132-135], grain orientation spread (GS) map [127] and image quality (IQ) map [135-139] etc can be used for this purpose. Grains which have GS value less than 1.5(× randomly distributed intensity) are expressed in gray scale in (c) and it can be seen clearly that austenite transformation occurred not at the unrecrystallised α'/ unrecrystallised α' boundaries but mostly at boundaries between unrecrystallised α'/ recrystallized α'. This means that austenite transformed after the recrystallization of martensite during intercritical annealing and a magnified image of section **'a'** in Figure A.1 (c) demonstrates the location of austenite grains. To know the orientation relationship between austenite and martensite or recrystallized martensite in Figure A.2, a total of 20 grains was observed and their deviation from the exact Kurdjumov-Sachs relationship listed in Table A.1. Most austenite grains had a low energy orientation relationship with both adjacent martensite and recrystallized martensite, i.e., a dual orientation relationship. Since simultaneous lattice matching in this way leads to strong variant selection during diffusional transformation [17, 18], it is assumed that the austenite variants with this would be selected from 24 possible variants.

Figure A.3 shows (100), (110) and (111) pole figures of martensite, recrystallized martensite and austnite grains. Based on variant information, $(110)_{\gamma}$ and $(111)_{\gamma}$ austenite texture were calculated using all possible KS variants and Figure A.4 (b) shows the results. This is not consistent with experimental data of austenite in Figure A.4 (a) indicating favoured variants. Figure A.4 (c) are calculated $(110)_{\gamma}$ and

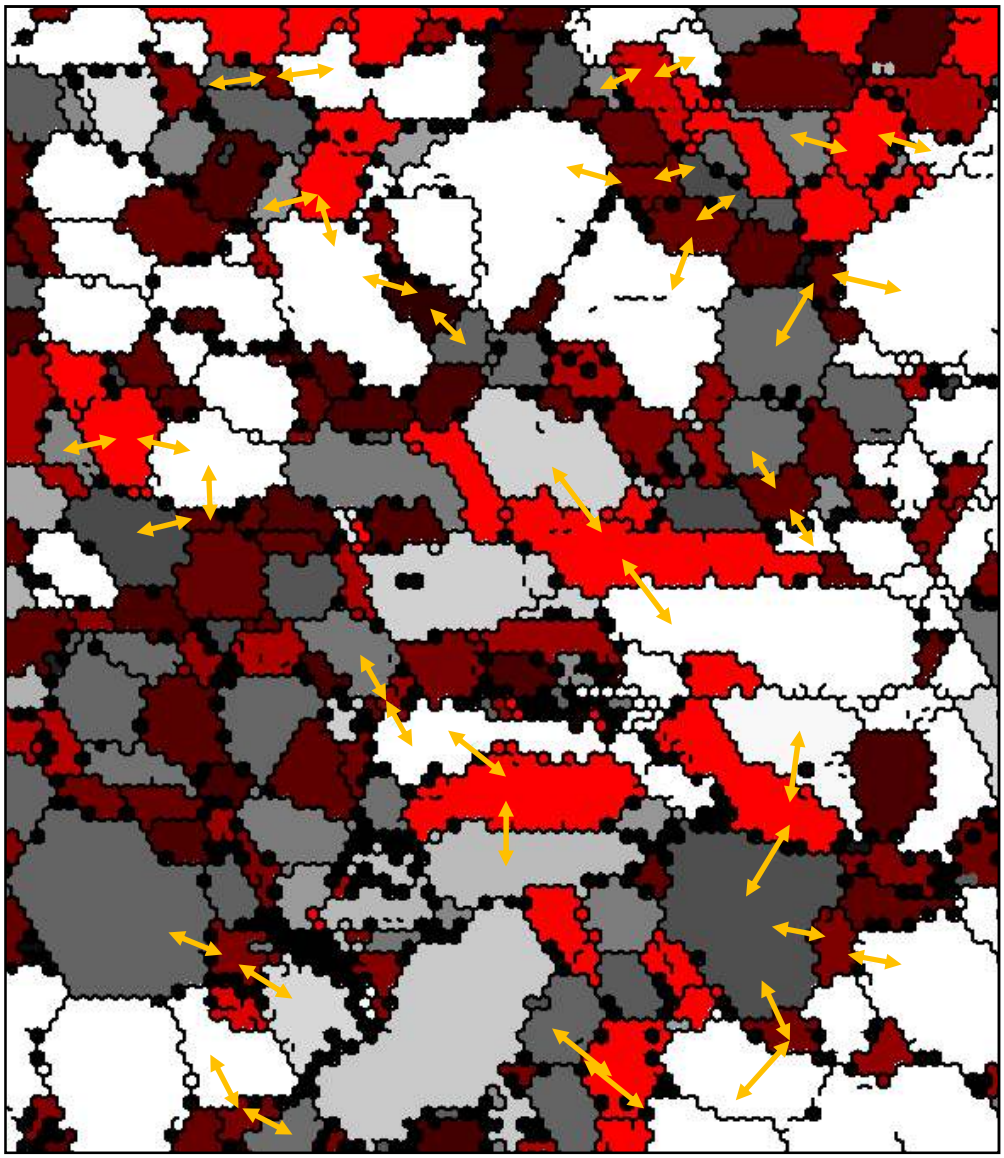

Figure A.2 a magnified image of section **'a'** marked in Figure A.1 (c) The orientation relationship with austenite and martensite or recrystallized martensite were marked in arrow. Red corresponds to the austenite and white and gray to martensite and recrystallized martensite respectively.

Table A.1 Deviation from the exact Kurdjumov-Sachs orientation for the austenite grains in Figure A.2

| γ grains | Deviation axis - angle pairs from exact KS orientation relationship | |
|---|---|---|
| | With respect to martensite | With respect to recrystallized martensite |
| $\gamma_1$ | [0.32 0.25 -0.91] 7.0° | [-0.01 -0.93 -0.38] [- 14.3° |
| $\gamma_2$ | [0.68 -0.27 0.68] 4.5° | 0.78 0.62 0.11] 4.0° |
| $\gamma_3$ | [0.74 0.65 0.19] 2.5° | [-0.49 -0.05 -0.87] [- 5.5° |
| $\gamma_4$ | [0.54 -0.71 -0.45] 1.3° | 0.29 -0.34 -0.89] 4.0° |
| $\gamma_5$ | [0.52 -0.34 -0.79] 4.0° | [-0.88 -0.47 -0.07] 10.4° |
| $\gamma_6$ | [0.02 0.96 -0.28] 3.4° | [0.58 0.78 -0.23] 3.8° |
| $\gamma_7$ | [0.19 -0.46 -0.87] 3.7° | [-0.12 0.87 0.48] 7.8° |
| $\gamma_8$ | [-0.78 -0.14 0.61] 4.9° | [0.99 -0.16 -0.01] 11.3° |
| $\gamma_9$ | [-0.07 1.00 0.01] 8.0° | [0.25 0.21 -0.95] 1.6° |
| $\gamma_{10}$ | [0.65 -0.05 -0.76] 2.6° | [0.82 -0.16 -0.55] 9.4° |
| $\gamma_{11}$ | [-0.03 -0.77 0.63] 6.6° | [-0.75 -0.66 0.01] 6.2° |
| $\gamma_{12}$ | [-0.88 -0.13 0.47] 2.6° | [0.14 -0.45 0.88] 4.7° |
| $\gamma_{13}$ | [0.20 -0.80 0.57] 5.0° | [-0.05 0.91 0.42] 5.1° |
| $\gamma_{14}$ | [-0.66 -0.25 0.71] 1.5° | [-0.57 0.29 -0.77] 4.6° |
| $\gamma_{15}$ | [-0.03 -0.77 0.63] 6.6° | [-0.75 -0.66 0.01] 6.2° |
| $\gamma_{16}$ | [0.08 -0.80 -0.60] 3.4° | [-0.98 0.10 -0.15] 5.5° |
| $\gamma_{17}$ | [0.68 -0.72 -0.09] 1.1° | [-0.95 0.02 0.32] 15.2 ° |
| $\gamma_{18}$ | [-0.91 0.34 -0.23] 8.2° | [-0.39 0.67 0.63] 4.2° |
| $\gamma_{19}$ | [0.18 0.16 -0.97] 3.8° | [0.87 -0.48 -0.15] 5.8° |
| $\gamma_{20}$ | [0.77 -0.63 0.05] 4.2° | [0.19 0.12 -0.98] 1.1° |

$(111)_\gamma$ pole figures of austenite with variant selection. Although some austenite transformed at boundaries between martensite or recrystallized martensite grains, selection by dual orientation shows good agreement with results in (a) in terms of texture intensity and positions of variants.

## A.4 Conclusions

No standing of kinetics competition between recrystallization and transformation mechanisms during reverse transformation has been studied in Fe-0.12C-5.8Mn-0.47Si-3.1Al wt. % low carbon manganese TRIP steels using macroscopic texture analysis. Austenite has been observed to have a low energy orientation relationship simultaneously with adjacent martensite and recrystallized martensite grain, which means that most transformation from martensite to austenite occurred after the recrystallization of martensite in this alloy system. The calculated pole figure with variants selection are consistent with those observed experimentally observed pole figure of austenite showed the evidence of variants restriction due to the simultaneous lattice matching by dual orientation.

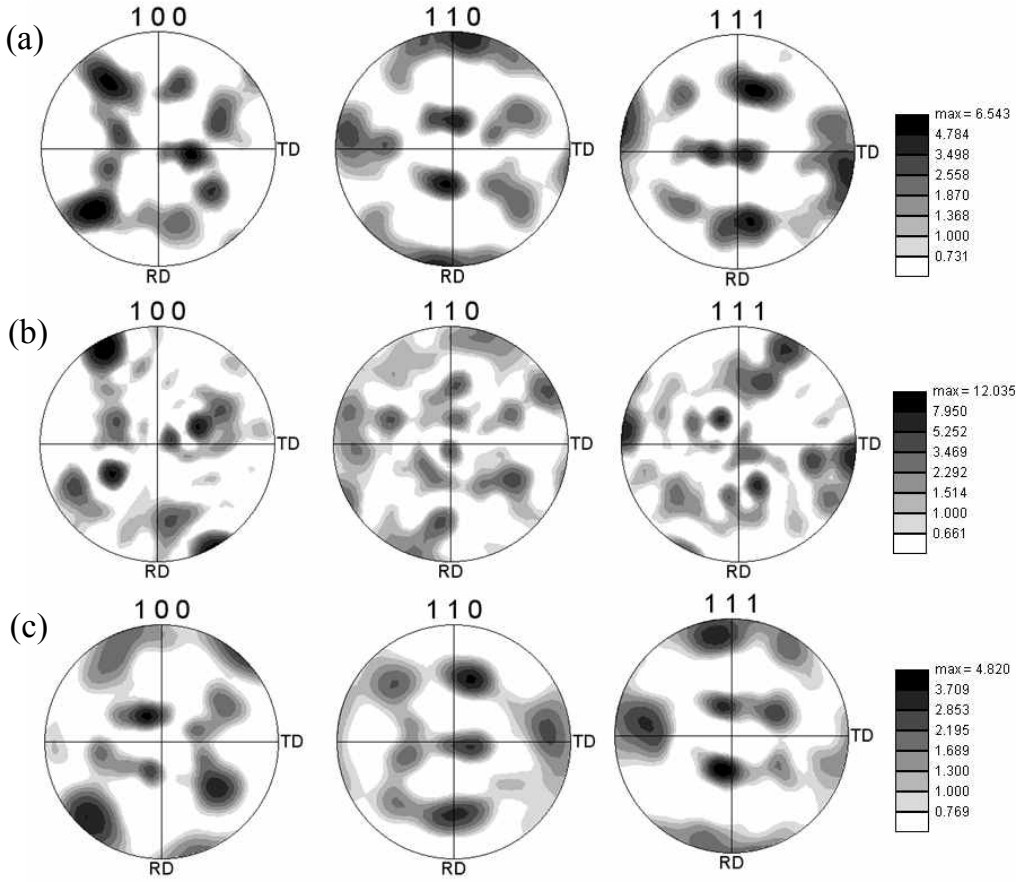


Figure A.3 {100}, {110} and {111} pole figures of (a) un-recrystallized martensite (b) recrystallized martensite, (c) austenite grains

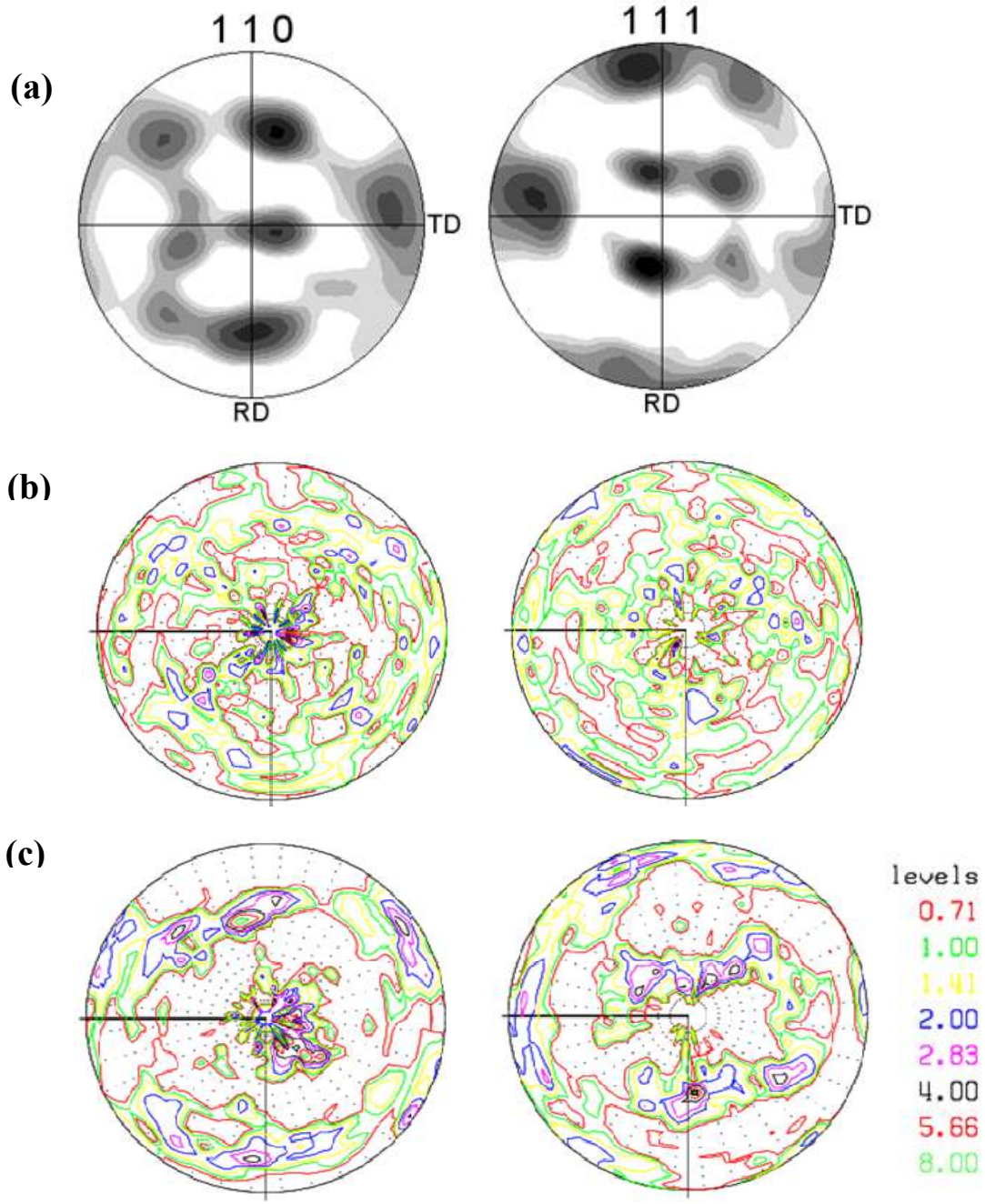


Fig.5 110 and 111-Pole figures of austenite (a) Experimental data, (b) calculated data with all possible KS variants (c) and with favoured variants.

# Appendix B FORTRAN program

These programs can be obtained from
http://www.msm.cam.ac.uk/map/mapmain.html

**Program MAP_STEEL_FERRITE_TEXTURE**

**1. Provenance of Source Code**

Kim Dae Woo

Graduate Institute of Ferrous Technology (GIFT)

Pohang University of Science and Technology

Pohang, Republic of Korea

gomdury@postech.ac.kr

Added to MAP: September 2008.

**2. Purpose of code**

The allotriomorphic ferrite nucleates heterogeneously at austenite grain boundaries, and although a reproducible, low-energy orientation relationship is expected to exist between the ferrite and one of the austenite grains with which it is in contact, there are reports that the ferrite can simultaneously adopt this orientation with more than one austenite grain. We examine this possibility using crystallographic theory in order to assess the probability of such events as a function of the strength of the

texture within the austenite prior to its transformation.

**3. Specification**

Language: Fortran 77

Product form: Source code and executable files for UNIX/Linux machines.

**4. Description**

Austenite grains are conveniently represented as a stack of identical, space-filling Kelvin tetrakaidecahedra each of which consists of eight hexagonal and six square faces, with 36 equal edges. For ferrite nucleation at austenite grain surfaces, there are therefore 14 face-sites per grain. The computer algorithm was constructed so that for each grain orientation relative to the sample frame of reference, it was possible to access the orientations of the fourteen neighbouring grains. A total of 1700 austenite grains were created in this way, with one of the grains having its crystallographic axes exactly parallel to those of the sample. The relationship between the sample and austenite crystal axes can be described using Euler angles. These are the three angles by which the sample reference frame must be rotated in order to coincide with that of the crystal. None random austenite textures were generated relative to the sample axes by setting the first austenite grain to the exact required texture, and then choosing relative to this grain, random rotation axes but with the right-handed rotation angle limited to the range of 4 to 45 degree. Any grain of ferrite will always have an orientation relationship ($\alpha$ J $\gamma$) with an austenite

grain 1. However, some ferrite grains will have a special orientation relationship which corresponds to a low energy configuration. We adopt as the low energy orientation, one predicted by the crystallographic theory of martensite in order to ensure a coherent line between $\alpha$ and $\gamma$:

$$\begin{pmatrix} 0.579356 & 0.542586 & 0.102537 \\ 0.014470 & 0.133650 & -0.788984 \\ -0.552000 & 0.0572979 & 0.086936 \end{pmatrix}$$

and when ferrite was allowed to form on a face between two austenite grains with relative orientation ($\gamma_1$ J $\gamma_1$), the corresponding orientations with the ferrite are ($\gamma_1$ J $\alpha$) and ($\gamma_2$ $J_{LE}$ $\alpha$) where the latter is the low energy variant. It follows that:

$$(\gamma_1 \text{ J } \alpha) = (\gamma_1 \text{ J } \gamma_1)\ (\gamma_2\ J_{LE}\ \alpha)$$

Both the matrices on the right-hand side of this equation are known because the austenite orientations are set initially and (r 2_JLE_a) is given by previous table. Ferrite was allowed to nucleate on all 14 faces of each austenite grain. The ferrite in all cases had a low energy orientation with one austenite grain; since there are 24 crystallographically equivalent such orientations for any given austenite grain, the selection of the particular variant was made at random from the 24 available. The name of source code is

**allotriomorh.f**

This is a source code of this program. For the execution, it needs to be compiled.

compile example : g77 allotriomorp.f -o name.out

## 5. References


1. Transformation texture of allotriomorphic ferrite in steel, Materials Science and Technology, 2009, DOI: 10.1179/174328408X365793, D. W. Kim, R. S. Qin, H. K. D. H. Bhadeshia
2. Crystallographic Texture of Stress-Affected Bainite, Proceedings of The Royal Society A, 463 (2007) 2309-2328, S. Kundu, K. Hase and H. K. D. H. Bhadeshia
3. S. Kundu, Transformation Strain and Crystallographic Texture in Steels, Ph.D. Thesis, University of Cambridge, U. K., 2007.
4. H. K. D. H. Bhadeshia, Geometry of Crystals. 2nd edition, Institute of Materials, 2001

## References


1. Mackenzie, J.K. and J.S. Bowles, *The crystallography of martensite transformations II.* Acta Metallurgica, 1954. **2**(1): p. 138-147.
2. Bowles, J.S. and J.K. Mackenzie, *The crystallography of martensite transformations I.* Acta Metallurgica, 1954. **2**(1): p. 129-137.
3. Wechsler, M.S., D.S. Lieberman, and T.A. Read, *On the theory of the formation of martensite.* Trans. AIME Journal of Metals, 1953. **197**: p. 1503-1515.
4. Kundu, S. and H.K.D.H. Bhadeshia, *Transformation texture in deformed stainless steel.* Scripta Materialia, 2006. **55**(9): p. 779-781.
5. Kato, M. and T. Mori, *Stress-induced martensite in single crystals of an Fe-23Ni-5Cr alloy.* Acta Metallurgica, 1976. **24**(9): p. 853-860.
6. Higo, Y., F. Lecroisey, and T. Mori, *Relation between applied stress and orientation relationship of α´ martensite in stainless steel single crystals.* Acta Metallurgica, 1974. **22**(3): p. 313-323.
7. Bokros, J.C. and E.R. Parker, *The mechanism of the martensite burst transformation in FeNi single crystals.* Acta Metallurgica, 1963. **11**(12): p. 1291-1301.
8. Bogers, A.J. and W.G. Burgers, *Partial dislocations on the {110} planes in the B.C.C. lattice and the transition of the F.C.C. into the B.C.C. lattice.* Acta Metallurgica, 1964. **12**(2): p. 255-261.
9. Patel, J.R. and M. Cohen, *Criterion for the action of applied stress in the*

*martensitic transformation.* Acta Metallurgica, 1953. **1**(5): p. 531-538.

10. Perdahcioğlu, E.S., H.J.M. Geijselaers, and M. Groen, *Influence of plastic strain on deformation-induced martensitic transformations.* Scripta Materialia, 2008. **58**(11): p. 947-950.

11. Geijselaers, H.J.M. and E.S. Perdahcioğlu, *Mechanically induced martensitic transformation as a stress-driven process.* Scripta Materialia, 2009. **60**(1): p. 29-31.

12. Dames, G.J., J.S. Kallend, and P.P. Morris, *The quantitative prediction of transformation textures.* Acta Metallurgica, 1976. **24**(2): p. 159-172.

13. Kurdjumov, G.V. and G. Sachs, *Über den mechanismus der stählhartung.* Zietschrift für Physik A Hadrons and Nuclei, 1930. **64**: p. 325-343.

14. Nishiyama, Z., *X-ray investigation of the mechanism of the transformation from face centered cubic lattice to body centered cubic.* Science Reports of Tohoku Imperial University, 1934. **23**: p. 637–634.

15. Lee, J.K. and H.I. Aaronson, *Influence of faceting upon the equilibrium shape of nuclei at grain boundaries--II. Three-dimensions.* Acta Metallurgica, 1975. **23**(7): p. 809-820.

16. Lee, J.K. and H.I. Aaronson, *Influence of faceting upon the equilibrium shape of nuclei at grain boundaries--I. Two-dimensions.* Acta Metallurgica, 1975. **23**(7): p. 799-808.

17. Kim, D.W., et al., *Dual orientation and variant selection during diffusional transformation of austenite to allotriomorphic ferrite.* Journal of Materials

Science, 2010. **45**(15): p. 4126-4132.

18. Kim, D.W., R.S. Qin, and H.K.D.H. Bhadeshia, *Transformation texture of allotriomorphic ferrite in steel.* Materials Science and Technology, 2009. **25**(7): p. 892-895.

19. Bhadeshia, H.K.D.H., *Diffusional formation of ferrite in iron and its alloys.* Progress in Materials Science, 1985. **29**(4): p. 321-386.

20. Chan, J.W. and G. Kalonji. in *International Conference on Solid-Solid Transformations*. 1981. Warrendale, Pennsylvania: TMS-AIME.

21. Cahn, J.W., *Theory of crystal growth and interface motion in crystalline materials.* Acta Metallurgica, 1960. **8**(8): p. 554-562.

22. Hillert, M., *The Mechanism of Phase Transformation in Crystalline Solids*. 1969: Institute of Metals, London.

23. Clemm, P.J. and J.C. Fisher, *The influence of grain boundaries on the nucleation of secondary phases.* Acta Metallurgica, 1955. **3**: p. 70–73.

24. Cahn, J.W., *The Kinetics of grain boundary nucleated reactions.* Acta Metallurgica, 1956. **4**: p. 449–564.

25. Reed, R.C. and H.K.D.H. Bhadeshia, *The Reconstructive Austenite-Ferrite Transformation in Low-Alloy Steels.* Materials Science and Technology, 1992. **8**: p. 421-435.

26. Ryder, P.L., W. Pitsch, and R.F. Mehl, *Crystallography of the precipitation of ferrite on austenite grain boundaries in a Co + 20% Fe alloy.* Acta Metallurgica, 1967. **15**(9): p. 1431-1440.

27. Ryder, P.L. and W. Pitsch, *The crystallographic analysis of grain-boundary precipitation.* Acta Metallurgica, 1966. **14**(11): p. 1437-1448.

28. King, A.D. and T. Bell, *Observations on the morphology and crystallography of proeutectoid ferrite.* Metallography, 1976. **9**(5): p. 397-413.

29. Christian, J.W., *The Theory of Phase Transformations in Metals and Alloys, Part 1, 2nd edition*. 1965: Pergamon, Oxford.

30. Babu, S.S. and H.K.D.H. Bhadeshia, *A direct study of grain boundary allotriomorphic ferrite crystallography.* Materials Science and Engineering: A, 1991. **142**(2): p. 209-219.

31. Crosky, A., P.G. McDougall, and J.S. Bowles, *The crystallography of the precipitation of $\alpha$ rods from $\beta$ Cu-Zn alloys.* Acta Metallurgica, 1980. **28**(11): p. 1495-1504.

32. Purdy, G.R., *The dynamics of transformation interfaces in steels--I. The ferrite-austenite interface in Fe-C-Mo alloys.* Acta Metallurgica, 1978. **26**(3): p. 477-486.

33. Ghosh, P., et al., *Precipitation behavior and texture formation at different stages of processing in an interstitial free high strength steel.* Scripta Materialia, 2008. **59**(3): p. 276-278.

34. Tanaka, T., *Controlled Rolling of Steel Plate and Strip.* International metals reviews, 1981. **26**(4): p. 185-212.

35. Bowles, J.S. and J.K. Mackenzie, *The crystallography of martensite*

*transformations III. Face-centred cubic to body-centred tetragonal transformations.* Acta Metallurgica, 1954. **2**(2): p. 224-234.

36. Bunge, H.-J., *Texture Analysis in materials Science: Mathematical Methods*. 1982: Butterworths-Heinemann, London.

37. Randle, V. and O. Engler, *Introduction to texture analysis : macrotexture, microtexture and orientation mapping*. 2000: Amsterdam, The Netherlands

38. Lee, D.N., *Texture and Related Phenomena*. 2006: The Korean Institute of Metals and Materials, Seoul.

39. Bhadeshia, H.K.D.H., *Problemisn theG alculatioonf T ransformatiToenx turein Steels.* lSlJ lnternat ional, 2010. **50**(11): p. 1517-1522.

40. Bhadeshia, H.K.D.H., *Geometry of crystals, 2nd edition*. 2001: Institute of Materials, London.

41. Miyamoto, G., et al., *Crystallography of intragranular ferrite formed on (MnS+V(C,N)) complex precipitate in austenite.* Scripta Materialia, 2003. **48**(4): p. 371-377.

42. Kang, J.H., et al., *Effect of external stress on the orientation distribution of ferrite.* Scripta Materialia, 2003. **48**(1): p. 91-95.

43. Dahmen, U., P. Ferguson, and K.H. Westmacott, *Invariant line strain and needle-precipitate growth directions in Fe-Cu.* Acta Metallurgica, 1984. **32**(5): p. 803-810.

44. Gey, N., B. Petit, and M. Humbert, *Electron backscattered diffraction study of ε/a´ martensitic variants induced by plastic deformation in 304 stainless*

*steel.* Metallurgical and Materials Transactions A: Physical Metallurgy and Materials Science, 2005. **36**(12): p. 3291-3299.

45. Bokros, J.C. and E.R. Parker, *The mechanism of the martensite burst transformation in Fe---Ni single crystals.* Acta Metallurgica, 1963. **11**(12): p. 1291-1301.

46. Durlu, T.N. and J.W. Christian, *Effect of prior deformation on the martensite burst transformation in single crystals of an Fe-Ni-C alloy.* Acta Metallurgica, 1979. **27**(4): p. 663-666.

47. Davies, G.J. and R.M. Bateman. in *6th International Conference on Textures of Materials*. 1981. Tokyo: The Iron and Steel Institute of Japan.

48. Higo, Y., F. Lecroisey, and T. Mori, *Relation between applied stress and orientation relationship of a′martensite in stainless steel single crystals.* Acta Metallurgica, 1974. **22**(3): p. 313-323.

49. Kato, M. and T. Mori, *Orientation of martensite formed in Fe-23Ni-5Cr crystals under uniaxial stress along [001].* Acta Metallurgica, 1977. **25**(8): p. 951-956.

50. Miyaji, H., et al. in *Physical metallurgy of thermomechanical processing of steels and other metals*. 1988.

51. Adachi, Y., K. Hakata, and K. Tsuzaki, *Crystallographic analysis of grain boundary Bcc-precipitates in a Ni-Cr alloy by FESEM/EBSD and TEM/Kikuchi line methods.* Materials Science and Engineering: A, 2005. **412**(1-2): p. 252-263.

52. Kei, A., et al., *Morphology of proeutectoid ferrite at austenite grain boundaries in low carbon.* Tetsu-To-Hagane, Journal of the Iron and Steel Institute of Japan, 1988. **74**: p. 1839-1845.

53. Vaughan, D., *The precipitation of θ′ at high-angle boundaries in an Al-Cu alloy.* Acta Metallurgica, 1970. **18**(1): p. 183-187.

54. Furuhara, T., et al., *Crystallography of grain boundary alpha precipitates in beta titanium alloy.* Metallurgical and Materials Transactions A, 1996. **27**: p. 1635-1646.

55. Dingley, D.J. and M.M. Nowell, *The use of electron backscatter diffraction for the investigation of nano crystalline materials and the move towards orientation imaging in the TEM.* Microchimica Acta, 2004. **147**: p. 157–165.

56. Humphreys, F.J., *Characterisation of fine-scale microstructures by electron backscatter diffraction (EBSD).* Scripta Materialia, 2004. **51**: p. 771–776.

57. Gourgues-Lorenzon, A.F., *Application of electron backscatter diffraction to the study of phase transformations.* International Materials Reviews, 2007. **52**: p. 65-128.

58. Gourgues, A.F., H.M. Flower, and T.C. Lindley, *Electron backscatterring diffraction study of acicular ferrite, bainite and martensite steel microstructures.* Materials Science and Technology, 2000. **16**: p. 26–40.

59. Gourgues, A.-F., *Electron backscatter diffraction and cracking.* Materials Science and Technology, 2002. **18**: p. 119-133.

60. Nohava, J., et al., *Electron backscattering diffraction analysis of secondary*

*cleavage cracks in a reactor pressure vessel steel.* Materials Characterisation, 2003. **49**: p. 211–217.

61. Lambert-Perlade, A., et al., *Mechanisms and modelling of cleavage fractures in simulated heat–affected zone microstructures in HSLA steel.* Metallurgical & Materials Transactions A, 2004. **35A**: p. 1039–1053.

62. Kim, Y.M., et al., *Effects of molybdenum and vanadium addition on tensile and charpy impact properties of API X70 linepipe steels.* Metallurgical & Materials Transactions A, 2007. **38A**: p. 1731–1742.

63. Callone, V., A.F. Gourgues, and A. Pineau, *Fatigue crack propagation in cast duplex stainless steels: thermal ageing and microstructural effects.* Fatigue and Fracture of Engineering Materials and Structures, 2004. **27**: p. 31-43.

64. S.Wechsler, M., D.S. Lieberman, and T.A. Read., *On the theory of the formation of martensite.* AIME Journal of Metals, 1953. **197**: p. 1503-1515.

65. Kundu, S. and H.K.D.H. Bhadeshia, *Crystallographic texture and intervening transformations.* Scripta Materialia, 2007. **57**: p. 869–872.

66. Kundu, S., K. Hase, and H.K.D.H. Bhadeshia, *Crystallographic texture of stress–affected bainite.* Proceedings of the Royal Society A, 2007. **463**: p. 2309-2328.

67. Kundu, S., *Transformation Strain and Crystallographic Texture in Steels*. 2007, University of Cambridge: Cambridge, U. K.

68. Aaronson, H.I., *The proeutectoid ferrite and the proeutectoid cementite*

*reactions*. Decomposition of austenite by diffusional processes, ed. I.V. F.Zackay and H.I. Aaronson. 1962, New York, USA.

69. King, A.D. and T. Bell, *Crystallography of grain boundary proeutectoid ferrite.* Metallurgical Transactions A, 1975. **6A**: p. 1419-1429.

70. Suh, D.-W., et al., *Evaluation of the deviation angle of ferrite from the KS relationship in low carbon steel by EBSD.* Scripta Materialia, 2002. **46**: p. 375-378.

71. Underwood, E.E., *Quantitative Stereology*. 1970: Addison–Wesley Publication Company.

72. Czinege, I. and T. Reti, *Determination of local deformation in cold formed products by a measurement of the geometric characteristics of the crystallites*, in *In Eighteenth International Machine Tool Design and Research Conference, Forming*. 1977. p. 159–163.

73. Leeuwen, Y.v., et al., *Effect of geometrical assumptions in modelling solid state kinetics.* Metallurgical & Materials Transactions A, 1998. **29**: p. 2925-2931.

74. Singh, S.B. and H.K.D.H. Bhadeshia, *Topology of grain deformation.* Materials Science and Technology, 1998. **15**: p. 832-834.

75. Q. Zhu, C.M.S. and H.K.D.H. Bhadeshia, *Quantitative metallography of deformed grains.* Materials Science and Technology, 2007. **23**: p. 757–766.

76. McDougall, J.D.W.a.P.G., *The crystallography of Widmanstätten ferrite.* Acta Metallurgica, 1973. **21**: p. 961-973.

77. Bhadeshia, H.K.D.H., *Critical assessment: Diffusion–controlled growth of ferrite plates in plain carbon steels.* Materials Science and Technology, 1985. **1**: p. 497-504.

78. Hillert, M., *The formation of pearlite*. Decomposition of austenite by diffusional processes, ed. V.F. Zackay and H. I. Aaronson. 1962.

79. Swallow, E. and H.K.D.H. Bhadeshia, *High Resolution Observations of the Displacements Caused by Bainitic Transformation.* Materials Science and Technology, 1996. **12**: p. 121-125.

80. Watanabe, T., et al., *Grain boundary engineering by magnetic field application.* Scripta Materialia, 2006. **54**(6): p. 969-975.

81. Tsurekawa, S., et al., *The control of grain boundary segregation and segregation-induced brittleness in iron by the application of a magnetic field.* Journal of Materials Science, 2005. **40**(4): p. 895-901.

82. Bogers, A.J. and W.G. Burgers, *A.J Bogers and W.G Burgers. Partial dislocations on the {110} planes in the b.c.c. lattice and the transition of the fcc into the bcc lattice.* Acta Metallurgica, 1964. **55**: p. 779-781.

83. Wilkinson, A.J. and D.J. Dingley, *Quantitative deformation studies using electron back scatter patterns.* Acta Metallurgica et Materialia, 1991. **39**: p. 3047-3055.

84. Mukherjee, A.K., *Plastic Deformation of Metals Treaties on Materials Science and Technology*, ed. Arsennault. Vol. 6. 1975, New York: Academic Press.

85. Wilkinson, A.J. and D.J. Dingley, *Quantitative deformation studies using electron back scatter patterns.* Acta Metallurgica et Materialia, 1991. **39**(12): p. 3047-3055.

86. Choi, S.H., *Simulation of stored energy and orientation gradients in cold-rolled interstitial free steels.* Acta Materialia, 2003. **51**(6): p. 1775-1788.

87. Choi, S.-H. and Y.-S. Jin, *Evaluation of stored energy in cold-rolled steels from EBSD data.* Materials Science and Engineering A, 2004. **371**(1-2): p. 149-159.

88. Tóth, L.S. and J.J. Jonas, *Modelling the texture changes produced by dynamic recrystallization.* Scripta Metallurgica et Materialia, 1992. **27**(3): p. 359-363.

89. Urabe, T. and J.J. Jonas, *Modeling texture change during recrystallization of an IF steel.* ISIJ International, 1994. **34**(5): p. 435-442.

90. Juul Jensen, D., *Growth rates and misorientation relationships between growing nuclei/grains and the surrounding deformed matrix during recrystallization.* Acta Metallurgica et Materialia, 1995. **43**(11): p. 4117-4129.

91. Krielaart, G.P. and S. van der Zwaag, *Simulations of pro-eutectoid ferrite formation using a mixed control growth model.* Materials Science and Engineering A, 1998. **246**(1-2): p. 104-116.

92. Lee, K.-M., H.-C. Lee, and J.K. Lee, *Influence of coherency strain and applied stress upon diffusional ferrite nucleation in austenite.* Philosophical

Magazine, 2010. **90**: p. 437-459.

93. Lee, J.K., et al., *Plastic relaxation of the transformation strain energy of a misfitting spherical precipitate: Ideal plastic behavior.* Metallurgical Transactions A, 1980. **11**(11): p. 1837-1847.

94. Earmme, Y.Y., W.C. Johnson, and J.K. Lee, *Plastic Relaxation of the Transformation Strain Energy of a Misfitting Spherical Precipitation: Linear and Power-Law Strain Hardening.* Metallurgical transactions. A, Physical metallurgy and materials science, 1981. **12 A**(8): p. 1521-1530.

95. Santofimia, M.J., L. Zhao, and J. Sietsma, *Model for the interaction between interface migration and carbon diffusion during annealing of martensite-austenite microstructures in steels.* Scripta Materialia, 2008. **59**(2): p. 159-162.

96. Mecozzi, M.G., J. Sietsma, and S. van der Zwaag, *Analysis of $\gamma$ to $\alpha$ transformation in a Nb micro-alloyed C-Mn steel by phase field modelling.* Acta Materialia, 2006. **54**(5): p. 1431-1440.

97. Krielaart, G.P. and S. Van Der Zwaag, *Kinetics of $\gamma \rightarrow \gamma$ phase transformation in Fe-Mn alloys containing low manganese.* Materials Science and Technology, 1998. **14**(1): p. 10-18.

98. Santofimia, M.J., et al., *Influence of interface mobility on the evolution of austenite-martensite grain assemblies during annealing.* Acta Materialia, 2009. **57**(15): p. 4548-4557.

99. Liu, Z.K., *Theoretic calculation of ferrite growth in supersaturated*

*austenite in Fe---C alloy.* Acta Materialia, 1996. **44**(9): p. 3855-3867.

100. Kozeschnik, E., *A numerical model for evaluation of unconstrained and compositionally constrained thermodynamic equilibria.* Calphad, 2000. **24**(3): p. 245-252.

101. Ghosh, P., et al., *Precipitation and texture formation in two cold rolled and batch annealed interstitial-free high strength steels.* Scripta Materialia, 2006. **55**(3): p. 271-274.

102. Ghosh, P., B. Bhattacharya, and R.K. Ray, *Comparative study of precipitation behavior and texture formation in cold rolled-batch annealed and cold rolled-continuous annealed interstitial free high strength steels.* Scripta Materialia, 2007. **56**(8): p. 657-660.

103. Saha, R. and R.K. Ray, *Texture and grain growth characteristics in a boron added interstitial free steel after severe cold rolling and annealing.* Materials Science and Engineering: A, 2010. **527**(7-8): p. 1882-1890.

104. Saha, R. and R.K. Ray, *Effect of severe cold rolling and annealing on the development of texture, microstructure and grain boundary character distribution in an interstitial free steel.* ISIJ International, 2008. **48**: p. 976-983.

105. Wang, Z.-d., et al., *Effect of Processing Condition on Texture and Drawability of a Ferritic Rolled and Annealed Interstitial-Free Steel.* Journal of Iron and Steel Research, International, 2006. **13**(6): p. 60-65.

106. Martínez, V.J., J.I. Verdeja, and J.A. Pero-Sanz, *Interstitial free steel:*

*Influence of [alpha]-phase hot-rolling and cold-rolling reduction to obtain extra-deep drawing quality.* Materials Characterization, 2001. **46**(1): p. 45-53.

107. Ghosh, P., et al., *Comparative study of precipitation behavior and texture formation in continuously annealed Ti and Ti + Nb added interstitial-free high-strength steels.* Scripta Materialia, 2008. **58**(11): p. 939-942.

108. Ghosh, P., C. Ghosh, and R.K. Ray, *Thermodynamics of precipitation and textural development in batch-annealed interstitial-free high-strength steels.* Acta Materialia, 2010. **58**(11): p. 3842-3850.

109. Samet-Meziou, A., et al., *TEM Study of Recovery and Recrystallization Mechanisms after 40% Cold rolling in an IF-Ti steel.* ISIJ International, 2008. **48**: p. 976-983.

110. Verbeken, K. and L. Kestens, *Strain-induced selective growth in an ultra low carbon steel after a small rolling reduction.* Acta Materialia, 2003. **51**(6): p. 1679-1690.

111. Bhadeshia, H.K.D.H., *Neural networks and information in materials science.* Statistical Analysis and Data Mining, 2009. **1**: p. 296-305.

112. Yescas, M.A., H.K.D.H. Bhadeshia, and D.J. MacKay, *Estimation of the amount of retained austenite in austempered ductile irons using neural networks.* Materials Science and Engineering A, 2001. **311**(1-2): p. 162-173.

113. Cottrell, G.A., et al., *Neural network analysis of Charpy transition temperature of irradiated low-activation martensitic steels.* Journal of

Nuclear Materials, 2007. **367-370**(Part 1): p. 603-609.

114. Capdevila, C., et al., *Proposal of an empirical formula for the austenitising temperature.* Materials Science and Engineering A, 2004. **386**(1-2): p. 354-361.

115. Bhadeshia, H.K.D.H., *Mechanisms and Models for Creep Deformation and Rupture*, in *Comprehensive Structural Integrity*, I. Milne, R.O. Ritchie, and B. Karihaloo, Editors. 2003, Pergamon: Oxford. p. 1-23.

116. Emren, F., U. von Schlippenbach, and K. Lücke, *Investigation of the development of the recrystallization textures in deep drawing steels by ODF analysis.* Acta Metallurgica, 1986. **34**(11): p. 2105-2117.

117. Akben, M.G., et al., *Dynamic precipitation and solute hardening in a titanium microalloyed steel containing three levels of manganese.* Acta Metallurgica, 1984. **32**(4): p. 591-601.

118. Hamart, O., T. Lung, and S. lanteri. *40th MWSP Conference Proceedings*. 1998. Warrendale(PA):ISS.

119. Lee, K., S.-H. Han, and Y.-S. Jin. in *International Forum for the Properties and Application of IF Steels*. 2003. Tokyo.

120. Gladman, T., *The physical metallurgy of microalloyed steels*. 1997, London: Institute of Materials.

121. Samajdar, I., et al., *γ-Fibre recrystallization texture in IF-steel: an investigation on the recrystallization mechanisms.* Materials Science and Engineering A, 1997. **238**(2): p. 343-350.

122. De Cooman, B.C., *Structure-properties relationship in TRIP steels containing carbide-free bainite.* Current Opinion in Solid State and Materials Science. **8**(3-4): p. 285-303.

123. Zaefferer, S., J. Ohlert, and W. Bleck, *A study of microstructure, transformation mechanisms and correlation between microstructure and mechanical properties of a low alloyed TRIP steel.* Acta Materialia, 2004. **52**(9): p. 2765-2778.

124. Choi, K.S., et al., *Microstructure-based constitutive modeling of TRIP steel: Prediction of ductility and failure modes under different loading conditions.* Acta Materialia, 2009. **57**(8): p. 2592-2604.

125. Suh, D.W., et al., *Influence of Al on the microstructural evolution and mechanical behavior of low-carbon, manganese transformation-induced-plasticity steel.* Metallurgical and Materials Transactions A: Physical Metallurgy and Materials Science, 2010. **41**(2): p. 397-408.

126. Suh, D.-W., et al., *Influence of partial replacement of Si by Al on the change of phase fraction during heat treatment of TRIP steels.* Scripta Materialia, 2007. **57**(12): p. 1097-1100.

127. Peranio, N., et al., *Microstructure and texture evolution in dual-phase steels: Competition between recovery, recrystallization, and phase transformation.* Materials Science and Engineering: A, 2010. **527**(16-17): p. 4161-4168.

128. Lee, S.-J., Y.-M. Park, and Y.-K. Lee, *Reverse transformation mechanism of martensite to austenite in a metastable austenitic alloy.* Materials Science

and Engineering: A, 2009. **515**(1-2): p. 32-37.

129. Bleck, W., A. Frehn, and J. Ohlert. in *Niobium Science and Technology: The International Symposium Niobium 2001*. 2001. Orlando, FL, USA.

130. Humphreys, F.J. and M. hatherly, *Recrystallization and Related Annealing phenomena*. 2004: Elsevier, Oxford, GB.

131. Rocha, R.O., et al., *Microstructural evolution at the initial stages of continuous annealing of cold rolled dual-phase steel.* Materials Science and Engineering A, 2005. **391**(1-2): p. 296-304.

132. Petrov, R., et al., *Microstructure and texture of a lightly deformed TRIP-assisted steel characterized by means of the EBSD technique.* Materials Science and Engineering: A, 2007. **447**(1-2): p. 285-297.

133. Jorge-Badiola, D., A. Iza-Mendia, and I. Gutiérrez, *Study by EBSD of the development of the substructure in a hot deformed 304 stainless steel.* Materials Science and Engineering A, 2005. **394**(1-2): p. 445-454.

134. Dziaszyk, S., et al., *On the characterization of recrystallized fraction using electron backscatter diffraction: A direct comparison to local hardness in an IF steel using nanoindentation.* Materials Science and Engineering: A. **In Press, Corrected Proof**.

135. Calcagnotto, M., et al., *Orientation gradients and geometrically necessary dislocations in ultrafine grained dual-phase steels studied by 2D and 3D EBSD.* Materials Science and Engineering: A, 2010. **527**(10-11): p. 2738-2746.

136. Wilson, A.W., J.D. Madison, and G. Spanos, *Determining phase volume fraction in steels by electron backscattered diffraction.* Scripta Materialia, 2001. **45**(12): p. 1335-1340.

137. Verbeken, K., N. Van Caenegem, and M. Verhaege, *Quantification of the amount of ε–martensite in a Fe-Mn-Si-Cr-Ni shape memory alloy by means of electron backscatter diffraction.* Materials Science and Engineering: A, 2008. **481-482**: p. 471-475.

138. Verbeken, K., N. Van Caenegem, and D. Raabe, *Identification of ε-martensite in a Fe-based shape memory alloy by means of EBSD.* Micron, 2009. **40**(1): p. 151-156.

139. Kitahara, H., et al., *Crystallographic analysis of plate martensite in Fe-28.5 at.% Ni by FE-SEM/EBSD.* Materials Characterization, 2005. **54**(4-5): p. 378-386.

# Acknowledgements

I am grateful to the POSCO, Korea for funding this project. I would also like to thank POSCO for allowing me to take study leave for 4 years.

I would like to express my sincere gratitude to my supervisor, Prof. H. K. D. H. Bhadeshia, for his guidance and encouragement. I am also thankful to Professor Dong-Woo Suh for his guidance and friendship as my co-advisor. I also want to express my great thanks to Professor Nack-Joon Kim, the Dean of Graduate Institute of Ferrous Technology, for the provision of laboratory facilities and the atmosphere at POSTECH and Professor Hae-Geon Lee for their advice and support.

Support from Dr. Carlos Capdevila Montes and Dr. Francisca Caballero in CENIM-CSIC, Spain is gratefully acknowledged – who helped with many experiments. I would like to express my sincere gratitude to Dr. S. Kundu and Dr. S. Babu for their helpful discussions and advices. I am indebted to Dr. Jang-Yong You, Dr. Kyung-Kun Um for their help and encouragement with the experiments conducted at POSCO.

I have received technical help suggestions from many other people during the course of this work. I want to specially mention Prof. De Cooman, Prof. Hu-Chul Lee for many helpful discussions.

I would like to express sincere thanks to all the people in the Graduate Institute of

Ferrous Technology (GIFT) in Pohang University of Science and Technology, especially those members in Computational Metallurgy Laboratory (CML), for all their help and for all the memories we have.

Finally, I wish to record my deep sense of appreciation to my parents, wife for their love and support during the entire period.

학부와 석사를 졸업하고 박사과정을 마무리 하는 지금까지 10 년의 시간이 흘렀습니다. 그 동안 힘들었던 일, 슬펐던 일들 보다는 기쁘고 행복한 일들이 훨씬 많기에, 이 마음을 조금이나마 더 표현하고자 글을 씁니다.

우선, 늘 솔선 수범하시며 저를 올바른 학자의 길로 인도해 주신 Bhadeshia 교수님께 먼저 감사의 말씀 올립니다. 끊임 없이 정진하시고 항상 새로운 것을 찾으시는 모습은 학생들에게 늘 귀감이 되었습니다. 딱딱 할 수 있는 사제간의 관계를 늘 부드럽게 유지하시면서도 연구를 하실 때에는 늘 진중하시며 열정적이셨습니다.

강한 리더십으로 늘 연구실에 활력을 불어넣어 주시는 서동우 교수님께도 감사의 말씀 올립니다. 실험이 잘 되지 않아 진척이 없어 풀이 죽어 있을 때에는 다정다감한 친 형처럼, 연구에 있어 소홀함이나 나태함을 보일 때에는 엄한 아버지처럼 저를 대해주셨습니다. 그 덕분에 큰 힘을 얻고 무사히 박사과정을 마칠 수 있었습니다.

4 년 동안 학교에서 수학을 할 수 있도록 도움을 주신 포스코 후판 연구그룹 연구원 분들께도 감사의 말씀 드립니다. 바쁘신 와중에서도 디펜스 때 참석해 주신 엄경근 박사님께 먼저 감사 드리며 연구에 많은 조언을 해주신 유장용 박사님과 최종교 박사님께도 감사의 말씀 올립니다.

늘 함께 동고 동락 했던 연구실 식구들에게도 저의 마음을 전합니다. 준학, 홍석, 주현, 민성, 재용, 재훈, 유영, 승우, 은주, 영주, 지용, 근수, 한번도 제대로 고맙다는 표현을 못한 것 같습니다. 모두 착하고 성실한 동생들이니 졸업하고 어디에 있던지 제 몫은 다 하는 연구원이 되리라 믿어 의심 치 않습니다.

늘 바쁘다는 핑계로 연락도 제대로 못 드리고 자주 찾아 뵙지도 못해 불효만 한 것 같습니다. 아버님 어머님 그리고 장인어른 장모님께도 큰절을 올립니다. 앞으로 살면서 못다한 효도를 다하겠습니다. 두문불출하는 오빠를 대신해서 궂은 일 도맡아서 하는 여동생 내외에게도 고맙습니다. 지수, 민준이 건강하게 잘 자라기를 기원합니다. 그리고 공부하느라 잘 챙겨주지도 못한 우리 처남과 처제에게도 미안함과 고마움을 전합니다.

끝으로 저의 처에게 글을 남깁니다.

여보, 11 월 15 일이면 당신과 결혼하고 이제 꼭 1 년 째 되는 날입니다. 매주 장거리 출퇴근 하면서 보러 오겠노라고 약속해놓고 바쁘다는 핑계로 한 달에 몇 번 보지도 못하고 혼자 큰 집 남겨놔서 미안해요. 기쁠 때, 행복할 때에는 늘 당신이 먼저 생각이 나고, 슬프고 힘들 때에도 당신의 위로와 따듯한 손이 먼저 떠오릅니다. 늘 묵묵히 내 곁에 있어줘서 고맙고 사랑합니다.

2010. 10. 28

김 대 우

# CURRICULUM VITAE

**Name:** Kim, Dae Woo (金 昊 優)

**E-mail:** gomdury@postech.ac.kr

**Date of birth:** 14nd Augest, 1978

**Place of birth:** DaeGu, South Korea

**Education**

**B. S**. 2005, Kyungpook National University (Daegu, Korea), Department of Materials and Engineering

**M. S**. 2007, POSTECH (Pohang, Korea), Department of Materials Science and Engineering

**Ph.D**. 2011, POSTECH (Pohang, Korea), Graduate Institute of Ferrous Technology, Computational Metallurgy Group